PHOTOPRODUCTION OF $D^{\pm}$ MESONS

BY

KAREN LYNETTE LINGEL

B.A., University of California, 1983
M.S., University of Illinois, 1984

THESIS

Submitted in partial fulfillment of the requirements
for the degree of Doctor of Philosophy in Physics
in the Graduate College of the
University of Illinois at Urbana-Champaign, 1990

Urbana, Illinois

A283994

PHOTOPRODUCTION OF $D^{\pm}$ MESONS

Karen Lynette Lingel, Ph.D.
Department of Physics
University of Illinois at Urbana-Champaign, 1990
James E. Wiss, Advisor

$D^{\pm}$ mesons have been observed in photoproduction in Fermilab experiment E687. A sample of approximately 2500 events of the decay $D^{\pm} \rightarrow K^{\mp}\pi^{\pm}\pi^{\pm}$ has been analyzed. The cross section for $x_f > 0$ is measured to be

$$\mathrm{BR} \cdot \sigma = 0.368 \pm 0.073 \ \ \pm 0.111 \ \mu\mathrm{b/Be\ nucleus}$$

at our average photon energy of 220 GeV. The cross section dependence on incident photon energy, Feynman x, and transverse momentum has also been measured and found to be in good agreement with other measurements.

The lifetime of the $D^{\pm}$ has been measured to be 1.061 ± 0.039 ± 0.020 picoseconds. This measurement is also in good agreement with recent results.

Acknowledgements

E687 would not exist without the unique contributions from each of its members. I cannot list each collaborator here, nor his or her many important contributions to the experiment. Nonetheless, I wish to express my appreciation for their efforts.

My advisor, Jim Wiss, deserves special thanks. He has a remarkable grasp of physics at every level, and an uncanny way of explaining it in a clear and fundamental way.

I thank Joel Butler, E687 spokesman, for his relentless pursuit of data. He managed the experiment with the proper goal in mind. He is a good person to have on our side.

I am grateful for John Cumalat's insight and fresh perspective.

We are truly lucky to have the expertise and competence of Jeff Wilson infusing nearly every aspect of the analysis. He is definitely worthy of the responsibilities heaped on him.

I thank my fellow UI colleagues: Glen Jaross, Ray Culbertson, and Paul Sheldon. Much of their work is reflected in this thesis.

Eric Mannel and Rik Yoshida deserve profound gratitude for undertaking the task of managing (quite effectively) the running of the reconstruction and the skims. Neither deserved the accompanying headaches or abuse.

I thank Dave Harding for his help and patience when I was starting my career as a Data Aquisition Person.

The staff and management of Fermilab and the DOE are to be thanked for their swift action after the fire at Wideband. Without this mobilization of forces, we may never have gotten any data.

I am grateful to Jerry Wray and Dave Lesny, who maintain the efficient, user-centered computer system at UI.

This research was funded in part by the U.S. Department of Energy under contract DEAC02-76ER01195. Thanks guys!

CONTENTS

Page

LIST OF ABBREVIATIONS

BGM	Beam Gamma Monitor: an electromagnetic shower counter at zero degrees, designed to collect primarily uninteracted beam photons.
BR	Branching Ratio: the fraction of parent particles which decay a certain way.
BT	Electron Beam Trigger scintillator counter which counts electrons in the electron beam.
CHC	Central Hadron Calorimeter: hadron calorimeter at zero degrees, which supplements the Hadron Calorimeter.
HC	Hadron Calorimeter: calorimeter to measure the energy of charged hadrons. This device is also used for triggering.
H×V	Two planes of scintillators: one with counters arranged horizontally, the other with the planes arranged vertically. These counters are used for triggering.
IE	Inner Electromagnetic shower counter: detects electromagnetic particles at smaller angles.
MG	Master Gate: the trigger which initiates basic data aquisition.
OE	Outer Electromagnetic shower counter: large aperture device for detecting electromagnetic particles.
OH	Outer Hodoscope: large aperture scintillator array, used for triggering.
PGF	Photon Gluon Fusion: a model for predicting heavy quark production.
PWC	Proportional Wire Chamber: wire chamber for detecting charged particles.
RESH	Recoil Electron Shower Hodoscope: a set of electromagnetic shower cells which detect the recoil electron.
RESHLO	Trigger condition which requires energy deposition in 1, 2, or 3 adjacent cells in the RESH counter.
SSD	Silicon Strip Detector: the high resolution, silicon microstrip vertexing detector.
TR1	Scintillator trigger counter immediately upstream of the microstrip detector.

INTRODUCTION

In 1964, Bjorken and Glashow [1] proposed the existence of a fourth quark, so that the number of quarks equaled the number of (known) leptons. In 1970, Glashow, Iliopoulos, and Maiani [2] proposed a theory of weak interactions, which required a fourth quark to explain the absence of strangeness-changing neutral currents. The discovery of the J/ψ in 1974 [3,4] led to speculations that this particle might be the lowest mass $c\bar{c}$ vector meson. Subsequent observation of excited ψ states [5] cemented this idea. In 1976, the first D mesons (open charm) were observed. [6,7]

Much of the early experimental work on D mesons has been done at e^+e^- machines. About 40% of e^+e^- events (well above threshold) are charm events, and beam-energy constraints significantly improve mass resolution as well as reject considerable background. However, these machines are limited by their luminosity. Much higher luminosity can be reached with photon beams, and although charm events constitute only about 1% of the events well above charm threshold, the absolute rate of production is higher than in e^+e^- machines. Photon beams can also sample the entire charm spectrum simultaneously. Unfortunately, background rejection is a more difficult task. Recently however, advances in technology (i.e., silicon microstrips) have made it possible to accurately measure decay vertexes of charm particles. Using the D meson lifetime, then, can significantly reduce the background.

E687 uses a high-luminosity bremsstrahlung photon beam to collect large samples of charm particles. A photon interacts in a Beryllium (or Silicon) target producing primary reaction products in the forward direction, including occasional charm particles. Generally speaking, nuclear fragments will travel at large angles and will not be detected. The charm particles will travel a certain distance (for $D^{\pm}$, a few centimeters) before decaying. The charm particle itself is not detected, but its charged decay daughters will leave tracks in the high resolution silicon microstrip vertex detector, and in the wire tracking chambers in the main spectrometer. The tracks' positions and directions can be reconstructed, and their bends in the analysis magnets will provide momentum information. With the aid of particle identification information from Cerenkov counters, we can reconstruct the original charm particle by forming an invariant mass. Since hadronic background is substantial in fixed target experiments, it is necessary to rely on the decay distance of the charm particle to distinguish these charm particles from hadronic background. This effort is aided greatly by the advanced, high-resolution silicon microstrip vertex detector, which can determine decay vertexes to high accuracy. The charm sample obtained by E687 in this way is comparable to the world's largest charm sample. This thesis will concentrate on three areas of $D^{\pm}$ phenomena: production dynamics, lifetime, and decay structure.

CHAPTER 1

Theory

1.1 Photon-Gluon Fusion Model

In the photon-gluon fusion (PGF) mechanism [8] for the photoproduction of heavy flavored states, the photon "fuses" with a gluon from the target nucleon, and creates a $c\bar{c}$ pair. The relevant diagrams are shown in Figure 1.1. The cross section for this process can be given as the cross section for the quark-level subprocess, $\hat{\sigma}(\omega, x)$, convoluted with the gluon distribution function:

$$\sigma(\omega) = \int_{x_{min}}^{1} dx\, G(x, Q^2)\, \hat{\sigma}(\omega, x) \tag{1.1}$$

where $G(x, Q^2)$ is the gluonic structure of the proton, which can be a function of the Q^2 of the process, $x_{min} = 4m_D^2/s$, and s is the total squared center of mass energy for this process: $s = m_N^2 + 2m_N\omega$ where ω is the energy of the photon, and m_N is the mass of the target nucleon. The quark sub-process cross section, calculated to first order in α_s is:

$$\hat{\sigma}(\omega, x) = \frac{2\pi\alpha\alpha_s}{\hat{s}}\left(\frac{e_q}{e}\right)^2\left[(1 + \gamma - \gamma^2/2)\ln\left(\frac{1+\beta}{1-\beta}\right) - \beta(1+\gamma)\right] \tag{1.2}$$

where $\hat{s} = xs$, $\gamma = 4m_c^2/\hat{s}$, $\beta = \sqrt{1-\gamma}$, By experimentally measuring the charm cross section, we can examine the predictive power of QCD.

Unfortunately, neither the gluon structure, the mass of the charm quark, nor the strong coupling constant (α_s) are known with high accuracy. Traditionally, the Q^2 dependance of the gluon structure function is ignored, and the form is taken to be:

$$x\, G(x) = \frac{1}{2}(N_g + 1)(1 - x)^{N_g} \tag{1.3}$$

with N_g generally taken to be 5-10. The behavior of the gluon structure function at low x is a matter of considerable interest and speculation. Recently, the CHARM collaboration has derived gluon distribution functions from neutrino data [9]. Figure 1.2 shows different gluon distribution functions.

The PGF model will also predict the form of the differential cross section ($d\sigma/dx_f$) as a function of Feynman x (x_f) of the charm quarks. However, the differential cross section for *mesons* will have a different behavior, due to effects of fragmentation, that is, how the charm quarks dress themselves into colorless particles.

Figure 1.3 shows PGF cross section calculations for different gluon structure functions and quark masses. Figure 1.4 shows the differential cross section for quarks, and for mesons, assuming a dressing function.

In 1988, Ellis and Nason [10] calculated second-order (in α_s) corrections to the PGF cross section. (Some example Feynman diagrams are shown in Figure 1.5.) These corrections are quite large. Although the shape of the $\sigma(\omega)$ does not change much (at high photon energies) the overall level increases by a factor of 2 to 4. These second-order calculations will be used when comparing the E687 results to theory. (See Chapter 5.)

1.2 Associated Production

QCD-based models like PGF are symmetric in charm and anti-charm. Associated production models claim that charm quarks are likely to combine with target baryon quarks, producing charm baryons. This leaves the anti-charm quark, which will materialize as an anti-charm meson. This model thus predicts an excess of anti-charm mesons relative to charm mesons. This is a well-known phenomenon in strange hyperon production right above threshold. The associated production mechanism was used to explain the complete lack of D^o events at a medium-energy (40-70 GeV) photoproduction experiment at the CERN SPS [11], although several hundred $\overline{D^o}$ were seen. We expect that associated production effects will diminish as photon energies are increased, that is, the charm meson to anti-charm meson ratio may be a function of the meson momentum.

1.3 D$^{\pm}$ Mesons

1.3.1 Lifetime of the $D^{\pm}$

The lifetime of the $D^{\pm}$ meson has interested physicists since its discovery. Using simple valence-quark diagrams (Figure 1.6a), where the non-charm quark in a $D^{\pm}$ or D^{o} meson is just a spectator, one would expect the lifetimes of the $D^{\pm}$ and the D^{o} to be equal, since the identity of the spectator cannot make any difference. Unfortunately, the lifetime of the $D^{\pm}$ is about 2.5 times longer than the D^{o}! It was thought that the annihilation diagram (Figure 1.6b), which exists for the D^{o} but not the $D^{\pm}$ was responsible for this discrepancy. Recently, however, this explanation has fallen into disfavor. The currently favored theory [12] is that the charged- and (effective) neutral-current diagrams (Figure 1.7), which for the $D^{\pm}$ produce identical final states, interfere destructively , thus lengthening the lifetime of the $D^{\pm}$ relative to the D^{o}.

1.3.2 Dynamic Sub-structure of the $D^{\pm} \to K^{\mp}\pi^{\pm}\pi^{\pm}$

MARK III noticed very strange-looking Dalitz plots of the $D^{\pm} \to K^{\mp}\pi^{\pm}\pi^{\pm}$ decay [13]. They attributed the distributions to the interference of the $D^{\pm} \to K^{*}(892)\pi^{\pm}$ decay with non-resonant background, which they were unable to describe adequately. Subsequently, Diakonou and Diakonos [14] have found that by assuming that the $D^{\pm} \to K^{\mp}\pi^{\pm}\pi^{\pm}$ decay is dominated by $D^{\pm} \to K^{*}(892)\pi^{\pm}$ and $D^{\pm} \to K_{0}^{*}(1430)\pi^{\pm}$, which interfere significantly, the MarkIII effects can be well-described.

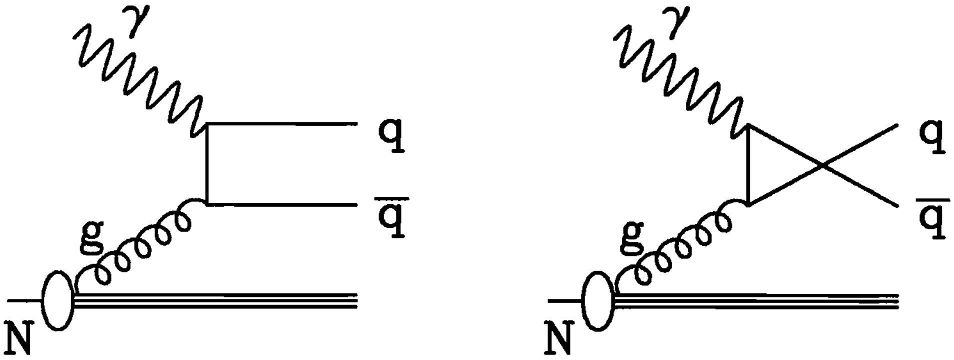

Figure 1.1: Feynman diagrams for photon gluon fusion.

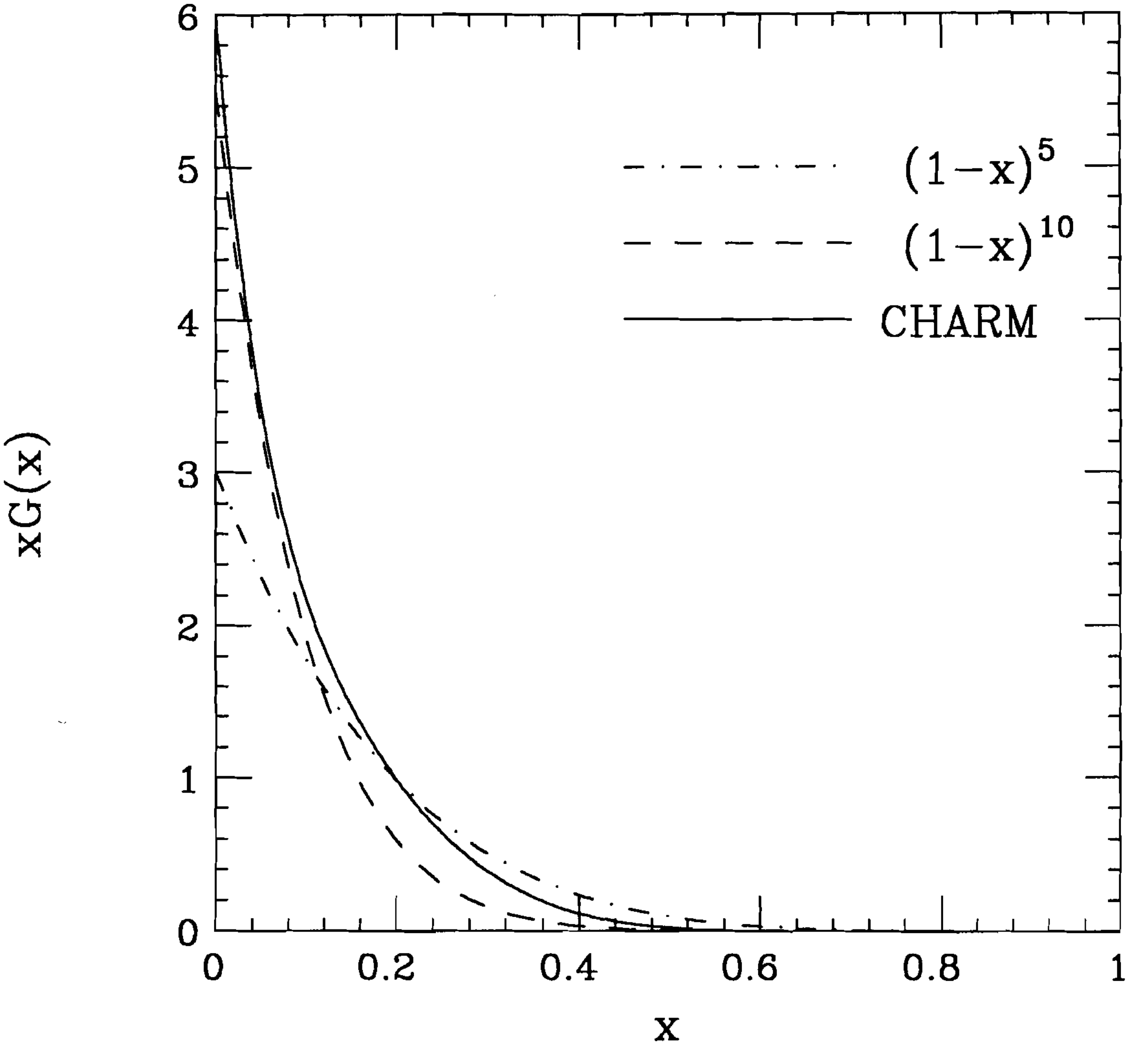

Figure 1.2: Various gluon distributions: $(1-x)^5$, $(1-x)^{10}$, and the measurement of the CHARM collaboration (at $Q^2 = 10$ GeV^2).

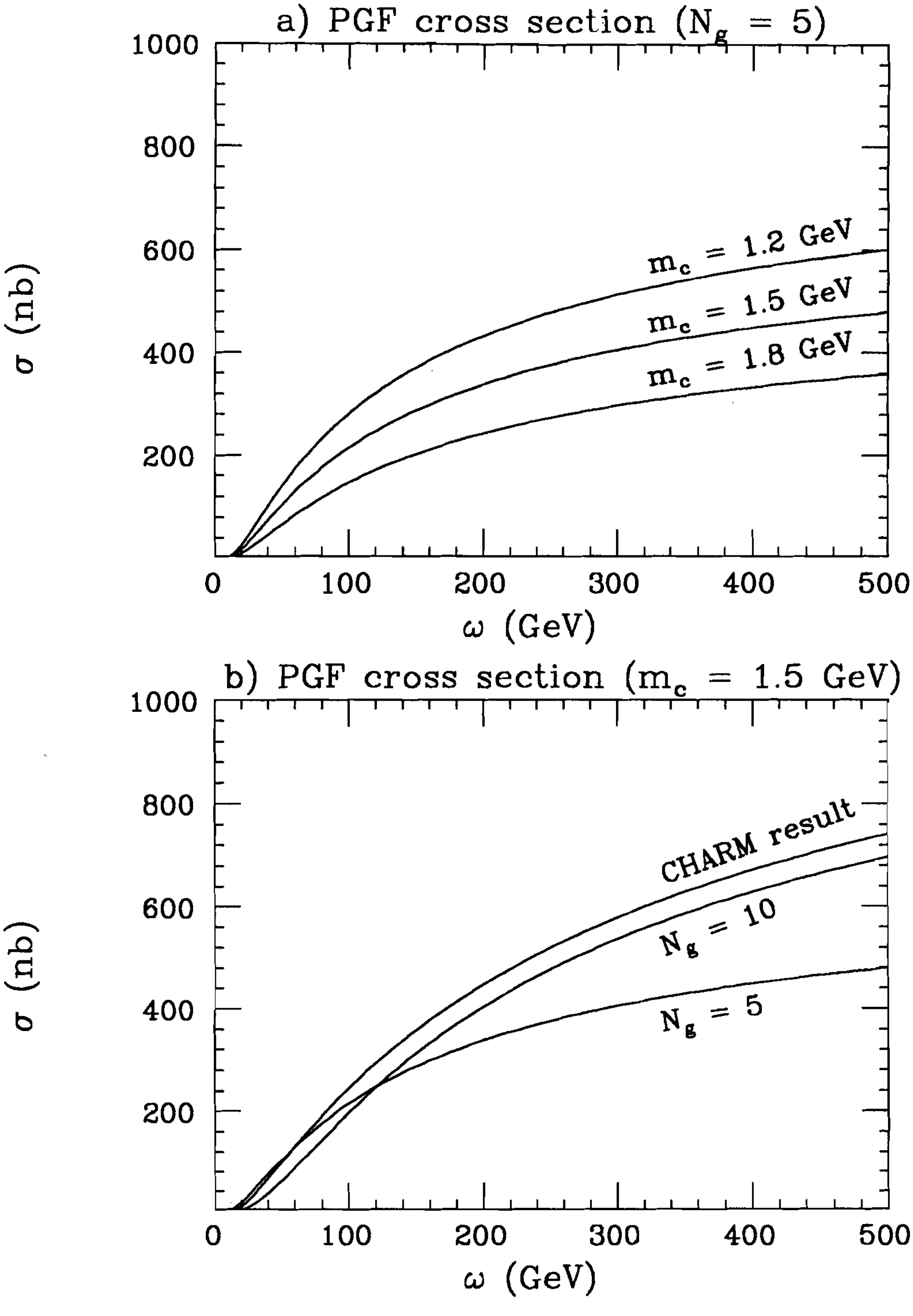

Figure 1.3: First order calculations of the photon-gluon fusion cross section a) for various charm quark masses. The gluon distribution $\propto (1 - x)^5$, and α_s is 0.2; b) for various gluon distribution functions, with $m_c = 1.5$ GeV, $\alpha_s = 0.2$.

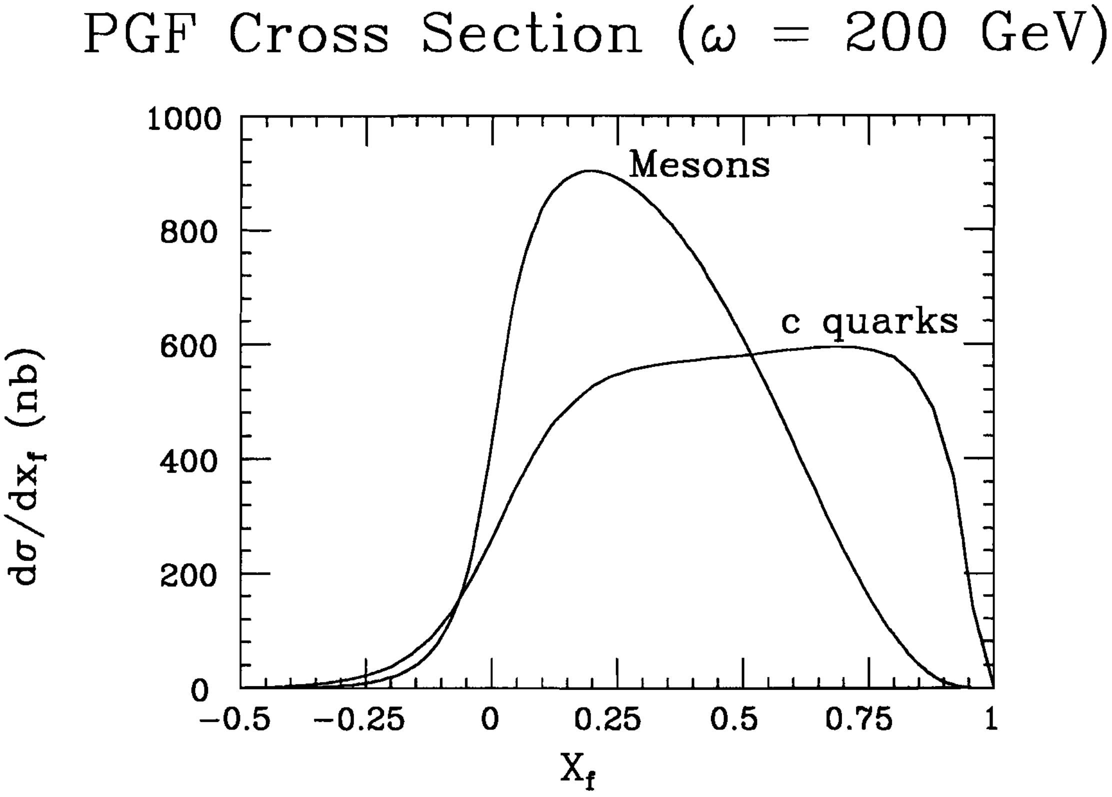

Figure 1.4: First order calculations of the PGF differential cross section for quarks and for mesons.

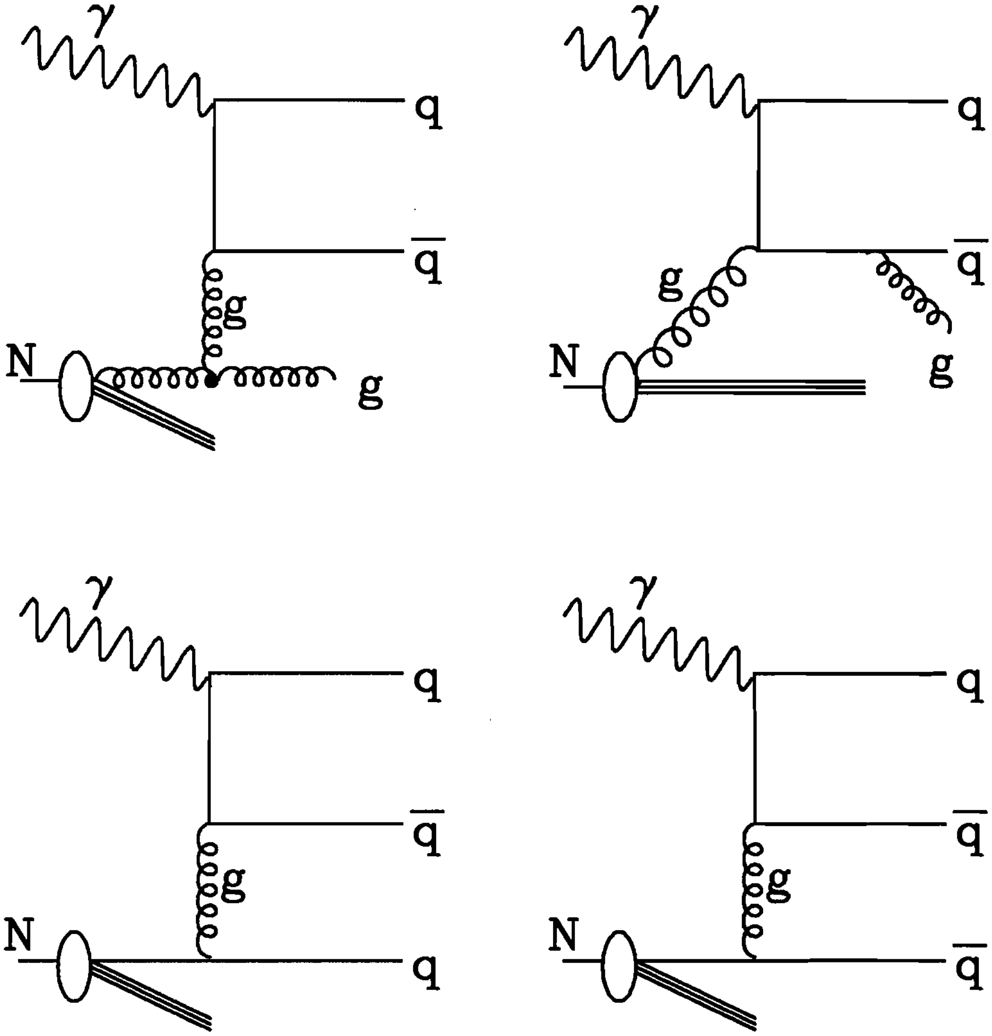

Figure 1.5: Photon-gluon fusion processes of second order in α_s.

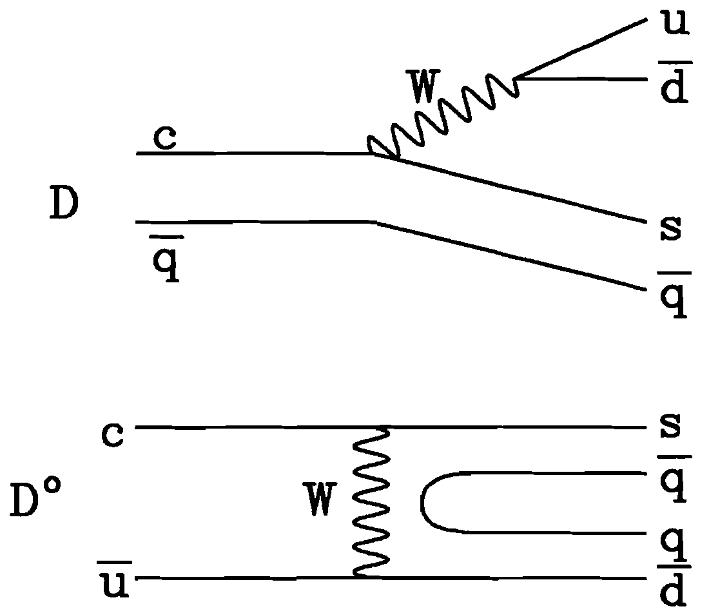

Figure 1.6: a) "Spectator" decay diagram for charm mesons decay. b) "Annihilation" decay diagram for D^o decay.

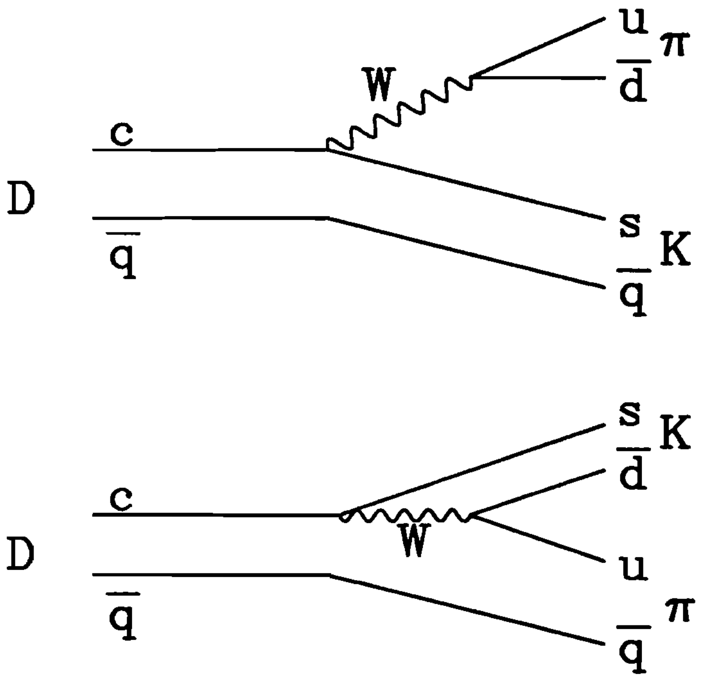

Figure 1.7: Decay diagrams for for D mesons. For $D^{\pm}$, these diagrams will produce identical final states, and thus interfere. These diagrams for the D^{o} do not produce identical final states.

CHAPTER 2
Apparatus

2.1 Beamline

The Wideband beamline was designed to be as versatile as possible. In different configurations, it can transport neutral hadrons, electrons, muons, pions, or photons to the experimental target. While E687 uses the clean photon beam for experimental data, other beams are useful for calibration.

The FNAL Tevatron provides 800 GeV protons to the Proton East (PE) line. (See Figure 2.1). These protons are incident on a 46 cm beryllium production target (about 77% of a radiation length, 89% of an interaction length). The charged particles are swept out of the resulting beam, leaving neutrons, neutral kaons, and photons (primarily from π^0 decay). The neutral beam impinges on a lead converter of about 60% radiation length which converts photons to e^+e^- pairs. The electrons are captured and transported around a beam dump, in which the leftover neutral particles are absorbed. In the process of transporting the electrons, the secondary beam energy is selected: 350 GeV for this analysis. The steering magnet apertures and collimators are such to allow for a large (about $\pm 13\%$) momentum bite, hence the "Wideband" name. The electron beam impinges on a lead radiator of about 20% radiation length which produces the final bremsstrahlung photon beam. (Additional beamline material increases the total radiator to 27% of a radiation length.) The recoil electrons are swept out of the beamline with sweeper magnets, where they are recorded in the Recoil Electron Shower Hodoscope (RESH). The RESH is a system of 10 lead-scintillator shower counters shown in Figure 2.2. The position of the hit cell gives the energy of the recoil electron.

Photons from the beamline will either interact in the target to produce events, or travel through the center of the spectrometer, to be collected at the Beam Gamma Monitor (BGM). The BGM consists of 45 layers of lead (0.32 cm thick) interleaved with Lucite (0.32 cm thick). The BGM serves two purposes: 1) as a luminosity monitor, its signal is discriminated, and a scaler counts each signal corresponding to energy deposition in the BGM of 133 GeV or more. (More on luminosity in chapter 5.) 2) as a multiple bremsstrahlung photon collector, it measures the energy deposition from photons from the electromagnetic shower in the radiator which did not interact in the target. Using the average value for the energy of the incident electron, the RESH and BGM supply us with enough information to estimate the energy of the interacting photon. (More on photon energy estimation in Chapter 3).

2.2 Targets

The experiment used three major targets:[1] two beryllium targets ("5-Be" and "4-Be") and a silicon wafer target ("Si"). The 5-Be (4-Be) target consists of 2 (1) square, large transverse Be segments, 2.54 cm on a side and 0.8128 cm thick. (See Figure 2.3). These segments are oriented at 45 degrees with respect to the vertical view, as shown in the figure. The remaining 3 segments are smaller transverse pieces of beryllium, 0.8128 cm thick, hexagonal-shaped to match the high resolution area of the microstrip detector. The gaps between segments are 75-200 microns. The total radiation length of the 5-Be (4-Be) target is 11.5% (9.2%).

The Si target consists of 29 silicon wafers of 220 micron thickness interleaved with 300 micron Be wafers, followed by 19 silicon wafers of 250 micron thickness, with 250 micron gaps between wafers. (See Figure 2.4.) The total radiation length of the Si target is 14.4% (11.9% from Si, 2.5% from Be). The Si wafers were pulse-height analyzed so that jumps in charge multiplicity from one plane to another would localize the primary interaction point. Although data taken with the Si target are used in this analysis, the charge multiplicity information is not used here.

2.3 Spectrometer

The E687 spectrometer was designed as a multi-purpose device. It consists of several systems: tracking, Cerenkov particle identification, calorimetry, muon identification,

---

[1] Also some minor targets, including $4.75 in quarters.

and trigger. Table 2.1 gives locations and sizes of each device in the spectrometer. Figure 2.5 shows the plan and elevation views of the spectrometer.

2.3.1 Tracking

The tracking system consists of two momentum-analyzing magnets, 5 multi-wire proportional chambers, and 12 planes of silicon microstrip detector planes. The magnets, M1 and M2, are run with opposite polarity, with current chosen to give momentum kicks of 0.400 GeV and -0.850 GeV, respectively

The wire chambers (PWCs) consist of 4 views (except P4), an X and a Y (measuring) view, plus U and V views at $\pm\arctan(.2)$ from the Y view. Wire chambers P0 and P3 are sized to match the aperture of the analysis magnets; the other chambers are matched to the acceptance of the spectrometer (except P4). Our original P4 was destroyed by fire [15], and was replaced with a similar chamber, but smaller, and with only 3 views: X, U, and V (with same stereo angles). All chambers were run with argon-ethane (65%/35%) bubbled through ethyl alcohol. Table 2.2 gives specifications of the PWCs.

The microstrips (SSDs) are organized into 4 stations of 3 views each (i, j, and k views); see Figure 2.6. The first station consists of strips of width 25 microns in the inner region, and 50 microns in the outer region. The other planes have 50 micron strips in the inner region and 100 micron strips in the outer region (Figure 2.6). The strips are read out in an analog way: charge division among strips is used to improve the resolution of the device.

2.3.2 Particle Identification

The E687 particle identification system consists of three threshold Cerenkov counters. Cerenkov counters C1 and C2 are located between the two magnets, and counter C3 is located downstream of the second magnet. Each counter consists of about 100 cells. Light from Cerenkov radiation is reflected off mirrors on the downstream face of the counter into phototubes. C3 and the outer region of C1 are outfitted with focussing mirrors. C2 and the inner section of C1 use planar mirrors at 45 degrees to the beamline. Specifications of the Cerenkov counters is summarized in Table 2.3.

2.3.3 Calorimetry

E687 has two electromagnetic shower counters, one large aperture Outer Electromagnetic shower counter (OE) just upstream of M1, for electromagnetic identification of particles in the outer spectrometer, and one Inner Electromagnetic shower counter (IE) for the inner spectrometer. Each shower counter consists of layers of lead and scintillator. Neither is used for this analysis.

The Hadron Calorimeter (HC) consists of 28 iron plates of 4.42 cm thickness (8 interaction lengths total), interleaved with sense planes, 2.86 cm thick. The sense planes consist of proportional tubes filled with 50% argon and 50% ethane. (In later runs, 1% ethyl alcohol vapor was added.) The signals are read capacitively from pads ganged together longitudinally to form towers. The hole in the HC is covered by a Central Hadron Calorimeter (CHC). The CHC consists of 16 layers of 3.8 cm thick depleted uranium slabs, clad with 0.24 cm thick steel, interleaved with 0.635 cm thick scintillator. The total amount of material is 6.4 interaction lengths. Together, the HC and CHC are used in the second level trigger, which requires that at least 35 GeV of energy is deposited in the hadrometers.

2.3.4 Muon System

The Muon system consists of planes of scintillator and gas proportional tubes. The outer muon system (OM) was just downstream of and shielded by the M1 magnet steel. OM comprised 2 planes of prop tubes and 2 planes of scintillator. The inner muon system was just downstream of the muon filter steel, comprising 4 prop tube planes and 3 scintillator planes. The muon system is not used in this analysis.

2.4 Trigger

Like most high energy experiments, E687 uses a two-level trigger system. The first level trigger, or Master Gate, is responsible for gating the data aquisition devices so that wire chambers can be read out, latches set, ADC's gated, etc. The Master Gate also holds off subsequent triggers, while the second level trigger is at work. The second level trigger, using PWC information, latch information, and ADC pulse height information, makes a decision as to whether the event is to be accepted or not. If the event is accepted, the inhibit against additional triggers continues while additional data aquisition tasks are completed (digitization of ADC information, readout into buffers, etc). If the event is not to be accepted, the second level trigger issues a fast clear, the data aquisition devices are cleared, and the inhibit is released.

2.4.1 First Level Triggering

Several trigger counters are used in E687: A scintillator counter in the electron beamline, T0; a scintillator in the photon beam, A0; two scintillators placed on either side of the photon beam pipe (for detecting muons in the beam halo), TM1 and TM2; and scintillator counters just upstream and just downstream of the microstrip detector, TR1 and TR2. A schematic drawing of the target region trigger counters is shown in Figure 2.7. The first level (or minimum bias) trigger (Master Gate, or MG) requires a charged particle in the electron beam (T0), no charged particle in the photon beam ($\overline{\mathrm{A0}}$), no muon from an upstream target ($\overline{TM1 + TM2}$) and charged particles emerging from the target (TR1·TR2). In addition we require two or more charged bodies in the spectrometer. This is accomplished with two trigger hodoscopes: The inner hodoscope, H×V and the outer hodoscope, OH. (Figure 2.8.) H×V is a set of crossed scintillators, located just downstream of the last PWC. A 7.1 cm gap separates the east and west halves, to allow uninteresting e^+e^- pairs to pass through. The OH is a layer of scintillators attached to the upstream face of the OE. The OH also has a gap between east and west halves. The Master Gate requires either two or more bodies in the H×V, or at least one body in the H×V and at least one body in the OH. The total Master Gate logical requirement is thus:

$$\mathrm{MG} = \mathrm{T} \cdot \left[\left((\mathrm{H} \times \mathrm{V})_{\geq 1\mathrm{body}} \cdot \mathrm{OH} \right) \oplus (\mathrm{H} \times \mathrm{V})_{\geq 2\mathrm{body}} \right] \qquad (2.1.a)$$

where

$$\mathrm{T} = \overline{\mathrm{A0}} \cdot \mathrm{T0} \cdot \mathrm{TR1} \cdot \mathrm{TR2} \cdot \overline{\mathrm{TM1} + \mathrm{TM2}} \qquad (2.1.b)$$

2.4.2 Second Level Triggering

The second level trigger required at least 35 GeV deposited in the HC, at least one hit in the x view of P0 (outside the pair region), and a signal in the RESH counter. Additional second level triggers (not used in this analysis), are a muon pair trigger, a prescaled e^+e^- pairs trigger, and a prescaled MG.

Table 2.1: Spectrometer layout

Device	Z location* (cm)	Z length (cm)	Transverse Size (cm)
5-Be target	-3.11	4.11	see text
SSD1	4.63	1.07	2.48 × 3.50
SSD2	10.69	1.07	4.96 × 4.96
SSD3	16.72	1.07	4.96 × 4.96
SSD4	28.66	1.07	4.96 × 4.96
M1 Up. Shield	77.44	17.78	336.00 × 384.00
M1 Up. Shield hole	77.44	17.78	25.40 × 101.60
M1 steel	220.95	167.64	350.52 × 546.10
M1 hole	220.95	167.64	76.20 × 127.00
M1 Down. Shield	370.17	8.90	336.00 × 384.00
M1 Down. Shield hole	370.17	8.90	76.20 × 127.00
P0	405.08	17.78	76.20 × 127.00
C1	519.75	187.90	101.60 × 152.40
P1	644.26	17.78	152.40 × 228.60
C2	757.00	187.96	152.40 × 228.60
P2	878.47	17.78	152.40 × 228.60
OE	962.99	132.40	270.00 × 300.00
OE hole	962.99	132.40	48.60 × 83.20
M2 Up. Shield	1091.43	8.90	336.00 × 384.00
M2 Up. Shield hole	1091.43	8.90	76.20 × 127.00
M2 steel	1238.11	167.64	350.52 × 546.10
M2 hole	1238.11	167.64	76.20 × 127.00
M2 Down. Shield	1383.52	8.90	336.00 × 384.00

---

* Z locations are measured from the front face of the Granite Block (which supports the microstrip detector) to the center of the device.

Table 2.1: (continued) Spectrometer layout

Device	Z location (cm)	Z length (cm)	Transverse Size (cm)
M2 Down. Shield hole	1383.52	8.90	76.20 × 127.00
Oμ X	1399.24	10.00	304.80 × 508.00
Oμ X hole	1399.24	10.00	101.60 × 162.56
Oμ Y	1416.94	10.00	304.80 × 508.00
Oμ Y hole	1416.94	10.00	101.60 × 162.56
P3	1442.60	17.78	76.20 × 127.00
Oμ H	1474.56	15.00	304.80 × 487.68
Oμ H hole	1474.56	15.00	121.92 × 152.40
Oμ V	1505.06	22.80	304.80 × 508.00
Oμ V hole	1505.06	22.80	121.92 × 152.40
C3	1884.42	711.20	190.50 × 228.60
P4	2288.89	17.78	101.60 × 152.40
H×V	2328.19	9.22	141.60 × 246.00
H×V gap	2328.19	9.22	7.10 × 365.80
IE	2399.67	76.84	123.12 × 123.12
IE hole	2399.67	76.84	10.16 × 10.16
HC	2569.78	219.30	203.20 × 304.80
HC hole	2569.78	219.30	30.00 (diameter)
BGM	2704.03	40.64	25.40 × 22.86
CHC	2778.00	101.60	45.72 × 45.72
μ filter1 iron	2895.66	128.60	231.14 × 330.20
μ filter1 hole	2895.66	128.60	10.16 × 10.16
Iμ 1X	2973.48	10.00	203.20 × 304.80
Iμ 1Y	2993.21	10.00	203.20 × 304.80

Table 2.1: (continued) Spectrometer layout

Device	Z location (cm)	Z length (cm)	Transverse Size (cm)
Iμ 1V	3012.52	15.30	213.36 × 304.80
Iμ 1H	3036.07	9.00	203.20 × 304.80
μ filter2 iron	3079.66	63.00	231.14 × 330.20
μ filter2 hole	3079.66	63.00	10.16 × 10.16
Iμ 2X	3138.95	10.00	203.20 × 304.80
Iμ 2Y	3158.09	10.00	203.20 × 304.80
Iμ 2H	3178.25	9.00	203.20 × 304.80

Table 2.2: PWC Specifications

		# instrumented wires			
Station	Pitch	X	U	V	Y
P0	2mm	376	640	640	640
P1	3mm	512	832	832	768
P2	3mm	512	832	832	768
P3	2mm	376	640	640	640
P4	X: 2mm; U,V: 3mm	336	768	768	-

Table 2.3: Cerenkov Counter Specifications

			Photoelectron	Thresholds (GeV)		
Counter	Gas	cells	yield (ave)	π	K	p
C1	50% He/50% N_2	90	2.6	6.7	23.3	44.3
C2	N_2O	110	8	4.4	16.2	30.9
C3	He	100	9	17.0	60.8	116.2

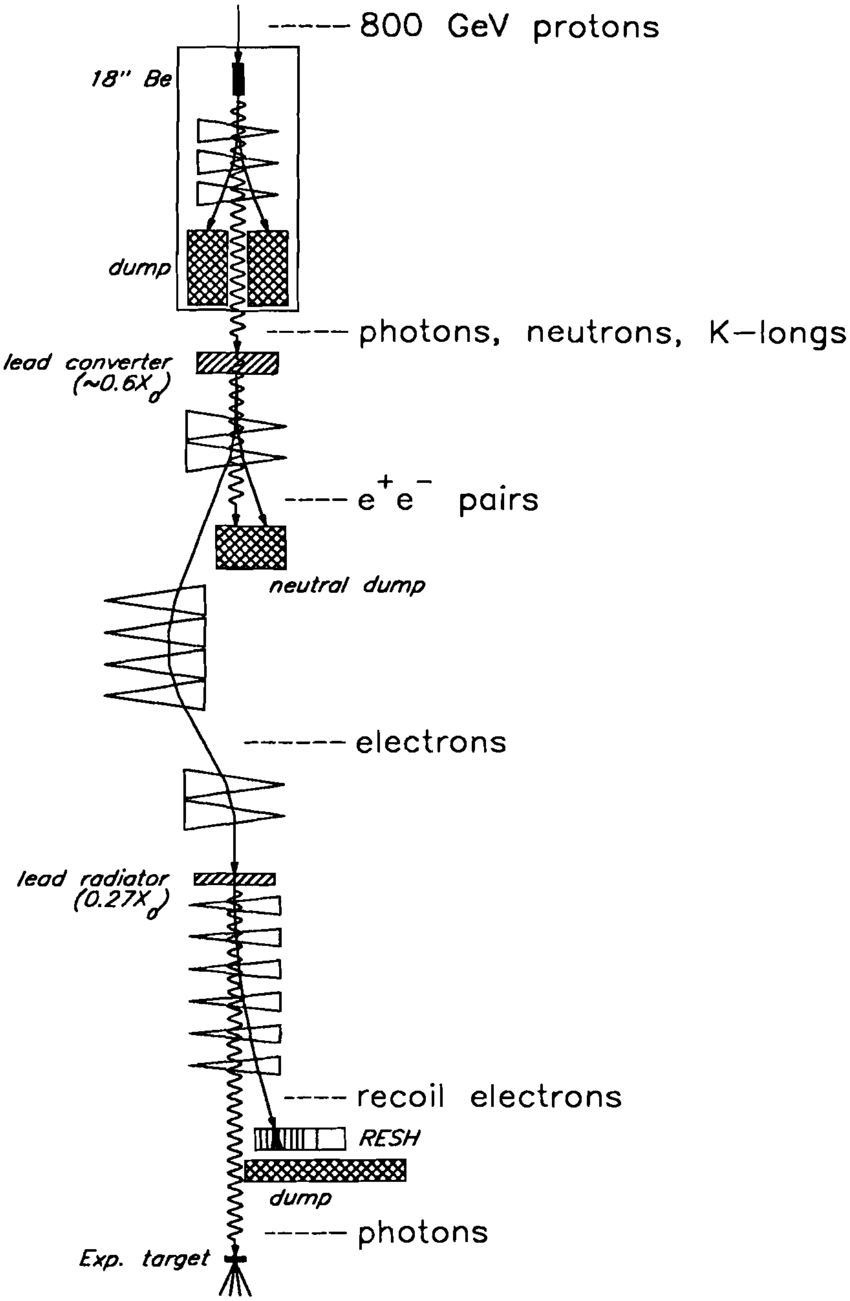

Figure 2.1: A schematic diagram of the steps involved in producing the E687 photon beam.

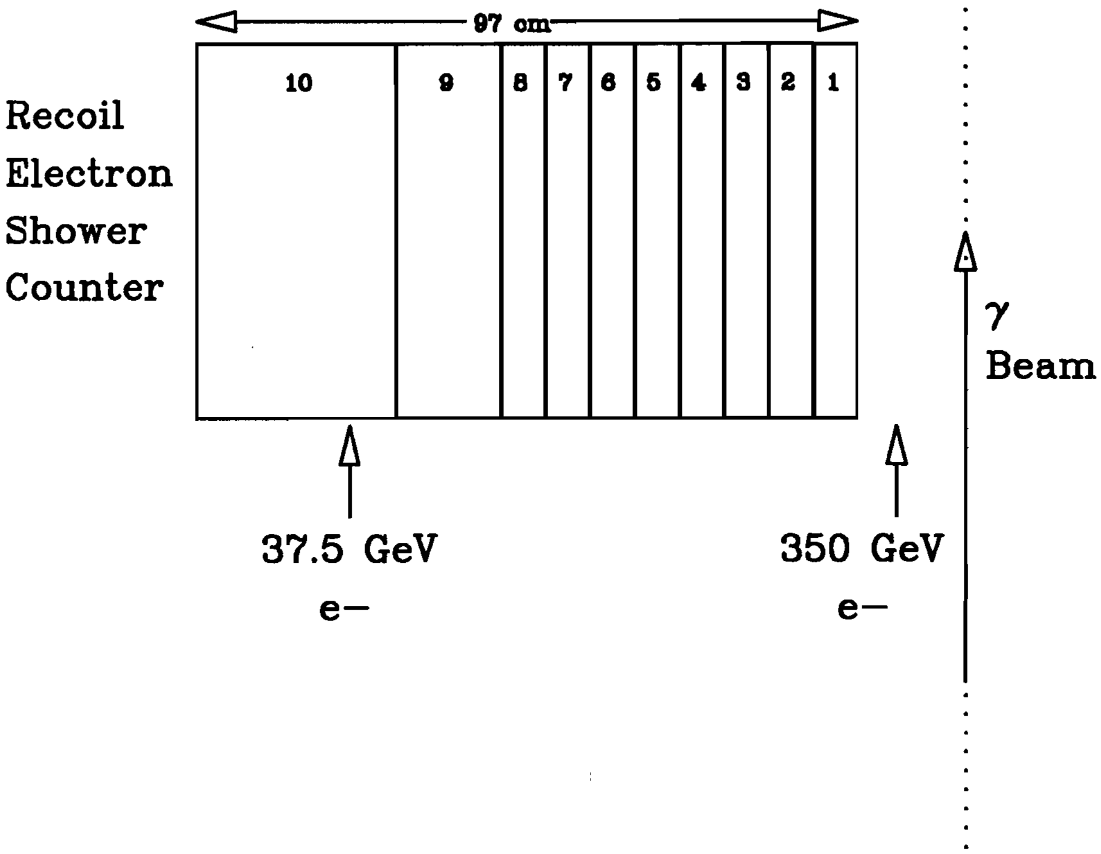

Plan View

Figure 2.2: Configuration of the Recoil Electron Shower Hodoscope (RESH).

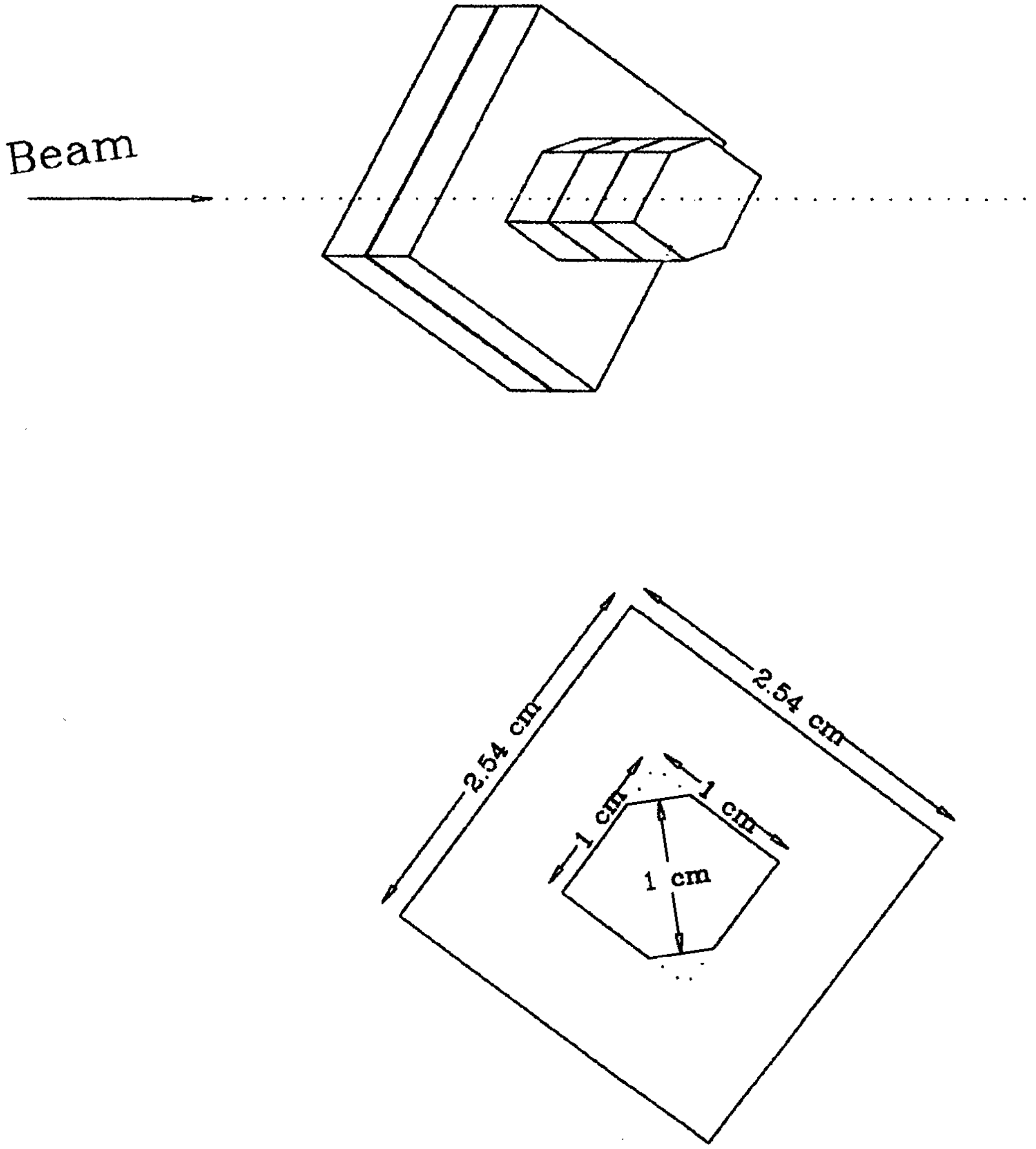

Figure 2.3: The 5-Be target.

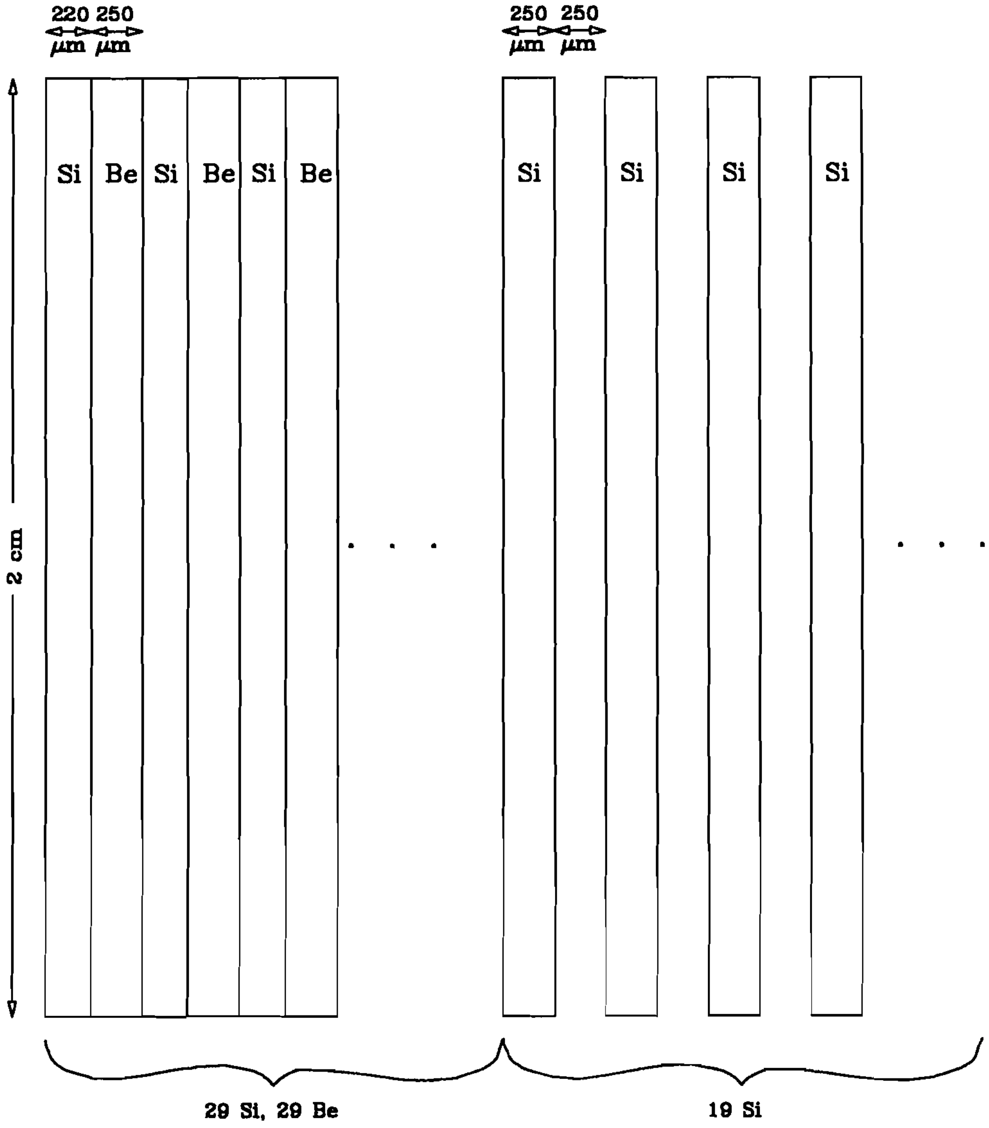

Figure 2.4: Silicon Wafer target.

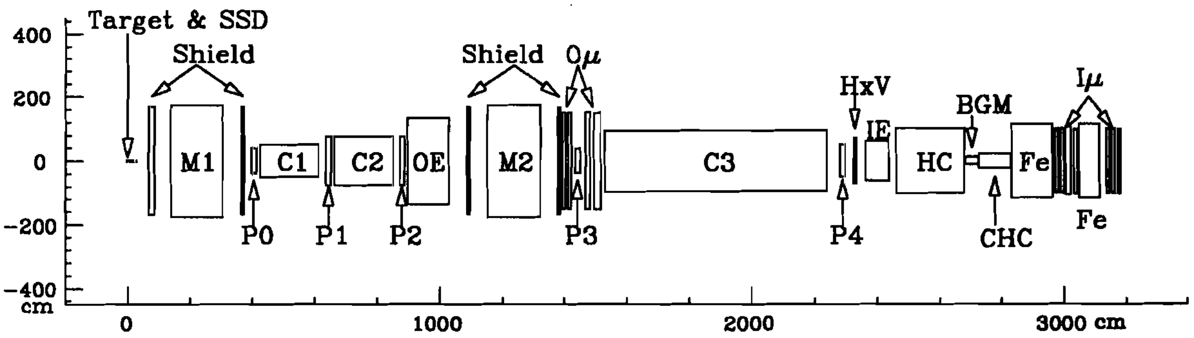

Top View

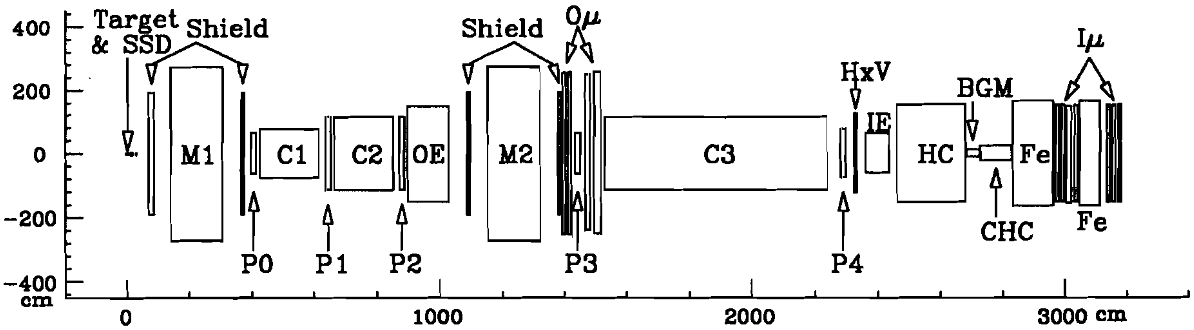

Side View

Figure 2.5: Plan and elevation views of the E687 spectrometer.

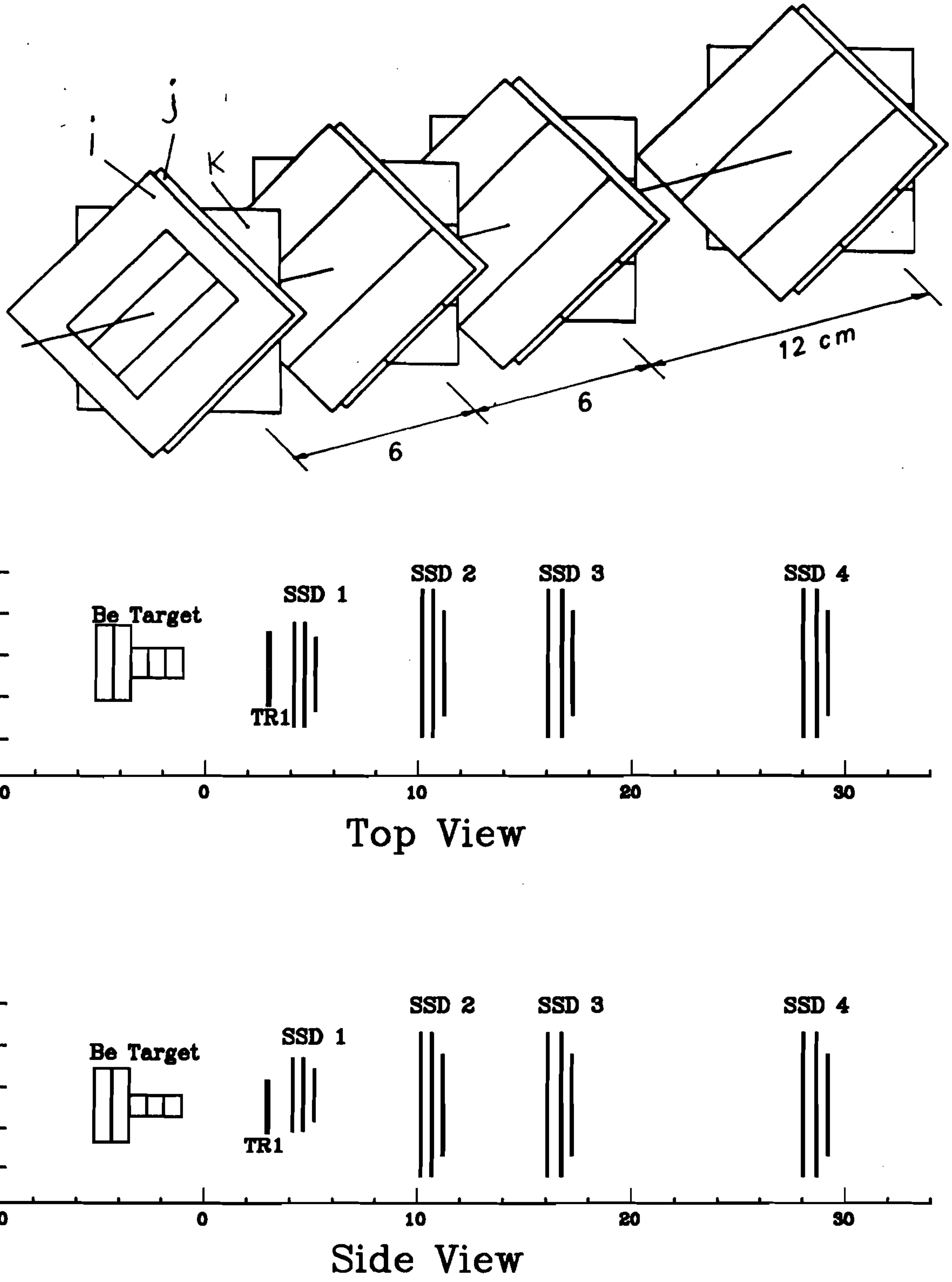

Figure 2.6: Silicon Microstrip Detector (SSD).

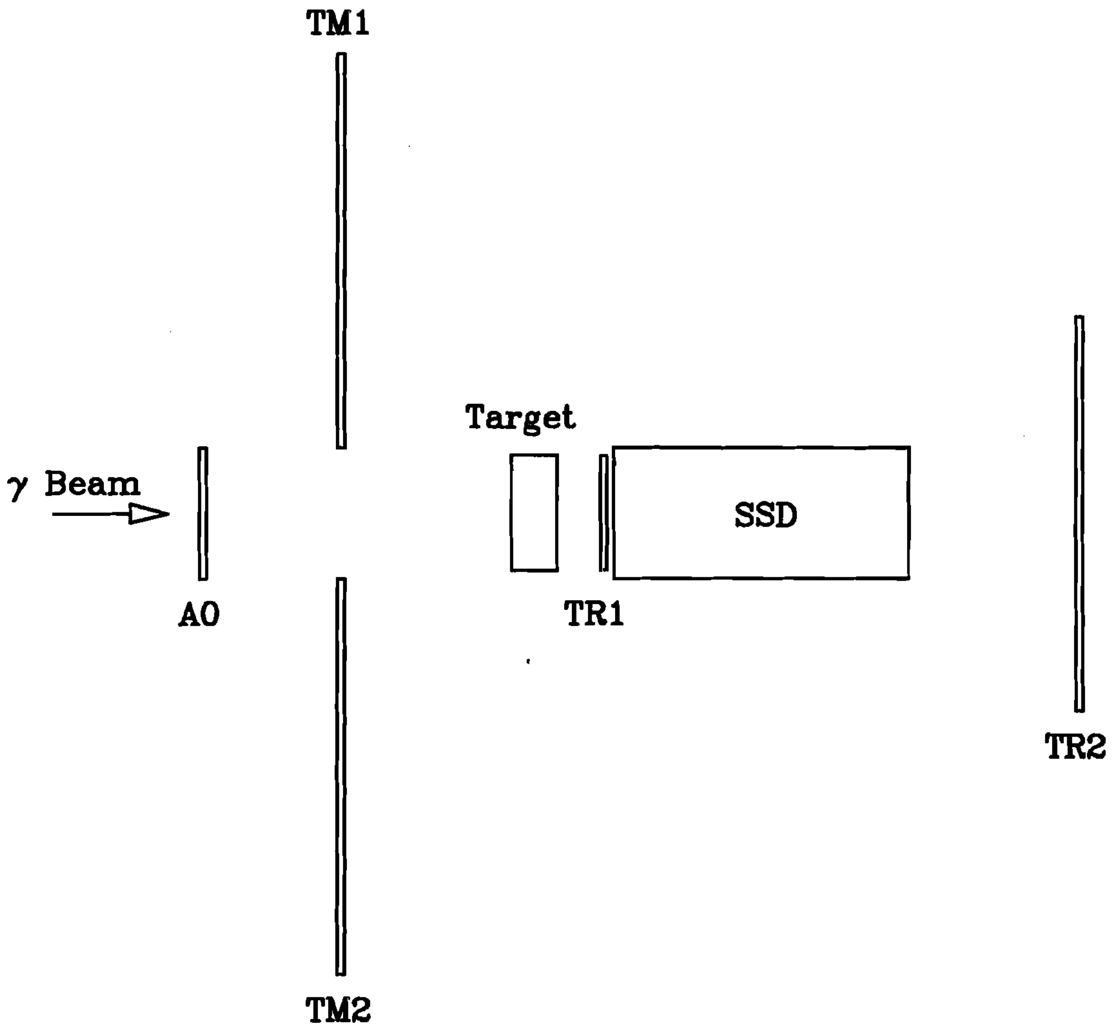

Figure 2.7: Schematic diagram of the trigger counters in the target region.

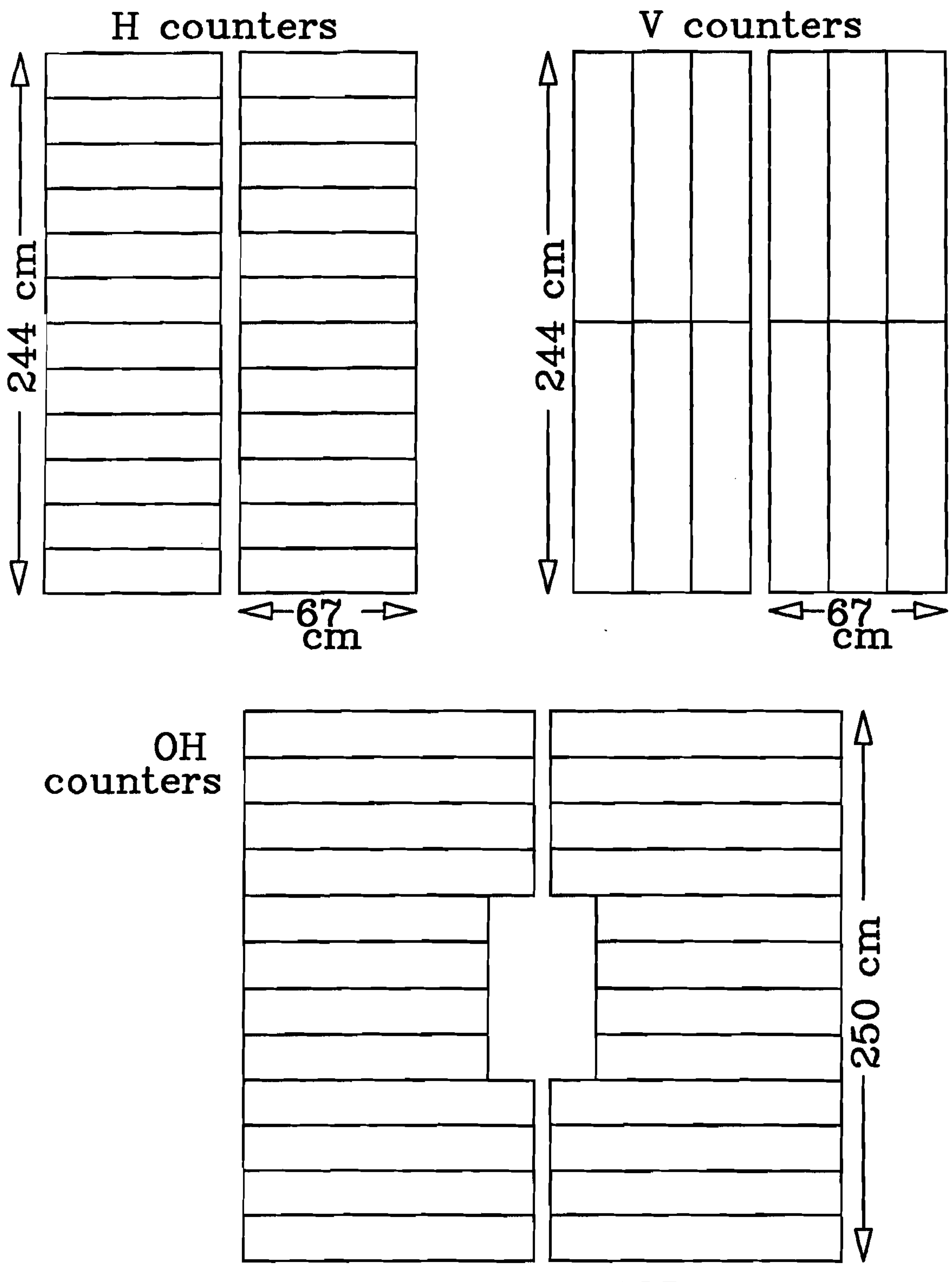

Figure 2.8: Schematic diagrams of the trigger hodoscopes.

CHAPTER 3

Analysis

3.1 Reconstruction and Analysis

3.1.1 SSD Track Reconstruction

The microstrip tracks are found by finding projections in the 3 views, then by matching the projections in space. Each projection is required to have at least 3 hits. Hit sharing is allowed. The resulting track is required to have a χ^2 per degree of freedom of 8 or less. Tracks which share projections are arbitrated by their χ^2 values. Leftover hits are then used to search for wide-angle or highly multiple-scattered tracks. The resolution of tracks which consist entirely of hits in the high resolution section of the SSD (extrapolated to the center of the target) is determined to be:

$$\sigma_x = 11\mu m\sqrt{1+\left(\frac{17.5GeV}{p}\right)^2}$$

$$\sigma_y = 7.7\mu m\sqrt{1+\left(\frac{25GeV}{p}\right)^2} \tag{3.1}$$

where the second term in the square root is the contribution due to multiple scattering effects.

3.1.2 PWC Track Reconstruction

PWC tracks are also found by projections. U,V, and Y view projections are found using PWC information only, and X (non-bend) view projections are found by matching hits to SSD track extrapolations. The projections are then matched, and must pass a χ^2 per degree of freedom cut. Tracks must not have more than 4 missing hits total, and no more than 2 missing hits can be from the same chamber. When all tracks with a SSD extension are found, X projections are found using PWC information alone, and matched to unused U, V, and Y projections.

In addition, "recovery" routines were used to find tracks in more difficult classes, such as SSD extensions into P0 and P1, and 3 chamber extensions into P3.

3.1.3 Linking

SSD tracks and PWC tracks are "linked" by matching extrapolations at the center of M1. The x and y positions as well as the slope in x are matched. Prospective links are subjected to a fit of all the hits, and must pass a χ^2 cut.

3.1.4 Momentum Determination

When all magnetic corrections have been applied to the tracks, the momentum can be determined by the bend of the track in M1 and/or M2. The momentum resolution is:

$$\frac{\sigma_p}{P} = \begin{cases} 3.4\% \left(\frac{P}{100GeV}\right) \sqrt{1 + \left(\frac{17GeV}{P}\right)^2} & \text{for M1;} \\ 1.4\% \left(\frac{P}{100GeV}\right) \sqrt{1 + \left(\frac{23GeV}{P}\right)^2} & \text{for M2} \end{cases} \tag{3.2}$$

where, again, the second term in the square root is the contribution due to multiple scattering.

3.1.5 Particle Identification

For each track traversing a Cerenkov counter, if the momentum is known and a particle identification (electron, pion, kaon, or proton) is assumed, predictions can be made about the Cerenkov light which the track contributes to associated cells (the cell the track hits, and all adjacent cells). If the light yield of the cells is greater than a certain noise level, the counter is called "on" for that track. If a cell could conceivably be "on" due to more than one track in the vicinity of the cell, then the counter is called "confused" for that track. Given the momentum of the track, the thresholds of the counters, and the on/off pattern for the track, the track can be placed (to the extent the three Cerenkov counters agree) into a definite or ambiguous identification category. Figure 3.1 shows the momentum ranges for which certain particle identification categories can be found.

Particularly important (since charm particles tend to decay into strange particles) are the kaon categories.

3.1.6 Vertex Reconstruction (Stand-alone Method)

The stand-alone vertexing algorithm is run on each event as part of the standard reconstruction. The algorithm tries to find free-form vertexes using only microstrip tracks. First, all tracks are put into one vertex, the χ^2 of the vertex is calculated. If the χ^2 is not acceptable, then the "worst" track (the track which contributes the most to the "badness" of the χ^2) is ejected from the vertex. The χ^2 of the new vertex is then calculated. The process repeats until a vertex of acceptable χ^2 is found. The algorithm is then applied to the ejected tracks, trying to form additional vertexes from them, until finally there is a list of acceptable vertexes (and some leftover tracks). The algorithm is able to find at least one vertex in about 50% of the events.

Since the stand-alone vertex algorithm is run on every event, the vertexes provided by this algorithm can be used by subsequent reconstruction techniques, for instance, finding neutral Vees, or determining the momentum of some categories of tracks.

Unfortunately, the stand-alone vertex algorithm is not very efficient at finding decay vertexes of short-lived particles. When two vertexes are close together, they can coalesce into one vertex, with a χ^2 acceptable to the algorithm. Additionally, small angle tracks from charm secondaries are often consistent with the primary or secondary vertex.

3.1.7 Vertex Reconstruction (Candidate-driven Method)

Because of the limitations of the stand-alone vertexing algorithm, a second vertexing algorithm was developed. This algorithm is run only when a possible fully-reconstructed "candidate" is found (for instance, by virtue of its invariant mass). The tracks in the candidate are then used to create a single "candidate" momentum vector. This candidate momentum vector is extrapolated backwards and used as a "seed" track for forming a primary vertex. The extrapolation errors for the "seed" track are computed from the full covariance matrix of the tracks composing the charm candidate. Tracks are attached to the seed track in various combinations and the vertex with the largest number of tracks which has a confidence level of at least 2.5% is accepted as the primary vertex. This algorithm produces a number of chi-squared variables: the χ^2 of the candidate (secondary) vertex, the χ^2 of the primary vertex, and a χ^2 of the fit which determines the distance between the primary and secondary vertexes. In addition, the algorithm returns complete covariance matrices for the found vertexes. This algorithm can not only find primary and secondary vertexes which are very close, it can also find primary vertexes where there is only one track (in addition to the candidate seed track).

3.2 Data Reduction

During the 1987-88 run, E687 took 75 million triggers (60 million were hadronic triggers) which were written onto 1200 9-track magnetic tapes. A reduced data sample is obtained through use of a *skim* process. The skim was run on all the reconstructed data on the Fermilab AMDAHL machine. The $D^{\pm}$'s used in this data analysis were obtained from a skim stream which was designed to keep all Cabibbo-allowed and Cabibbo singly- and multiply-suppressed decays of charmed mesons into all possible combinations of charged kaons, charged pions and K_s's, up to 6 bodies [16]. This skim combines kinematic requirements with vertexing requirements.

For the $D^{\pm} \rightarrow K^{\mp}\pi^{\pm}\pi^{\pm}$ decay, every possible combination of 3 linked tracks with total charge of ±1 is formed. The oppositely charged track is declared the kaon. This three-track group is considered an acceptable $D^{\pm}$ candidate if

a) Its invariant mass is between 1.60 GeV and 2.22 GeV

b) The candidate-driven vertex algorithm is successfully performed on the candidate.

c) The log of the confidence level of the fit of the candidate (secondary) vertex is greater than -5.0 (which corresponds to a confidence level of about 0.00674).

d) The kaon is identified as K definite, K/p ambiguous, or $K/\pi/e$ ambiguous (for momenta greater than 60.8 GeV) AND the significance of separation between the secondary and primary vertexes (L/σ_L) is greater than 2.5

OR

The kaon is identified as anything EXCEPT e definite, π definite, e/π ambiguous, or p definite AND L/σ_L is greater than 5.5.

3.3 $\mathbf{D^\pm}$ Analysis

The $D^\pm \rightarrow K^\mp\pi^\pm\pi^\pm$ sample used for this analysis must necessarily include the requirements from the $D^\pm$ skim. In addition, some of the cuts were made more strict, and an extra cut was applied:

a) The confidence level of the fit of the candidate (secondary) vertex greater than 1%. This exceeds the cut required by the skim.

b) The kaon identified as K definite, K/p ambiguous, or $K/\pi/e$ ambiguous (for momenta greater than 60.8 GeV). This cut exceeds the requirement of the skim.

e) The significance of separation between the secondary and primary vertexes (L/σ_L) greater than 3. This cut exceeds the requirement of the skim.

f) The pions NOT identified as K definite, p definite, or K/p ambiguous.

The power of the candidate-driven vertexing algorithm is demonstrated in Figure 3.2. The data sample is from an early data reduction algorithm which does not use the candidate-driven vertexing algorithm. The background of the sample is reduced by an order of magnitude by requesting a significance of detachment (L/σ_L) of 8 or greater. Figure 3.2also shows a $D^\pm$ signal where there is only one track (in addition to the "seed" track) in the primary vertex.

The $D^\pm$ signal used in this analysis is shown in Figure 3.3.

3.4 Photon Energy Measurement

Crucial to measuring the cross section is the measurement of the photon energy. Assuming a nominal electron beam energy (350 GeV), and measuring the energy of the recoil electron in the RESH:

$$E_{\text{loss}} = E_{\text{beam}} - E_{\text{recoil}} \tag{3.3}$$

(See Figure 3.4). In the case where the "lost" energy is radiated into a number of photons (multi-bremsstrahlung), equation 3.3 does not give the energy of the interacting photon. However, the BGM (the EM calorimeter at zero degrees) will capture the energy of the non-interacting multi-brem photons, which we can subtract from E_{loss} to get the photon energy, ω:

$$\omega = E_{\text{beam}} - E_{\text{recoil}} - E_{\text{BGM}} \tag{3.4}$$

Of course, equation 3.4 will not be accurate if, in addition to the multi-brem photons, there are e^+e^- pairs generated in the incident electron shower. However, the presence of accompanying pairs is not serious for three reasons: 1) extra pairs occur in only about 10% of the electron showers, 2) most of the e^+e^- pairs will be low energy and thus not greatly subtract from the measured photon energy and 3) if the e^+e^- pairs are energetic, the electron will very likely be swept into the RESH along with the original recoil electron, thus causing two separated hits in the RESH, which is vetoed in the second level trigger.

There are several problems associated with measuring the photon energy with equation 3.4. First, the energy of the incident electron is not measured. The secondary electron beam is tuned to an energy of 350 Gev, but the momentum bite is large (about ±13%). Thus, we only "know" the electron energy to about ±45 GeV.

Secondly, the recoil energy measured by the RESH is quantized, since the energy is measured magnetically by the position of the struck cell. The position of the hit cell will measure the bend angle of the recoil electron through the sweeper magnets, and thus the energy of the recoil electron. The recoil electron energy is given as the nominal energy of the cell (the energy of an electron hitting the cell in the center), or, if two adjacent cells fire, the energy of an electron hitting the crack between the two cells. Thus, E_{RESH} is one of 19 different values (10 cells plus 9 cracks between cells). The cells are arranged such that low energy photons "see" more granularity of the RESH measurement. (Figure 3.4.)

Thirdly, there is a significant pile-up problem in the BGM. Thus, the BGM will not only see the multibrem photons, but also stray photons from a piled-up event. Pile-up in the BGM occurs in about 35% of the events. This will artificially lower the energy measurement of the photon.

We attempt to compensate for these effects when we measure low photon energies by comparing the photon energy estimate from equation 3.4 above to the sum of the momenta of the charged tracks in the event. This should be a lower bound on the photon energy, so for low (less than 200 GeV) energy photons, we take the larger of equation 3.4 and E_{tracks}. We chose E_{tracks} approximately 25% of the time.

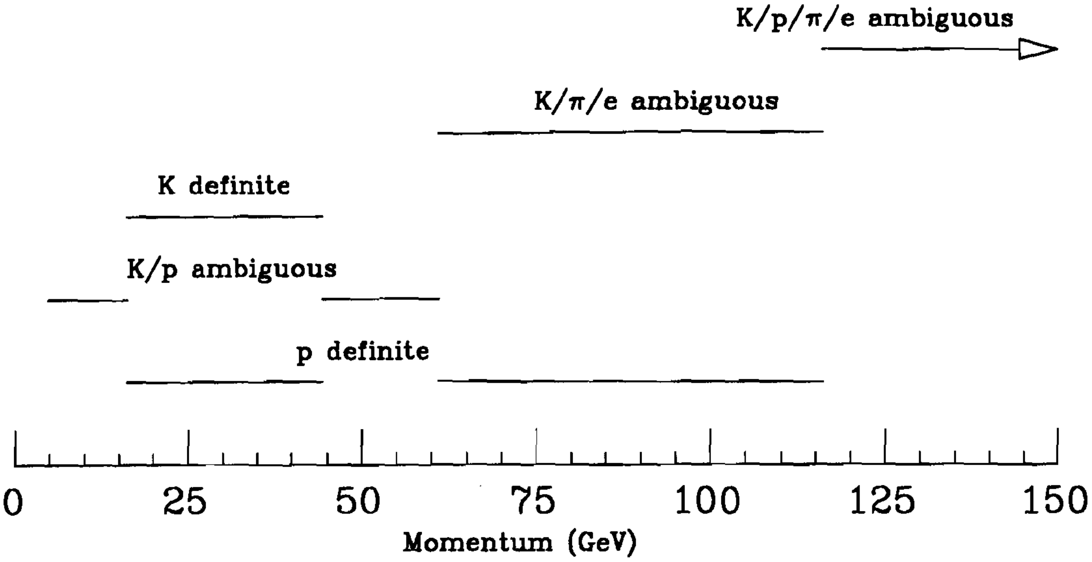

a) Cerenkov ID regions for 5–chamber tracks

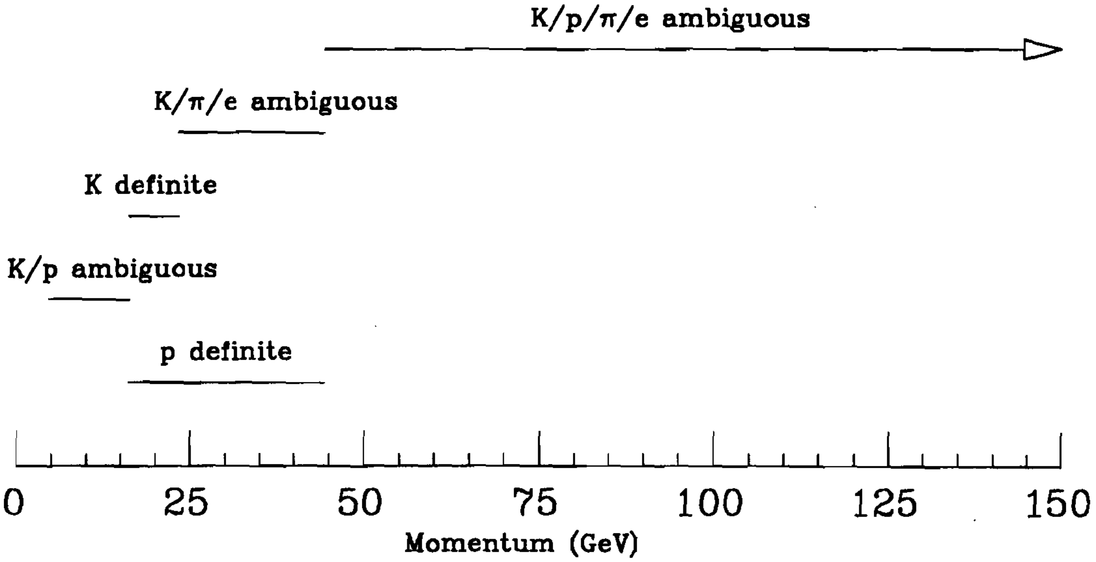

b) Cerenkov ID regions for 3–chamber tracks

Figure 3.1: Momentum ranges where certain Cerenkov identification classes are possible a) for tracks passing through all three Cerenkov counters, and b) for tracks passing through only C1 and C2.

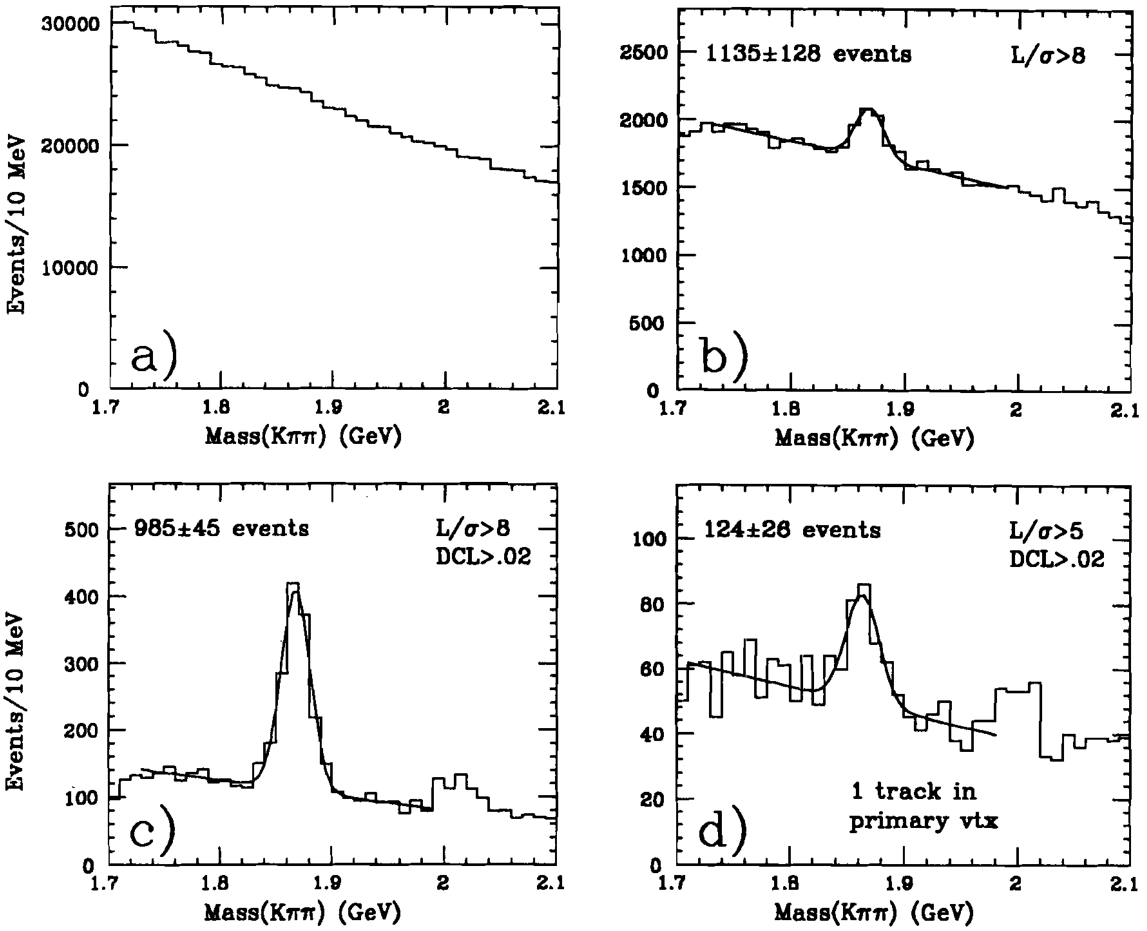

Figure 3.2: These plots illustrate the power of the candidate-driven vertexing algorithm: a) a selection of $K^{\mp}\pi^{\pm}\pi^{\pm}$ events from an early data reduction, which did not use the candidate-driven vertex algorithm. This sample requires only Cerenkov identification on the K (K definite, K/p ambiguous, or if the momentum is above 60.8 GeV, $e/K/\pi$ ambiguous). b) The sample with an additional requirement that the significance of separation (L/σ_L) between the primary and secondary vertexes be at least 8. Notice that the background has dropped by an order of magnitude. c) The sample with the additional cut that the confidence level of the secondary vertex (the candidate vertex) be at least 2%. d) A sample of $D^{\pm}$ events which only have one track (in addition to the candidate "seed" track) in the primary vertex. Stand-alone vertexing algorithms cannot find one-track vertexes.

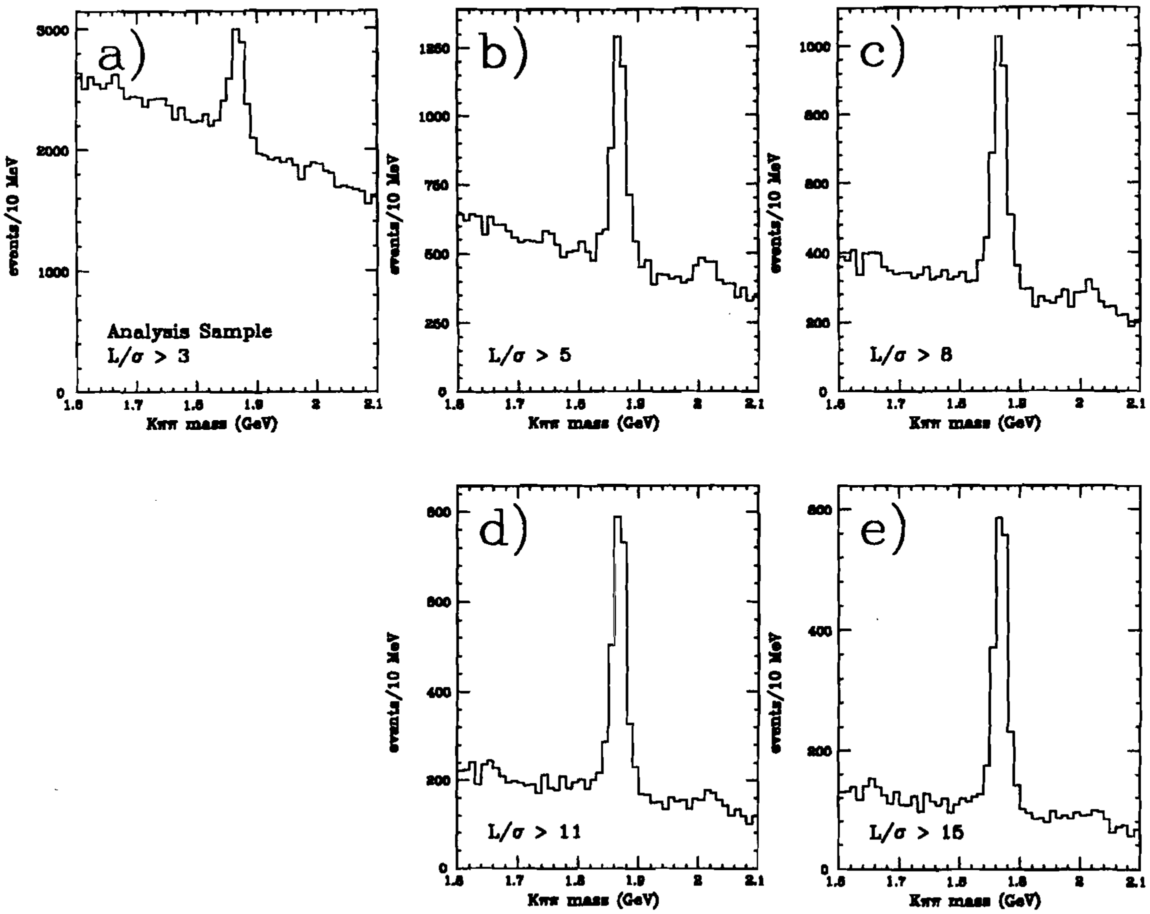

Figure 3.3: a) The general $D^{\pm}$ sample used in this analysis as described in section 3.2, and signals with stricter significance of detachment requirements: b) $L/\sigma_L > 5$, c) $L/\sigma_L > 8$, d) $L/\sigma_L > 11$, e) $L/\sigma_L > 15$. The stricter requirements are used for special applications.

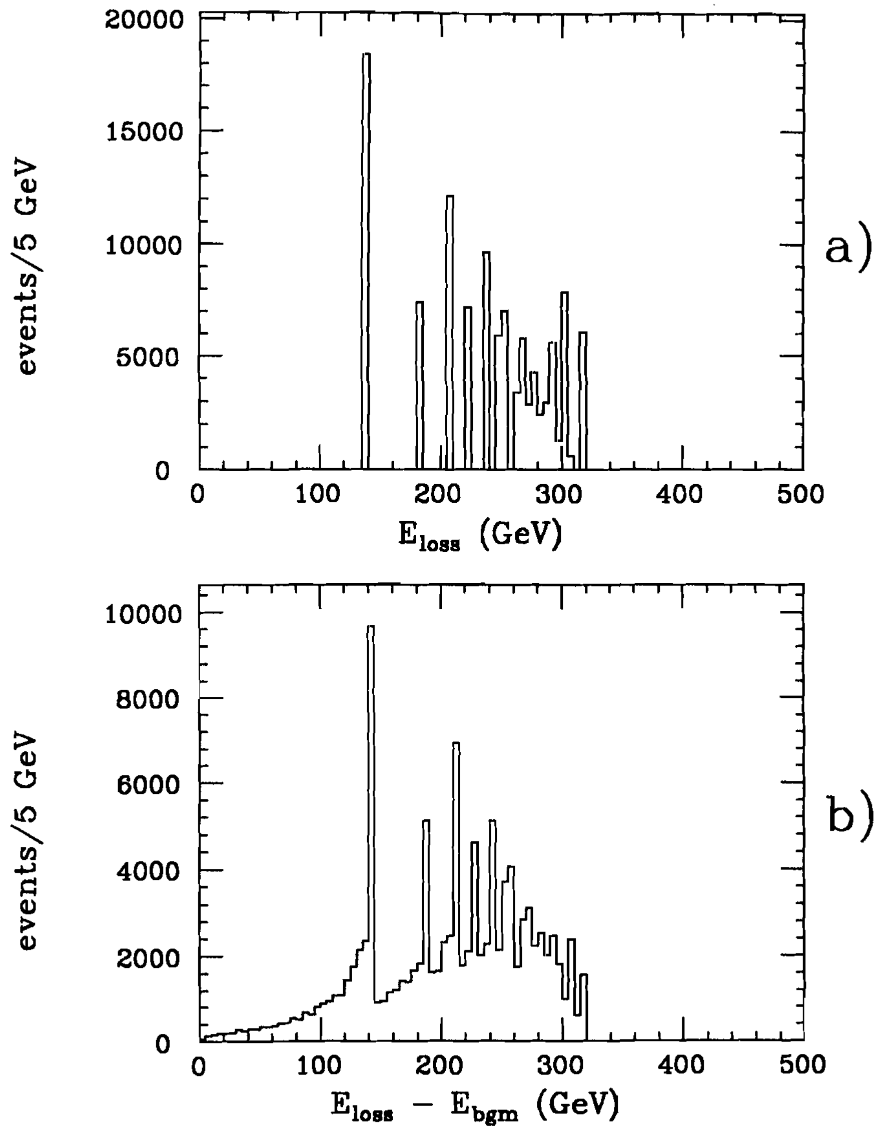

Figure 3.4: a) The E_{loss} energy spectrum, showing the granularity of the spectrum measured by the RESH. b) The measurement of the photon beam energy: E_{loss}- E_{bgm}.

CHAPTER 4

Monte Carlo

The Monte Carlo used for simulating E687 has to be carefully designed to take into account some unique problems. First, the long radiator (which produces the photon beam from the electron beam) will create several photons for each electron shower, causing problems we call *multi-bremsstrahlung complications.* We need to have some mechanism to decide which of the multi-brem photons is to produce a charm interaction. Secondly, our Be targets were very unusually shaped, (Figure 2.3) and the beam spot exceeds the edges of these targets, which cause *targeting correction* problems.

4.1 The Event Generator

Event generation includes all simulation of the incident beam, the production of the primary charm particles, and the decay of all particles. The generation is done by a program called GENERIC, which allows the user to freely choose most of the parameters of the experimental conditions, as well as the production and decay models of the particles.

4.1.1 Beam and Targeting Simulation

GENERIC starts by simulating the electron in the secondary beamline, which will bremsstrahlung to form the photon beam. The electron's energy is given by the experimentally measured distribution. (Measured by running a low intensity electron beam into the BGM.) Figure 4.1 shows the measured electron distribution and the distribution simulated by GENERIC.

In order to simulate the photon flux of the beam, $\Phi(x, y)$ where x, y is the transverse position of the beam, we must assume that the electron profile is the same as the photon beam profile. Because the beam spot is larger than the target segments, $\Phi(x, y)$ is modeled according to primary vertex distributions of photons which interact in the larger scintillator trigger counter TR1, which is just upstream of the microstrips (Figure 2.7). Figure 4.2 shows the x and y vertex distributions in TR1. Clearly the x and y distributions are not independent, the x distribution is more peaked for central values of y. After some experimentation, we found we could model the beam using elliptical probability contours. Since the x beam size is twice as broad as the y beam size, we invent a variable, R:

$$R = \sqrt{(x - x_c)^2 + (2(y - y_c))^2} \tag{4.1}$$

where $(x_c,\ y_c)$ is the center of the beam spot. We assume the beam is azimuthally symmetric in R. This method is called the *R-parameterization* method. An R value is chosen from 0 to R_{max} and an angle from 0 to 2π, and the x and y values calculated. Figure 4.3 shows the R distribution.

The electron then showers, according to 27% radiation length. First, a classical amount of energy is subtracted, to account for radiated photons of energy less than 5 MeV. Then the electron is stepped through the radiator material, according to a mean free path of radiation. The electron is allowed to multiple-scatter. The resulting photons are tested for conversions, and all shower products are traced until the daughters are less than 10 MeV, or have succeeded in exiting the radiator volume.

The dual problems of targeting and multi-brem photon activation can be addressed in the following way. Each of the photons resulting from the electron shower is given a possible interaction point by the x, y position of the radiating electron at the point of radiation, and a z position drawn uniformly from the upstream face of the target to $\Lambda = L_o\ \sigma_o/\sigma_{mc}(\omega)$, where L_o exceeds the maximum length of the target, $\sigma_{mc}(\omega)$ is the cross section energy dependence being simulated by the Monte Carlo and σ_o is a *reference cross section* for dimensionality purposes. The photon interaction point (x, y, z) is activated into a charm particle with activation probability given by:

$$\mathcal{A} = \begin{cases} 0 & \text{if outside the target;} \\ 1 & \text{if inside the target} \end{cases} \tag{4.2}$$

The probability of a photon being activated into a charm particle is then given by:

$$\mathcal{P} = \left(\frac{\sigma(\omega)}{\sigma}\right) \left(\frac{\rho(x,y,z)}{\rho_o}\right) \Phi(x,y)dxdy \, \frac{dz}{L_o} \tag{4.3}$$

where $\rho(x,y,z)$ is the density function of the target, which is 0 outside the target and ρ_o inside the target. By following this prescription, we simultaneously select a charm activation as a function of $\sigma(\omega)$, and properly simulate the targeting.

At this point we have to introduce some complications. One of the experimental targets uses Silicon as well as Beryllium, so we must modify equation 4.2:

$$\mathcal{A} = \begin{cases} 0 & \text{if outside the target;} \\ 1 & \text{if inside Si;} \\ \rho_{(Be)}/\rho_{(Si)} & \text{if inside Be.} \end{cases} \tag{4.4}$$

That is, if the activation point is in Be, it is only activated about 79% of the time. Here, we assume an A^1 dependence of the interaction cross section.

We also correct for the attenuation of the photon beam in z, by vetoing a fraction of activated photons by checking for pair conversion. A conversion location is given as x, y of the photon activation location, and a z_{conv} chosen according to the distribution $\exp(-z_{\text{conv}}/\lambda(\omega))$ where $\lambda(\omega)$ is an energy dependent mean free path where $\lambda(\omega \to \infty) \to (9/7)X_o$, (Figure 4.4) where X_o is the radiation length of the target material. If the conversion location is upstream of the interaction location, then this activation is vetoed.

In the case that two (or more) photons in the same event are both activated into charm, only the last activation is considered valid. The other photon(s) are de-activated.

In any event where there is a photon activation into charm, the accompanying photons are tested for conversions according to the method stated above. If these conversion locations are inside the target volume, then the electron pairs accompany the charmed event. Any unconverted photons also accompany the event.

We keep track of the number of Monte Carlo beam electrons necessary to create the sample of Monte Carlo charm events. We also simulate a BGM counter by incrementing the BGM count for every electron which radiates at least 133 GeV into photons. Of course, the luminosity must be scaled to account for the role of the reference cross section. Derivation of this scale factor can be found in Appendix A.

4.1.2 Charm Particle Generation

Once a photon energy is chosen, the charm particles can be produced. For this analysis, a $P_\perp^2$ distribution is simulated according to results from Fermilab experiment E691 [17]:

$$dN/d(P_\perp^2)_{mc} \propto \exp(-1.07P_\perp^2)$$

An x_f (the longitudinal momentum in the center of mass frame divided by the maximum possible longitudinal momentum) is also chosen with a distribution given by the parameterization of E691:

$$x_f \propto (1+9x_f)(1-x_f)^{2.63}$$

The $P_\perp$ and x_f determine the momentum of the $D^\pm$.

The particles decay according to an appropriate matrix element, generally just phase space. Additional decay matrix elements are available for semi-leptonic decays, resonance decays, and special decays (such as pseudo-scalar to vector plus pseudo-scalar, or vector to three pseudo-scalars).

4.1.3 Additional Event Particles

Backward jets are created according to the Feynman-Field prescription [18] to add particles to the primary vertex. The jets are propagated with respect to the overall center of mass with energy of $\sqrt{s}/2$. Occasionally, two separate events (caused by two separate beam electrons) are observed in the same gate. In this case, the second "piled-up" event is virtually always a photon conversion. We call these conversions embedded pairs. These conversions are different from multi-bremsstrahlung conversions, in that the vertex location is not correlated at all with the charm interaction vertex. To mimic this effect in the Monte Carlo, embedded pairs are added to 17% of the events. For expediency, a photon is generated with a simple energy spectrum, $1/\omega$. The energy is divided between the electron and the positron according to a flat distribution. A vertex location is chosen randomly in the target volume.

4.2 Event Simulation

The event simulation is done by a program called ROGUE. This program simulates responses of the spectrometer devices to the particles, as well as the particles responses (magnetic deflection, multiple Coulomb scattering, etc.,) to the spectrometer.

The basic philosophy of ROGUE is to trace each particle in turn, by stepping the particle to specified stopping locations, until the particle uses up its given decay path, fails to clear an aperture, or leaves the spectrometer. Stopping locations are points where some action must be undertaken: at wire chamber planes to simulate hits, at specified points for multiple scattering, at the aperture of a device to determine if the particle is accepted by it. When all the particles are finished being tracked, then the event is "digitized", and written to tape.

4.2.1 Tracking

Charged particles are traced through the spectrometer with a TURTLE tracing procedure: the deflection of the particle is determined according to its momentum and the magnetic field that it is experiencing.

At each SSD plane, a SSD hit is simulated. The amount of charge deposited is given by a Landau distribution, fit to microstrip data. Charge sharing between strips is given by a simple geometrical model based on the thickness of the ionization cloud and the intersection of the track with the detector plane [19]. Multiple scattering occurs at the middle plane of the stack. Before digitizing, spurious hits are added according to a Gaussian noise distribution.

At each PWC plane, the relevant coordinate is stored for later digitizing. For each hit, the adjacencies are determined. Each plane is characterized by an adjacency fraction, a_f, which is how often a hit is associated with an adjacent hit. These numbers are measured from the data, and are typically 4-6%. A band of width $a_f \Delta w$ (where Δw is the wire spacing) in the central region between two wires is the *adjacency region.* Any track passing in the adjacency region will cause hits in both wires.

Before digitizing, some hits are removed to simulate chamber inefficiency. Each plane has a characteristic efficiency, calculated from the data (about 80-98%). If a removed hit has an adjacency, the adjacency is removed also.

Certain locations are set up as multiple scattering stops. At these locations, the particle's direction is changed by adding $\Delta x'$, and $\Delta y'$ to the x and y slopes where $\Delta x'$, and $\Delta y'$ are gaussian distributions with width:

$$\sigma_{\mathrm{MCS}} = \frac{.014 \text{ GeV} \sqrt{L_R}}{\mid P \mid} \tag{4.5}$$

Where L_R is the radiation length of the multiple scattering volume being simulated, and $\mid P \mid$ is the magnitude of the particle's momentum. At multiple scattering stops, electrons and positrons also undergo bremsstrahlung.

Neutral particles are also moved through the spectrometer, stopping only for apertures and calorimeters.

4.2.2 Cerenkov

Charged tracks which pass through the Cerenkov counters, and which are above threshold, will throw off photons according to the mean free path of Cerenkov radiation in the particular counter. These photons are then traced to the mirrors, reflected and traced into the collection cones (if any) to the photomultiplier tube. Inefficiencies due to radiator transparency, mirror reflectivity, and photocathode quantum efficiency are all considered (averaged over wavelength). Electronics noise is not simulated in the Cerenkov counters.

4.2.3 Triggers

The H×V and OH scintillators are set "on" with probability according to their measured efficiency each time a charged particle strikes the counter. The measured efficiencies are generally 95-98%. The Master Gate, which initiates the data aquisition process, is formed using the H×V and OH signals (see equation 2.1.a). The T trigger (see equation 2.1.b) is assumed to be 100% efficient.

To simulate the RESH response, we calculate the x position of the recoil electron at the RESH counter. The energy is shared among the hit and adjacent cells. The second level trigger required a signal in the RESH consisting of 1, 2, or 3 adjacent RESH cells to be "on" (RESHLO trigger) as determined by the electromagnetic shower response. The cells are "on" if the deposited energy in the cell is more than 20% of the the energy of a nominal recoil electron which would hit the center of the cell as determined magnetically by its bend in the sweeper magnet.

The hadronic (HC) trigger response is simulated by adding the total energy of charged particles which hit the face of the Hadron Calorimeter, except for the energy of electrons, and positrons, which is assumed to be absorbed in the IE, and muons which are assumed to deposit no energy in the hadrometer. The trigger is simulated according to a parameterization of the trigger efficiency as a function of the sum of the momenta of charged tracks hitting the HC (not including tracks which go through the hole in the center.) [20]. The data and fits for the HC trigger efficiency are shown in Figure 4.5 for different running periods.

The multiplicity trigger is "on" if there is at least one hit in P0X outside the central region (pair region).

The second level trigger requires the Master Gate, RESHLO trigger, HC trigger, and the multiplicity trigger to all be "on".

4.3 Run Period Simulation

The various changes in triggering, performance, and targeting conditions were reflected in the Monte Carlo. The 1987-88 data run is divided into 8 run periods. These run periods are delineated by downtimes, target changes, or beam changes. Important differences in these run periods are considered by the Monte Carlo:

1. Target type.

2. Target location.
3. Beam location.
4. PWC efficiency.
5. HC trigger efficiency.

In order to simulate the targeting properly, trigger efficiency, and reconstruction efficiency, (crucial for measuring cross sections,) the Monte Carlo simulates a "mini-data-run". GENERIC selects a run period for each beam electron simulated. The run periods are distributed proportional to their luminosity in the data.

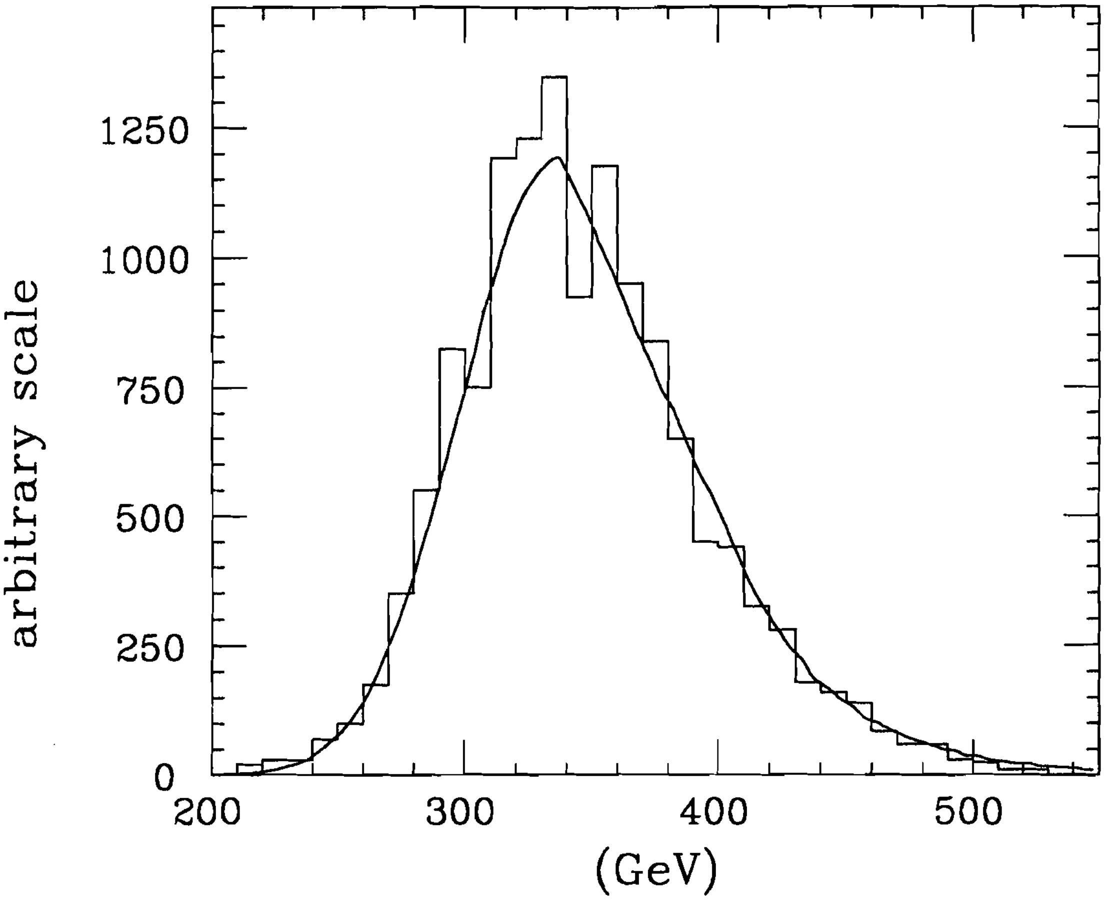

Figure 4.1: The measured energy distribution of the electron beam (histogram) and the distribution simulated in the Monte Carlo (curve).

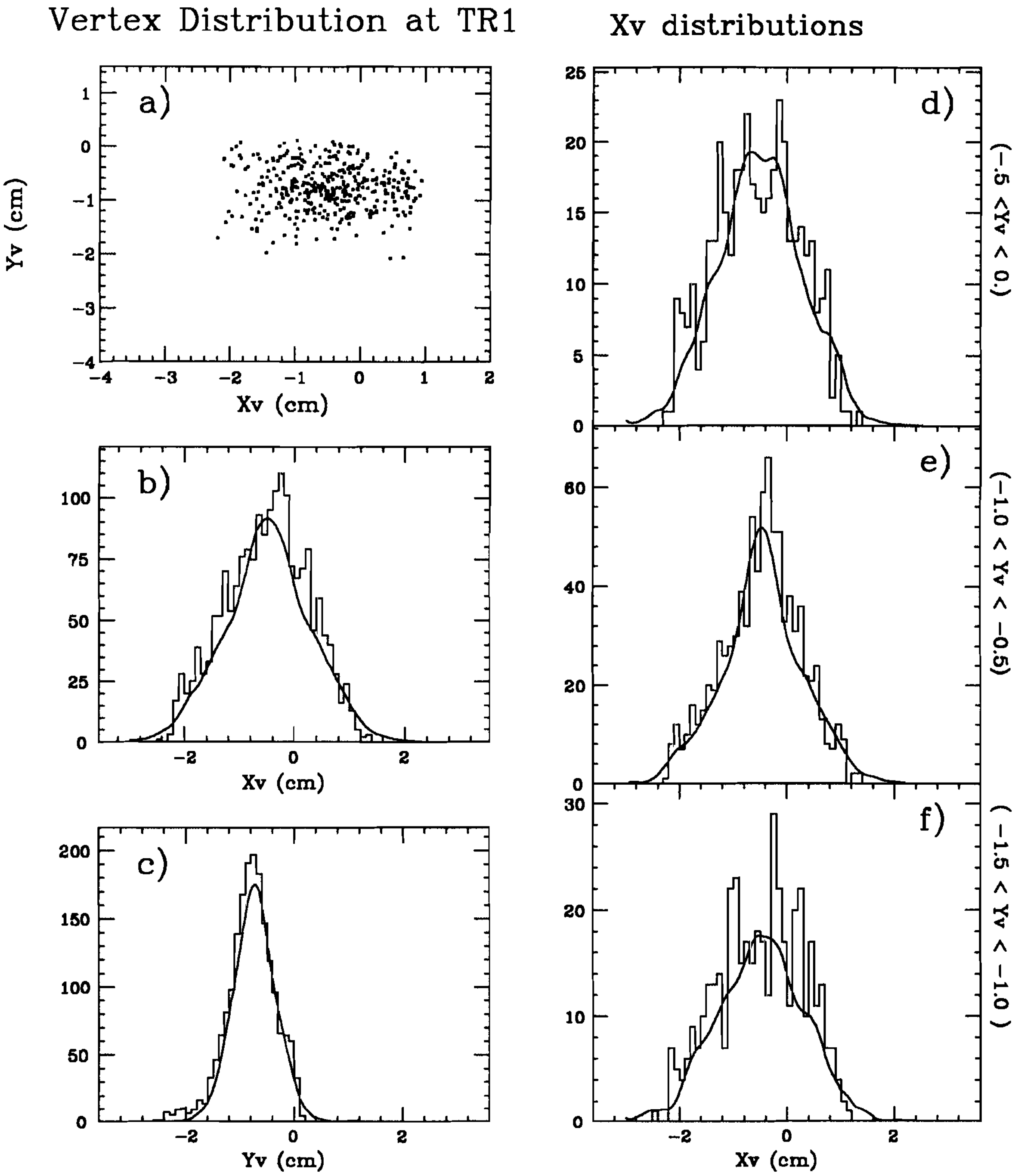

Figure 4.2: a) Vertex distribution of interactions in the TR1 trigger counter (which gives the photon flux $\Phi(x, y)$). The top edge is clearly visible. b) x distribution of interactions in TR1 (the histogram is the data, and the curve is the Monte Carlo simulation.) c) y distribution. Again the edge of the counter is visible. d)-f) x distributions for different slices in y. Clearly the x distribution is not independent of y.

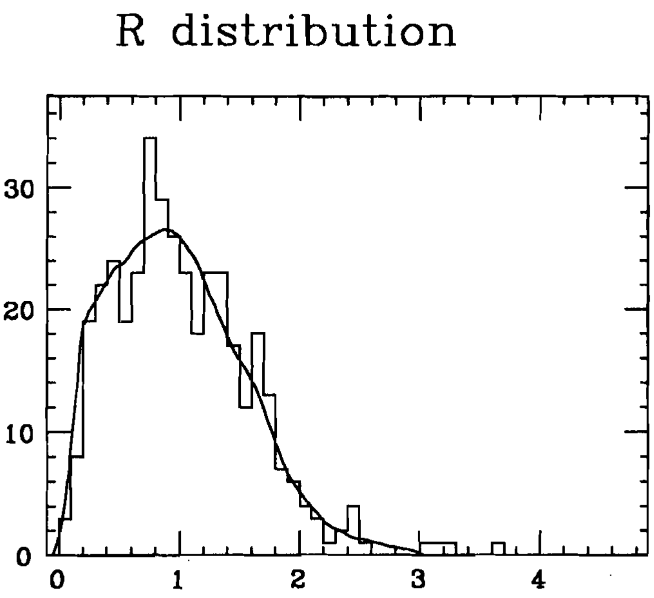

Figure 4.3: The measured (histogram) and simulated (curve) R-distribution, as described in the text.

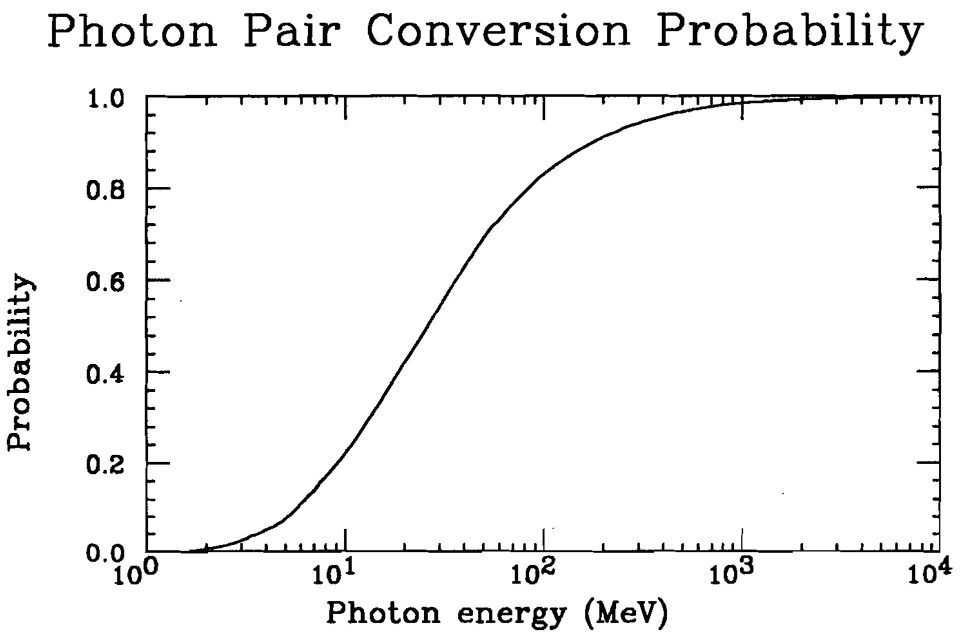

Figure 4.4: Photon conversion probability as a function of energy.

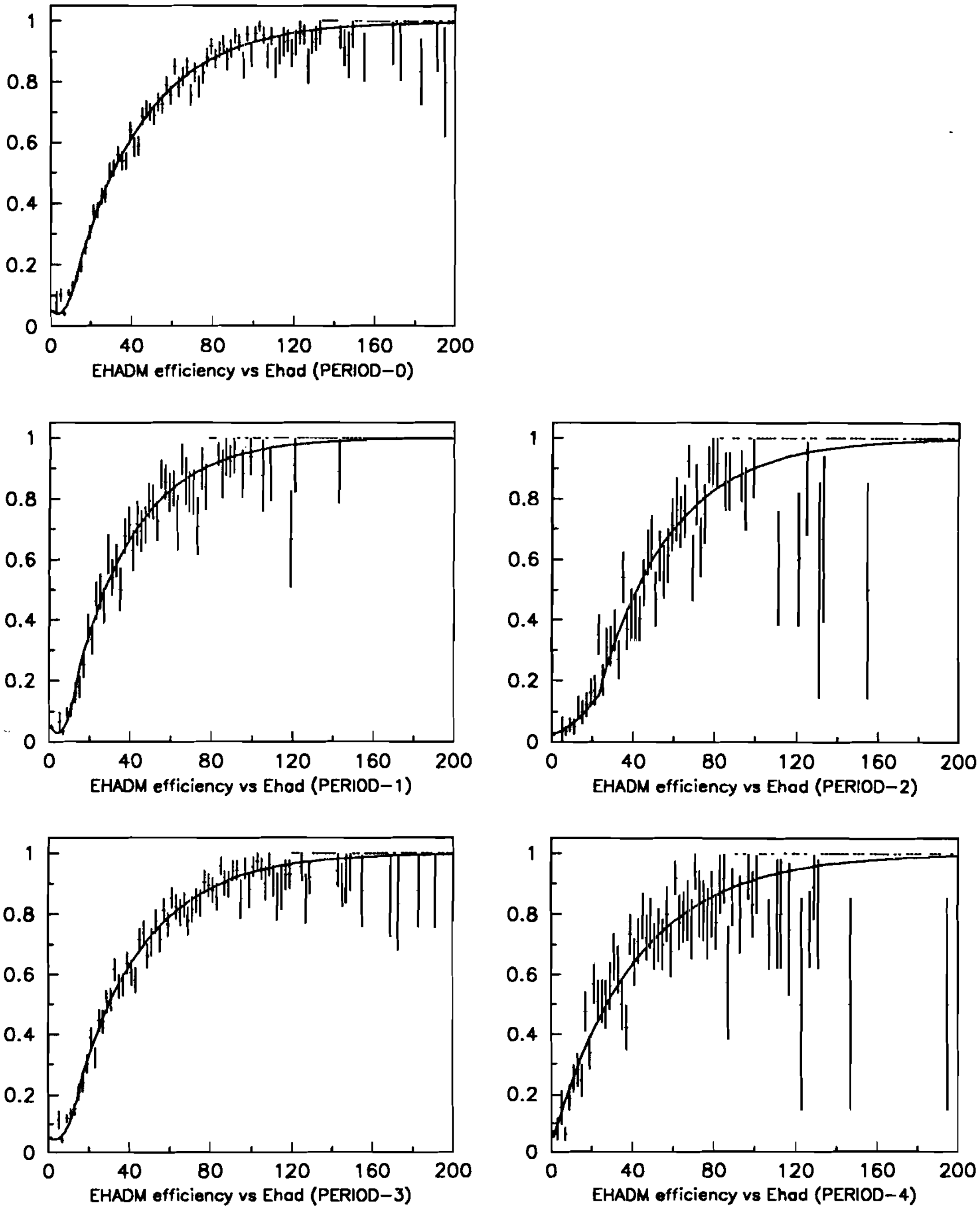

Figure 4.5: The Hadrometer trigger (EHADM) efficiency as a function of the sum of the momenta of the tracks hitting the face of the HC (Ehad) for different run periods.

CHAPTER 5

$D^{\pm}$ Cross Sections

5.1 Problems Caused by Poor Resolution

We would like to measure the $D^{\pm}$ photoproduction cross section as a function of photon energy (ω) and the differential cross section ($d\sigma/dx_f$) as a function of Feynman x (x_f). Feynman x is given by:

$$x_f = \frac{E_D}{\omega} - \frac{E_D^2 - P_z^2}{2m_N\, E_D} \tag{5.1}$$

where E_D is the lab frame energy of the $D^{\pm}$, P_z is its longitudinal momentum, and m_N is the mass of the target nucleon. For $x_f > 0.25$, $x_f \approx P_D/\omega$, where P_D is the total lab frame momentum of the $D^{\pm}$. The momentum is well-determined, but the photon energy is uncertain to ±45 GeV. Therefore, the uncertainty on x_f is:

$$\sigma_{x_f} \approx \frac{45\mathrm{GeV}}{\omega}\, x_f \quad \text{for} \quad x_f > 0.25 \tag{5.2}$$

For example, for a photon energy of 150 GeV, equation 5.2 implies a 30% uncertainty in x_f, which is more than ± 0.2 for x_f greater than $x_f = 0.70$. Uncertainty of ± 0.2 is large on the scale of the anticipated fall-off of $d\sigma/dx_f$ at large x_f.

The serious resolution effects in ω and x_f pose serious problems in measuring the cross section and differential cross section. An event measured at $x_f{}^*$ and ω^* will not give direct information about the cross section at $x_f{}^*$ and ω^*, because each measured $x_f{}^*$ represents a *range* of true x_f values. Similarly, the number of events in a given ω^* range reflects the cross sections over a large range of true ω values. In addition, poor resolution gives rise to correlations between cross section ranges. Consider two Δx_f bins which are completely unresolvable from each other. The number of data entries in one bin will not only be affected by the cross section in that bin, but also by the cross section in the adjacent bin. The two bins will be highly negatively correlated: the sum of the cross sections will be well determined, but the difference will not be, due the the sloshing of events from one bin to the other. In the limit where the bins are nearly completely unresolvable, the errors on the cross section will be much larger than the statistical error on the number of events in a bin. The method we use for finding cross sections uses a Monte Carlo to determine the true x_f, ω ranges represented by certain measured ${x_f}^*$, ω^* ranges, and then the cross section is *unfolded* from the resolution effects [21]. The unfolding process will take into account the enhanced errors due to correlations between bins.

5.2 Method for Measuring Cross Sections

We bin the data in joint bins of the measured quantities Δx_f^* and $\Delta\omega^*$ (the superscript * indicates measured quantities). Thus, if we have 4 x_f bins and 3 ω bins, there will be $3 \times 4 = 12$ measured $(\Delta x_f^* \Delta\omega^*)$ bins.

The number of events produced in the α'th true $\Delta x_f \Delta\omega$ bin (Greek indices will indicate true quantities, and Roman indices will indicate measured quantities) will be the average cross section for that bin times an appropriate luminosity factor and efficiency for that bin:

$$n_\alpha = \mathcal{L}_\alpha \, \epsilon_\alpha \, C_\alpha \tag{5.3}$$

There will be a *measurement matrix*, $K_{i\alpha}$, which transforms events which actually occur in the α'th bin into events in the i'th measured bin. The number of events that are found in the i'th bin is then:

$$\begin{aligned} n_i &= \sum_\alpha K_{i\alpha} n_\alpha = \sum_\alpha K_{i\alpha} \mathcal{L}_\alpha \, \epsilon_\alpha \, C_\alpha \\ &= \sum_\alpha R_{i\alpha} C_\alpha \end{aligned} \tag{5.4}$$

In general, the solution of equation 5.4 is a linear transformation:

$$C_\alpha = \sum_i \rho_{\alpha i} \, n_i \tag{5.5}$$

In the case where the number of measured bins is the same as the number of true bins, then the solution to the cross section problem is exactly constrained:

$$C_\alpha = \sum_i R^{-1}_{i\alpha} n_i \tag{5.6a}$$

that is,

$$\rho_{\alpha i} = R^{-1}_{i\alpha} \tag{5.6b}$$

In general however, a fit for the the cross section given a redundant number of n_i data entries is found by minimizing the following χ^2 (once the $R_{i\alpha}$ matrix is computed from Monte Carlo):

$$\chi^2 = \sum_i \frac{(n_i - \sum_\alpha R_{i\alpha}\ C_\alpha)^2}{n_i}$$

The solution to this standard minimization problem gives:

$$\rho_{\alpha i} = \sum_\beta \frac{H^{-1}_{\alpha\beta}\ R_{i\beta}}{n_i} \quad \text{where} \quad H_{\alpha\beta} = \sum_i \frac{R_{i\alpha}\ R_{i\beta}}{n_i} \tag{5.7}$$

Equation 5.7 represents the optimal variance solution when all variables are Poisson distributed and uncorrelated, and there is no background.

In order to count the number of $D^\pm$'s which occur in a particular bin, we need to incorporate some sort of background subtraction in our technique. In principle, one could make invariant mass plots for each measured $\Delta x^*_f \Delta\omega^*$ bin, fit the signal peak to find n_i, and then multiply by the ρ matrix to calculate C_α. An alternative is to make separate weighted histograms for each desired C_α measurement. An event is entered into a given α histogram with a weight of $\rho_{\alpha i}$, where i is the measured bin that the event falls into. The resulting histogram will have a signal peak over a smooth background. The area under the peak, $< \rho_{\alpha i} n_i >$, will be the model independent, unbiased, background-subtracted estimator for C_α according to equation 5.5.

In actual practice, we do not wish to measure cross sections for individual $\Delta x_f \Delta \omega$ bins, rather we wish to make a histogram for each, say, Δx_f bin, where the $\Delta \omega$ bins have been summed over. The weighted histogram scheme is ideal for this purpose. The individual weights for the α bins belonging to the concatenated "super-bin" are added, forming a "super-weight". The event is added once to the super-bin cross section histogram weighted by the super-weight.

5.3 Constructing the $\mathbf{R}_{i\alpha}$ matrix

We construct the $R_{i\alpha}$ matrix from Monte Carlo. Since the Monte Carlo adequately (we hope) simulates the experimental apparatus and analysis procedures, the measurement matrix, $K_{i\alpha}$, and the efficiency function, ϵ_α, are the same as for data. Similarly, we assume that the Monte Carlo properly simulates the photon spectrum. Then the $R_{i\alpha}$ matrix will be the same for Monte Carlo and data, except for a factor normalizing the total luminosity:

$$R_{i\alpha} = \frac{\mathcal{L}_{tot}^{(dat)}}{\mathcal{L}_{tot}^{(mc)}} R_{i\alpha}^{(mc)} \tag{5.8}$$

Since the normalization factor is a ratio, we can chose any luminosity indicator that we want. Our choice, the BGM scaler, is justified in section 5.5.

We now turn to a discussion of how the $R_{i\alpha}$ and $\rho_{\alpha i}$ matrices are computed by the Monte Carlo. The basic idea is to increment a matrix, $G_{i\alpha}$ for each event which falls in the true α'th bin, and is measured in the i'th bin, then

$$R_{i\alpha}^{(mc)} = \frac{G_{i\alpha}}{C_\alpha^{(mc)}} \tag{5.9}$$

The $C_\alpha^{(mc)}$ is the Monte Carlo cross section used to simulate data, and is given by:

$$C_\alpha = \int_{\omega_{1\alpha}}^{\omega_{2\alpha}} d\omega \int_{x_{1\alpha}}^{x_{2\alpha}} dx \, \frac{d\sigma}{dx}(x,\omega) \tag{5.10}$$

5.4 Error Calculation

We have assumed that the signal errors are Poisson distributed and uncorrelated such that:

$$< \delta n_i \; \delta n_j >= n_i \delta_{ij} \tag{5.11}$$

The anticipated errors for the cross section fit are:

$$< \delta C_\alpha \; \delta C_\beta >= \sum_i \rho_{\alpha i} \; n_i \; \rho_{\beta i} \tag{5.12}$$

The error on C_α will be:

$$\sigma(C_\alpha) = \sqrt{\sum_i n_i \rho_{\alpha i}^2} \tag{5.13}$$

From this we see that the variance on C_α is the sum of all weights in a bin added in quadrature. This is the standard way of computing errors in a weighted histogram, which means that the error in the signal peak in the weighted histogram will be the error on C_α. If one fits the weighted mass plot with standard weight errors for each mass bin, then the error in the area under the invariant mass peak will reflect **both** the errors from equation 5.13 as well as the additional error caused by the background.

In addition to these errors there will be some error associated with the finite statistics of the Monte Carlo, with which was made the $\rho_{\alpha i}$ matrix. If we include the Monte Carlo errors, then the errors on the cross sections given by equation 5.13 should be modified:

$$\sigma(C_\alpha) = \sqrt{\sum_i n_i \rho_{\alpha i}^2} \; \sqrt{1 + N_{data}/N_{mc}} \tag{5.14}$$

(See Appendix B.) Since we typically have 10 times the Monte Carlo sample as data, the error must be scaled by about 1.05.

5.5 Luminosity

To monitor luminosity, a scintillator counter (BT) counts electrons in the secondary beamline. Unfortunately, this counter will also count pions which contaminate the beamline, but which do not contribute significantly to the photon flux. The BT counter has also been shown to have a pile-up problem at high rates; a problem due to multiply occupied rf buckets.

Thus, due to the difficulty of understanding the BT counter, we use the Beam Gamma Monitor (BGM) as a luminosity counter. Its signal is counted every time there is at least 133 GeV deposited in the BGM. Since the BGM counts photons, the count is not compromised by the pion contamination in the secondary beamline. There is also less problem with pile-up: two electrons which arrive within the resolving time of the BGM scaler can cause a maximum of one count in the BGM, but the photon radiation from the two electrons is more likely to exceed the BGM threshold than photon radiation from one electron. These competing effects will cancel, as shown in Figure 5.1.

The BGM rate is artificially depleted when photons destined for the BGM are absorbed (pair-produce) in the spectrometer. A simple Monte Carlo is used to determine these effects. Uninteracted photons are traced through the spectrometer. If the photon pair-produces in the spectrometer then the electrons are traced through the spectrometer. In some cases, one or both of the electrons are focussed back to the BGM, where their energy is deposited. This Monte Carlo shows that the number of BGM counts should be multiplied by 1.044 for the 4-Be target, 1.055 for the 5-Be target, and 1.079 for the Si target to get the true number of times an electron from the secondary beamline gives off at least 133 GeV's worth of photons.

The recorded counts in the BGM must be corrected not only for the absorption factor, but also for livetime. Photons which arrive during the deadtime of the experiment do not exist as far as luminosity is concerned. The livetime for this experiment is typically 75%, which is measured by comparing a free-running $((H \times V)_{\geq \mathbf{1body}} \cdot OH) \oplus (H \times V)_{\geq \mathbf{2body}})$ to one which is inhibited during the experimental deadtime.

For each spill found in the data sample, the relevant entry in the Spill Scaler Record is looked up. If the BGM count is in the record, it is multiplied by the relevant absorbtion-correction factor, and adjusted for livetime. A running sum is kept of the total. For about 5% of the spills, no BGM scaler entry is found (due to hardware glitches, etc.) We estimate the BGM counts for the spill by using the average BGM counts for the particular run period.

5.6 Results

The $D^{\pm}$ sample used to measure cross sections includes the general requirements previously explained, plus several additional cuts. First, we wish to clean up the signal a bit more, so we apply a harder significance of detachment cut: $L/\sigma_L > 5$. Two cuts are added to ensure that the data sample passes the same trigger requirements as the Monte Carlo:

1. The second level trigger in data includes not only the hadronic energy trigger, but also prescaled Master Gate, muon pair trigger, etc. Since the Monte Carlo does not simulate any of these triggers, events are required to satisfy the hadronic energy trigger.
2. During certain times in the data run, the RESH requirement was removed from the second level trigger. Events from these run periods are kept only if the RESHLO trigger requirement is satisfied in addition to the second level trigger requirement.

Two other cuts were added to ensure the quality of the data sample:

3. Several reconstructed tapes (20%) were mis-written, so that BGM energy information was unavailable. Since we do not want to bias our photon energy estimation by ignoring or inventing BGM information, we remove these tapes from the data sample.
4. Luminosity information was unavailable for a few runs. Data from these runs is ignored.

In total, the sample includes about 1760 $D^{\pm}$ events and is shown in Figure 0.1. When making the C_α weighted histograms, we choose to histogram the *normalized mass difference*, $(m_D - m_{meas})/\sigma_m$. This is because the mass resolution can be a function of the $D^{\pm}$ momentum, and thus x_f. The fit for the normalized mass difference can be constrained so that the gaussian width equals 1.

The i and α bins are chosen to be the same. We chose ω bins so that their width is approximately twice the ω resolution. The exact bin boundaries take into account the structure inherent in the measured photon spectrum. Because the RESH measures only quantized energies, the ω spectrum will have spikes (Figure 0.2). The subtraction of of the BGM energy smears these spikes toward lower energies. We chose bins so that spikes and their smears are included in the same bin. The bins are

$x_f$bins	ω bins (GeV)
0.0 - 0.2	100 - 184
0.2 - 0.45	184 - 261
0.45 - 0.65	261 - 350
0.65 - 1.0	

The $D^{\pm}$ signal, partitioned into these bins, is shown in Figure 5.4.

The Monte Carlo sample includes about 19,000 reconstructed D events. These events were generated with a linear cross section for photon energies above 50 GeV; the slope was based on early cross section calculations:

$$\sigma(\omega)_{mc} \propto \frac{1.94}{\text{GeV}} (\omega - 50 \text{ GeV})$$

The generated x_f distribution is described in detail in Chapter 4. The $D^{\pm} \rightarrow K^{\mp}\pi^{\pm}\pi^{\pm}$ proceeds according to three-body phase space. The recoil state is chosen to be a generic charm quark, which is allowed to be any of the well-established charm mesons or baryons. For bookkeeping simplicity, care was taken to ensure that the recoil charm particle did not at any time produce a $D^{\pm} \rightarrow K^{\mp}\pi^{\pm}\pi^{\pm}$ decay.

To compare the Monte Carlo model to the data, we can bin the Monte Carlo as we did for the data in Figure 5.4, fit for the number of $D^{\pm}$ in each bin, and divide by the total. This will give a *fractional yield* for each bin. We can compare to the fractional yield of data for each bin:

Table 5.1: Fractional yield for Data (Monte Carlo)

	ω = 100 - 184	184 - 261	261 - 350 GeV
x_f= 0. - 0.2	3.7 ± 1.0% (3.1%)	10.2 ± 1.6% (8.2%)	3.2 ± 0.9% (4.8%)
0.2 - 0.45	16.9 ± 1.6% (11.6%)	23.5 ± 2.1% (22.7%)	7.1 ± 1.0% (11.2%)
0.45 - 0.65	7.7 ± 1.0% (8.2%)	10.6 ± 1.2% (11.4%)	4.1 ± 0.6% (4.4%)
0.65 - 1.0	5.5 ± 0.8% (4.3%)	4.3 ± 0.7% (4.6%)	0.8 ± 0.3% (1.2%)

The Monte Carlo was run without any absorption of tracks. This will make the efficiency of the Monte Carlo artificially high with respect to the data. The absorption can be added to the Monte Carlo in a post hoc fashion during the analysis. For each track in a $D^{\pm}$ decay, its probability of absorption is calculated, by the distance it travels in the target and the meson absorption length. The absorption length is pretty much the same for kaons and pions, and is independent of momentum in the momentum ranges we deal with. This absorption calculation shows that about 8% of the Monte Carlo $D^{\pm}$ signal will vanish due to absorbtion, thus we will have to multiply our measured cross sections by 1.08 to take into account this effect.

In addition, the Cerenkov efficiency for identifying the kaon in the Monte Carlo is better than for the data. Since the efficiency difference is independent of momentum, we can compensate for this effect by scaling the final cross sections. The scale factor is determined experimentally with D^o's from D^* decay [22]. Since a clear D^o signal without Cerenkov identification is easily obtained by cutting on the D^*-D^o mass difference, the effects of the Kaon identification requirement can be determined. The scale factor due to Cerenkov efficiency is about 1.21.

The combined scale factor for absorption and Cerenkov effects is thus 1.30. This factor will be applied to our measured cross sections. These effects will also contribute to the systematic error.

The weighted histograms of the normalized mass difference for the various C_{α}, as well as the fit to to signal peak, are shown in Figure 5.5. The cross section results are shown in Figure 5.6. The measured cross sections are for inclusive D^+ and D^- per Be nucleus times the branching ratio for $D^{\pm} \rightarrow K^{\mp}\pi^{\pm}\pi^{\pm}$. The cross section as a function of photon energy includes the x_f region from 0. to 1. We have included a systematic error of 30%, added in quadrature. (See section 5.7.)

The measured cross section for inclusive $D^{\pm}$ is determined to be

$$\mathrm{BR} \cdot \sigma = 0.368 \ \pm 0.073 \ \pm 0.111 \ \mu\mathrm{b/Be\ nucleus}$$

at our average photon energy of 220 GeV.

A recent photoproduction experiment at the Fermilab Tagged Photon Lab [17] published a $D^{\pm}$ inclusive cross section of 1.34 ± 0.03 ± 0.23 μb/Be nucleus, for $x_f > 0.2$ at their average energy of 145 GeV. From their parameterization of the cross section as a function of x_f, we find that about 34.3% of their cross section is between $x_f = 0.$ and $x_f = 0.2$. We must scale their cross section by 1.52 to account for the the fraction between $x_f = 0$ and $x_f = 0.2$. Multiplying by the branching ratio that they used, 9.1%, their $\mathrm{BR} \cdot \sigma$ becomes 0.186 ± 0.031 μb/Be nucleus, where the systematic and statistical error have been added in quadrature and scaled by the same factor as the cross section. The value measured in this analysis for 142 GeV is 0.242 ±0.034 ±0.073 μb/Be nucleus. This number is consistent with the E691 measurement, within errors.

Most of the published cross section results are for total $c\bar{c}$ production. To prepare the E687 result for comparison with these published results, we must first divide out the branching ratio of the decay $D^{\pm} \rightarrow K^{\mp}\pi^{\pm}\pi^{\pm}$ to get the total inclusive cross section for $D^{\pm}$. (We use the currently accepted value of 7.9%.) We must then invoke a scale factor which is the inverse of the fraction of the total $c\bar{c}$ cross section which is $D^{\pm}$. The E691 total $c\bar{c}$ cross section at 145 GeV is approximately 4.93 μb/Be nucleus [17]. Comparing the E691 $c\bar{c}$ cross section to their $D^{\pm}$ cross section (corrected for their x_f range), the E691 scale factor from $D^{\pm}$ to $c\bar{c}$ cross sections is 2.42. We will apply that scale factor to this analysis. The resulting estimated $c\bar{c}$ cross sections from this analysis are shown with other cross section measurements, as well as the PGF cross section calculations of Ellis and Nason [10], in Figure 5.7.

5.7 Systematic Error

There are many factors which will contribute to the systematic error of the cross sections. We try to pay particular attention to factors which will make our measured cross section larger than the true cross section, because E687 measurements tend to be somewhat higher than other measured results.

1. Since the beam profile, $\Phi(x, y)$ was measured with devices which were not adequately large for the task, the R-parameterization of the $\Phi(x, y)$ could inadequately describe the true beam profile. If for instance, we over-attribute the beam to the halo section, then the luminosity-to-charm ratio will be low in Monte Carlo compared to data. This means that our cross section measurement is higher than the true cross section. If however, there is more beam halo in data than we are describing in Monte Carlo, then our current measured cross section is lower than the true cross section.
2. The Hadron Calorimeter trigger is not well understood. At a certain point in the running the Central Hadron Calorimeter, CHC, was accidentally removed from the energy sum which constituted the hadronic energy trigger. With the central region missing, the HC trigger effectively becomes a transverse energy trigger. Since the transverse energy for charm is larger than for the ordinary hadronic events with which the HC trigger was parameterized, the HC trigger could actually be more efficient in charm data than in Monte Carlo, which means that our measured cross section is higher than the true cross section.
3. Similarly, charm events will be kaon rich. Kaons will leave less energy in the Inner Electromagnetic counter (immediately upstream of the HC), and thus deposit more energy in the HC, again making the HC trigger efficiency greater for charm data than for the ordinary hadronic events with which HC trigger was parameterized. Again, this means that our measured cross section is higher than the the true cross section.
4. If noise in the PWCs adversely affects our ability to reconstruct tracks, then the Monte Carlo track reconstruction efficiency will be artificially high. Again, this causes our measured cross section to be lower than the true cross section.

5. Since the P4 used in this experiment was undersized, a sizable number of particles strike the aluminum frame. If these particles shower, it will increase the efficiency of the H×V trigger (since the H×V counters are immediately downstream of P4.) This effect will mean that our measured cross sections are higher than the true cross section.

We estimate that the combined systematic effects cause a 30% systematic error in the cross sections.

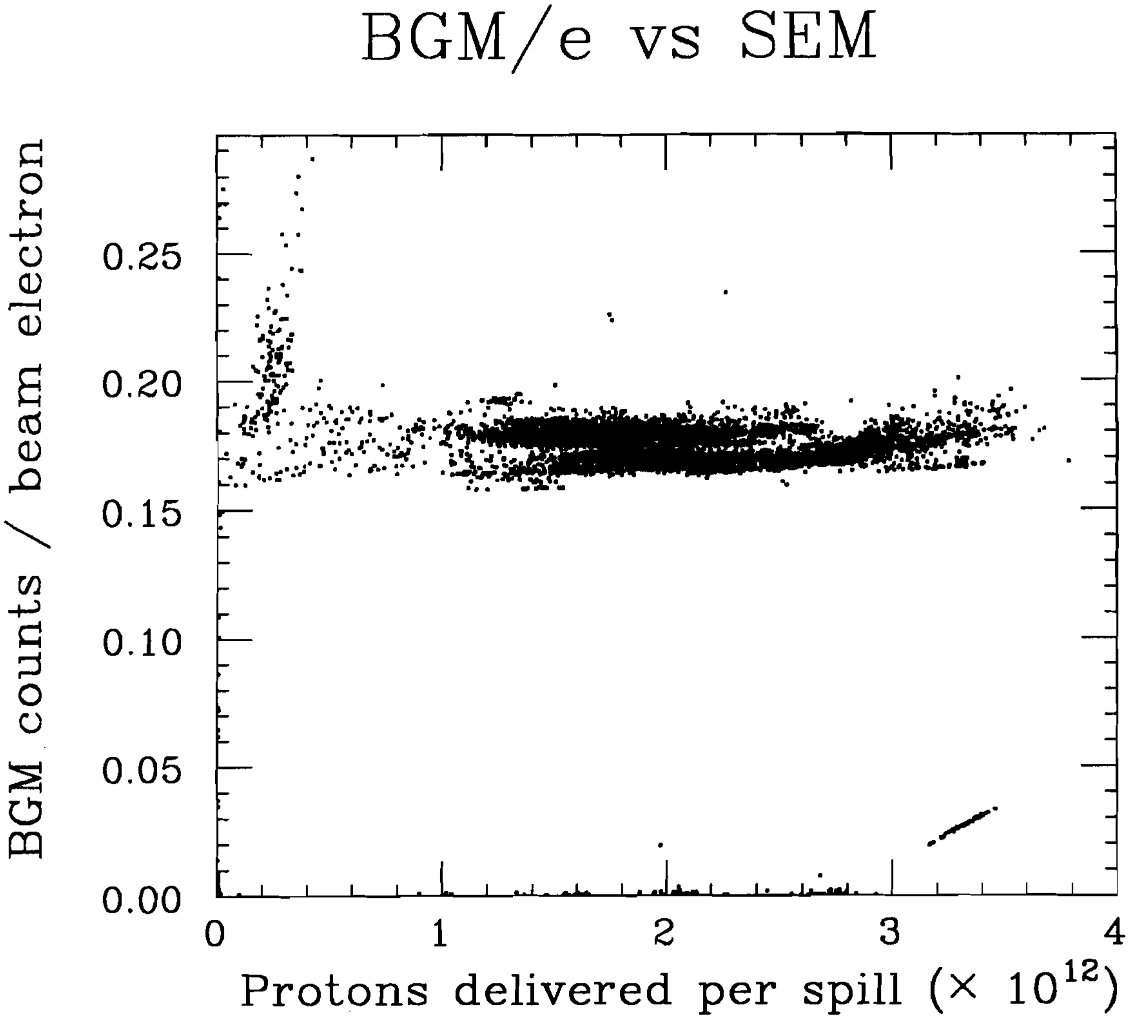

Figure 5.1: The ratio of the BGM scaler to the number of electrons as a function of the number of protons delivered to the wideband beam (SEM). (The number of electrons is counted by the BT scintillator, which suffers from pile-up due to multiply occupied rf buckets. The pile-up can be corrected by a simple model based in the duty factor of the beam.) The BGM/e ratio is constant over the entire range of delivered protons, indicating that the BGM scaler has no problem with pileup.

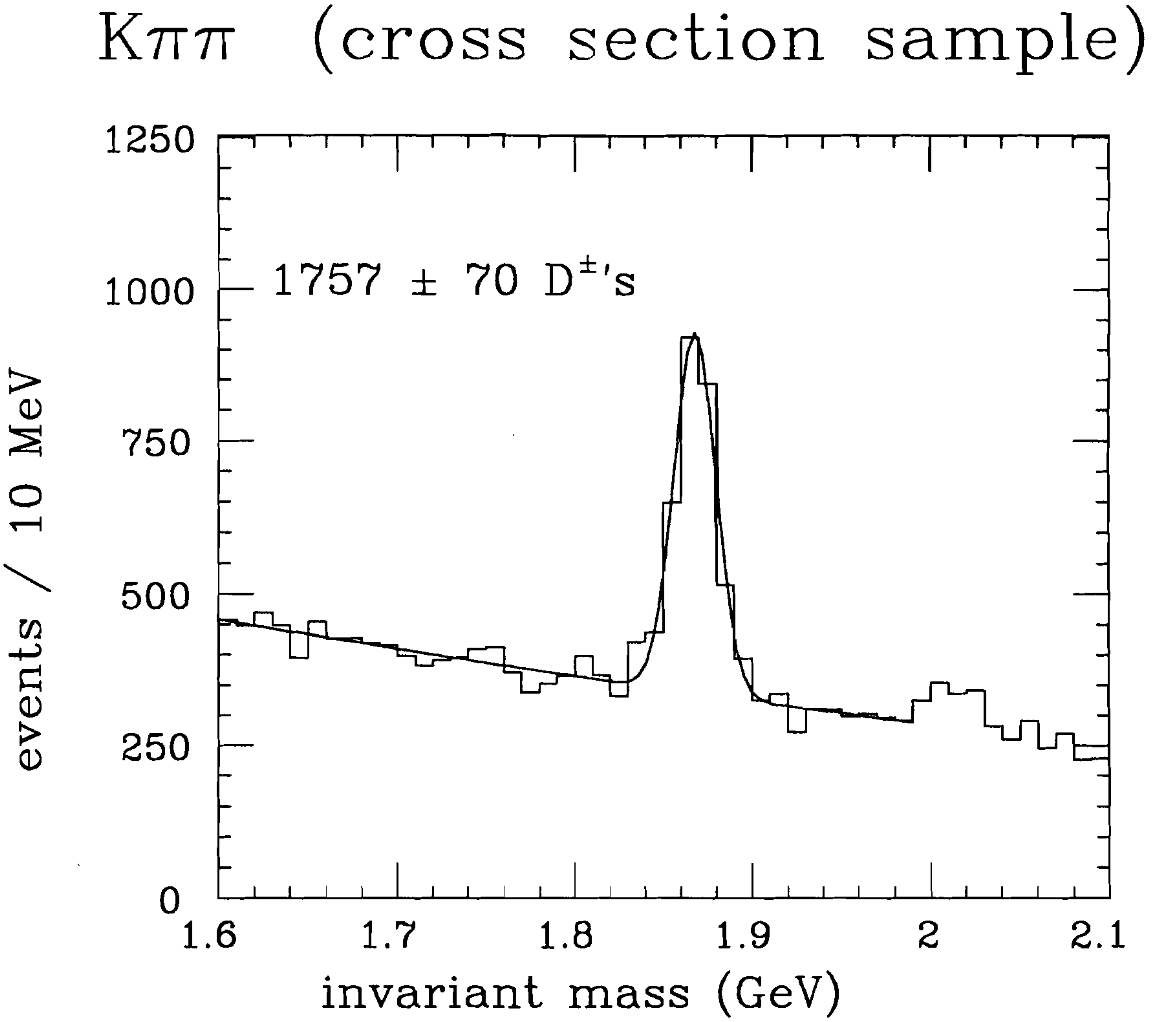

Figure 5.2: The $D^{\pm}$ sample used to measure cross sections.

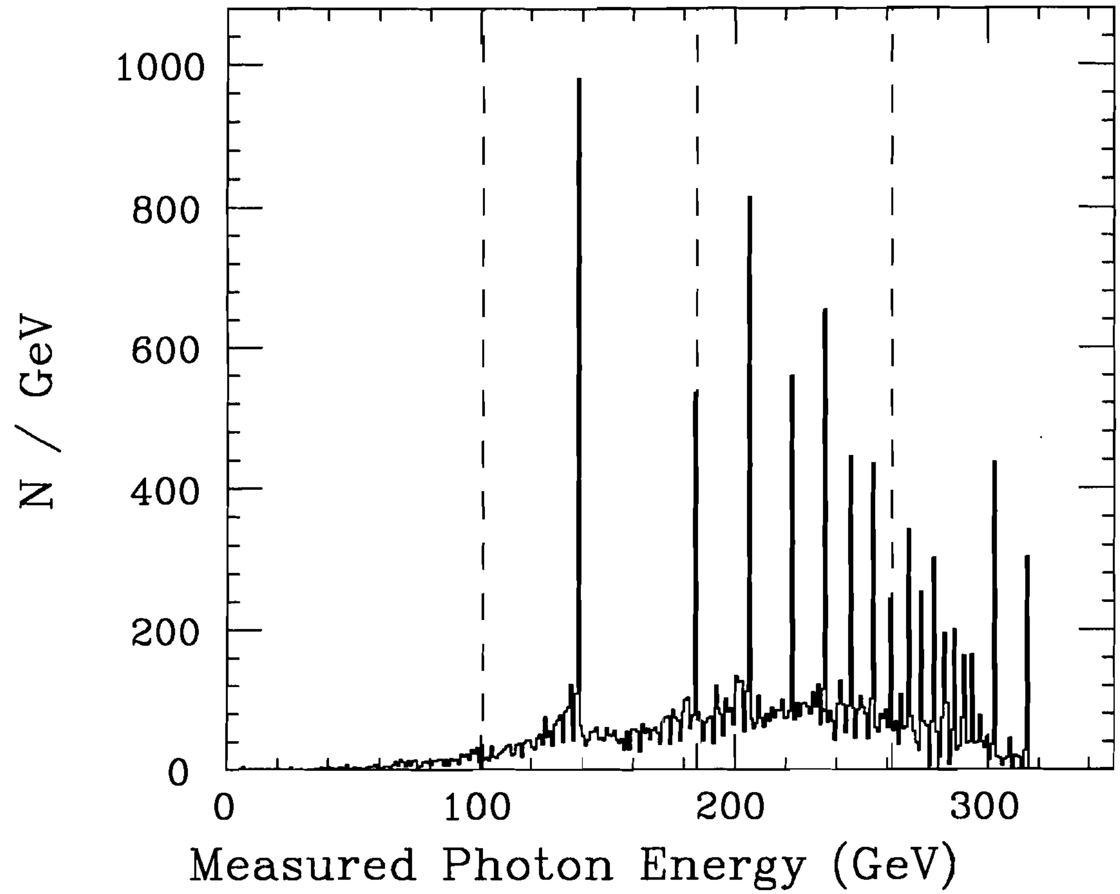

Figure 5.3: The measured photon energy spectrum. The cross section ω bins are delineated by the dashed lines.

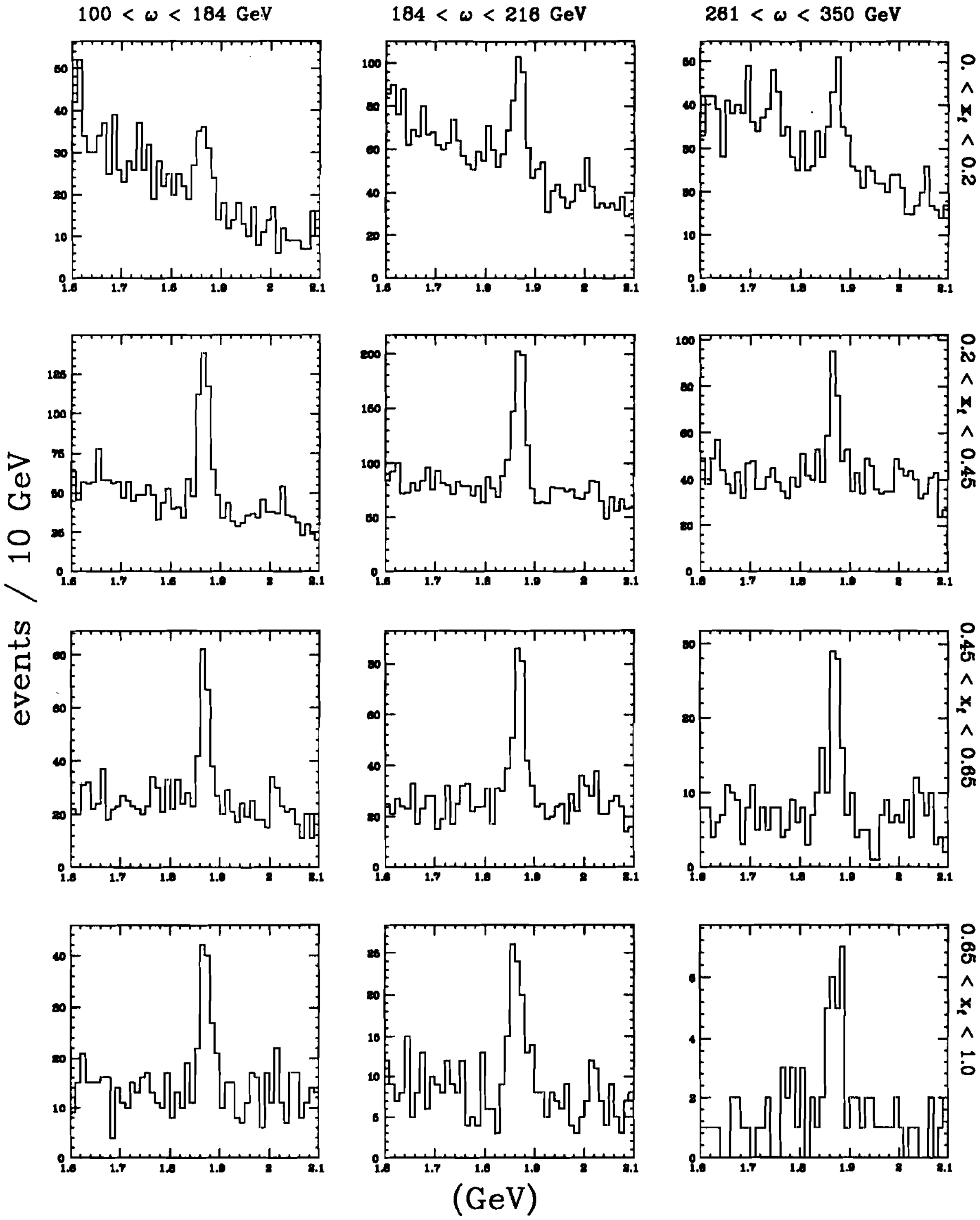

Figure 5.4: The signal binned in α bins. The columns are ω ranges and the rows are x_f ranges.

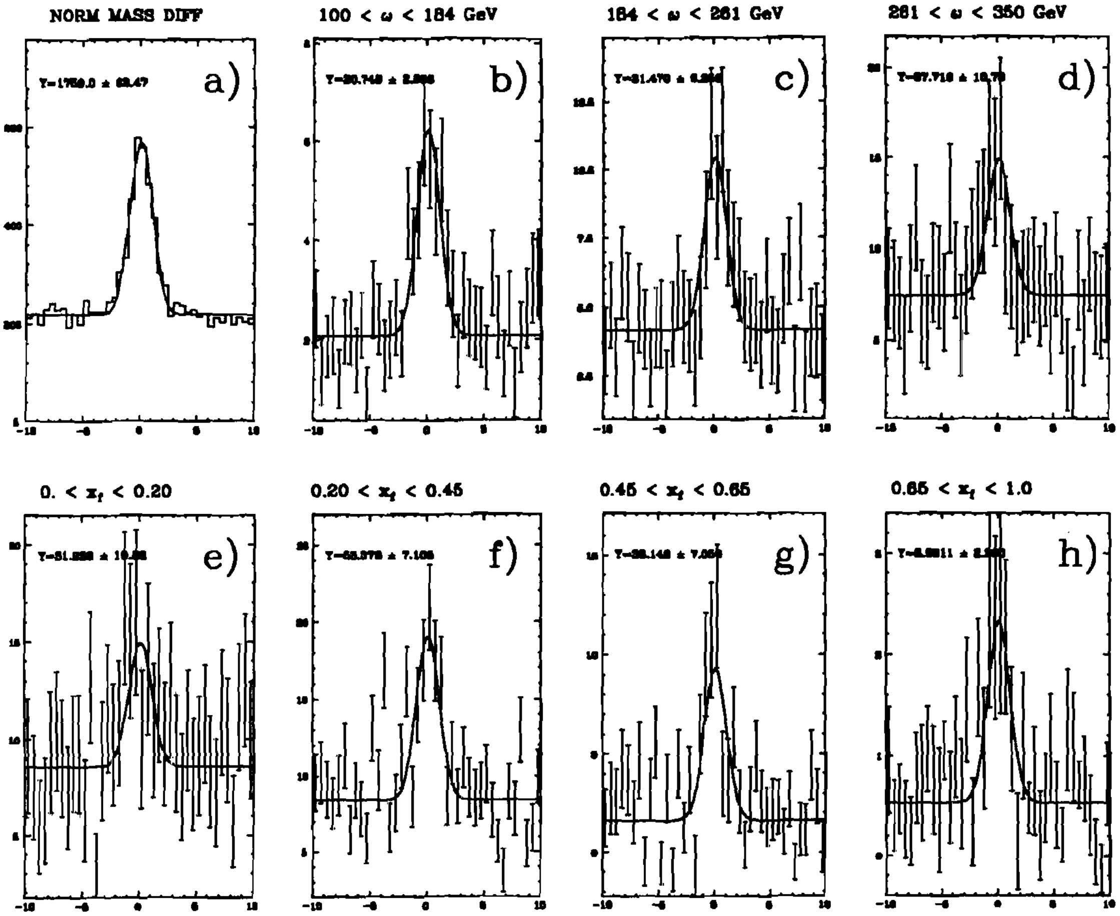

Figure 5.5: a) The normalized mass difference for all events, and the C_α weighted histograms for b)-d) different ω ranges, and for e)-h) different x_f ranges, as described in the text. The cross section signal peaks were fit to a gaussian which was constrained to be width = 1 and centered at the same location as the fit to the normalized mass difference for all the events. The area under the peaks is the average cross section times branching ration (nb/nucleon) for the bin.

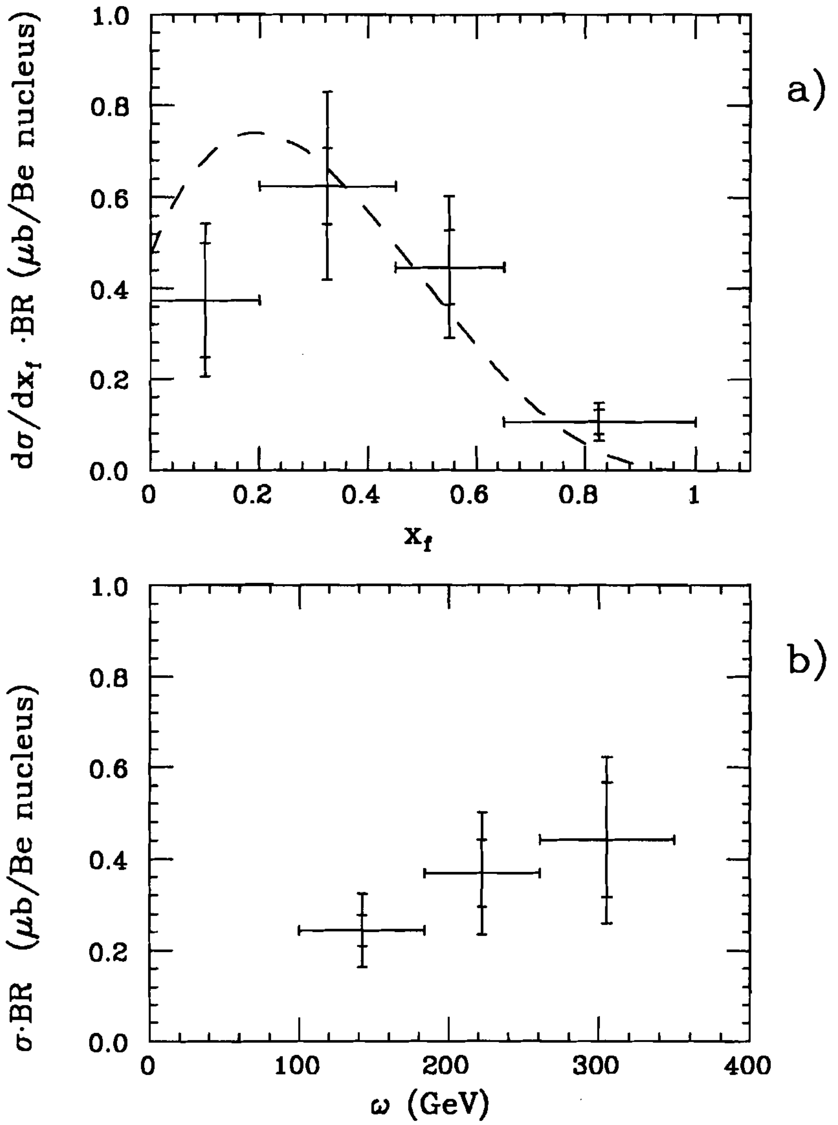

Figure 5.6: The cross section as measured in this analysis: a) $d\sigma/dx_f \cdot BR$ for $100 < \omega < 350$ GeV as a function of x_f. The curve is a parameterization given by E691 [17]. b) σ as a function of photon energy (ω) for $x_f > 0$. The inner errors are statistical only, and the outer error are statistical and systematic added in quadrature.

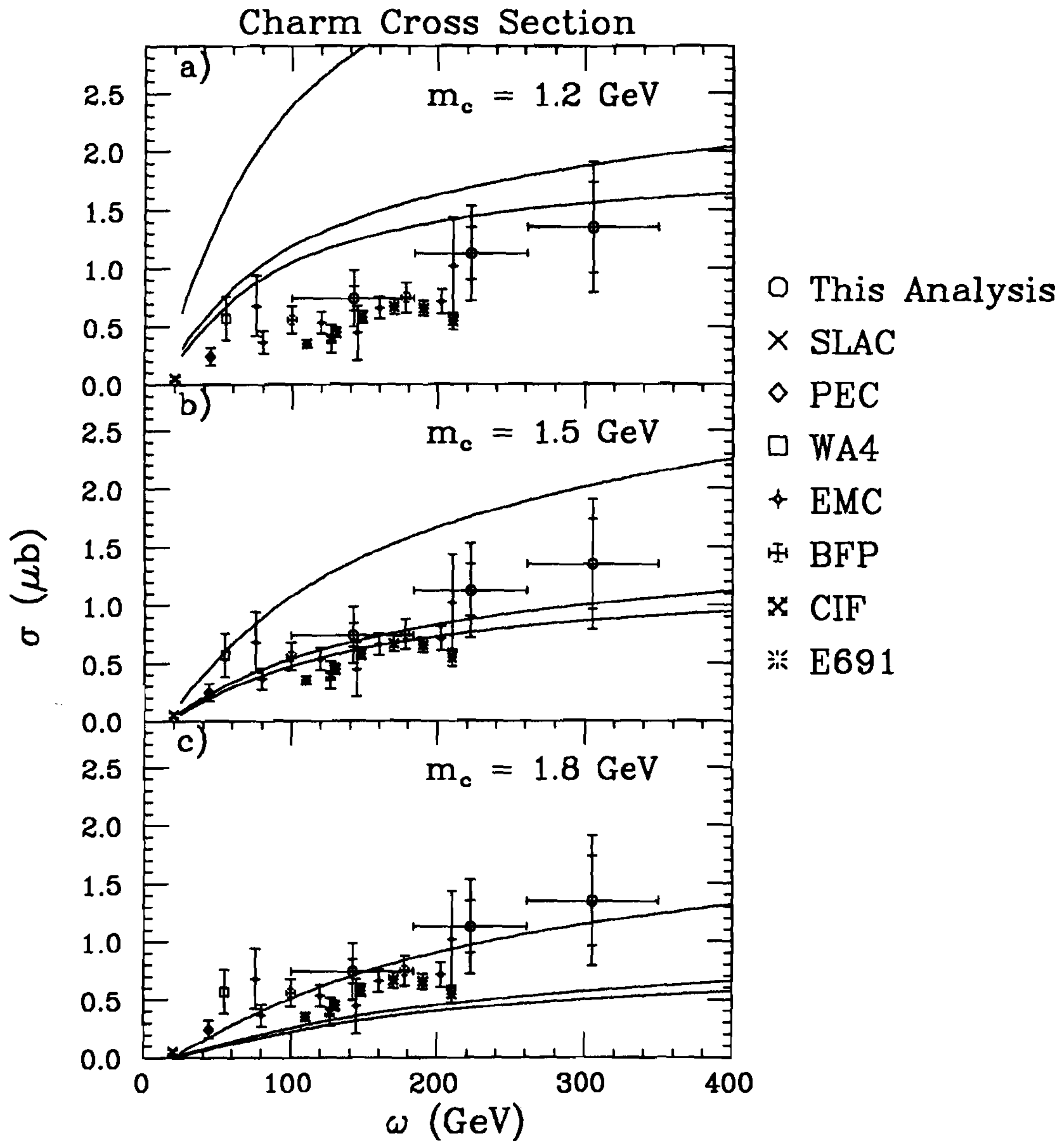

Figure 5.7: Comparison of various charm cross section measurements to photon-gluon fusion calculations of Ellis and Nason [10]. The central line represents the calculation, and the upper and lower curves represent theoretical uncertainty. Calculations for charm quark mass of: a) 1.2 GeV, b) 1.5 GeV, and c) 1.8 GeV. The data points are also from Ellis and Nason, see references therein.

CHAPTER 6

$D^{\pm}$ Lifetime

6.1 Method

In general, a lifetime fit proceeds by fitting the data to an exponential:

$$\frac{dN}{dt} \propto \exp(-t_{\text{meas}}/\tau)$$

where t is the proper time. However, attempting to separate the signal from the background on an event-by event basis is impossible, so some method must be invented to take care of the contamination by the background. In doing so, one can bring in an appreciable amount of systematical error due to Monte Carlo model dependence or a particular chosen parameterization. In addition, in this case, the $D^{\pm}$ sample is obtained through use of a significance of detachment cut, which implies a minimum lifetime (on an event-by-event basis). We wish to find a lifetime measurement method which will include minimal model dependence or parameterization and will be able to deal with the effects of the significance of detachment cuts.

Fermilab Experiment E691 has devised a clever method which addresses the above issues [23]. This lifetime method fits for a *modified proper time*, $t = t_{\text{meas}} - A\sigma_t$, where σ_t is the error on the individual event. That is, we "start the clock" (A) on an event-by-event basis, using the individual errors for that event. The modified proper time distribution will also be exponential. This method allows us to incorporate a significance-of-detachment requirement (which removes zero lifetime background), but lose as few real charm events as possible.

The method we use to find lifetimes is a binned maximum likelihood fit to an exponential, with sideband background subtraction. ("Sidebands" are invariant mass regions at higher or lower mass than the charm particle signal region.) Since this method uses no parameterization for the lifetime of the background, it does not suffer from systematic uncertainty arising from such a parameterization. Since the background will include both zero-lifetime background as well as "charm leftovers", a suitable background parameterization is difficult to construct. In addition there is very little statistical power in parameterizing the background, and the systematic effects are difficult to understand.

6.2 Lifetime Resolution

The measured proper time and the error in the proper time are calculated from the decay length of the $D^{\pm}$ and its error:

$$t_{\text{meas}} = \frac{L}{c}\,\frac{m_D}{P_D}$$

$$\sigma_t = \frac{\sigma_L}{c}\,\frac{m_D}{P_D} \tag{6.1}$$

where m_D and P_D are the mass and momentum of the $D^{\pm}$. Our resolutions are studied using a sample of D^o's which come from D^*'s [24]. Cutting on the mass difference between the D^o and D^* gives a D^o sample which is selected only kinematically, with no lifetime requirements at all. Plotting the fraction of D^o's which survive a L/σ_L cut, and using the world average lifetime, σ_t is found to be about 0.048 ps. We can confirm this number with Monte Carlo by measuring the difference between the measured lifetime and the generated lifetime. From Monte Carlo, σ_t is about 0.045 ps. (See Figure 6.1.)

6.3 Binned Maximum Likelihood

In each lifetime bin, centered at t_i, there will be S_i signal events and B_i background events, for a total of $N_i = S_i + B_i$ events. The total number of signal events is $S_{tot} = \sum_i S_i$. The likelihood function (assuming Poisson statistics) is:

$$\mathcal{L} = \prod_i \frac{\mu_i^{N_i}}{N_i!}\, e^{-\mu_i} \tag{6.2}$$

where

$$\mu_i = \epsilon(t_i)\; S_{tot}\frac{e^{-t_i/\tau}}{\tau} + B_i \tag{6.3}$$

The function $\epsilon(t)$ is a *modulator function* which describes how the measured events are expected to deviate from a true exponential. Minimizing $(-\ln\mathcal{L})$ with respect to τ

produces a lifetime. We can repeat this calculation for different values of A, the "clock-starting" point.

6.4 The $\epsilon(t)$ Function

The $\epsilon(t)$ function takes into account two factors. First, the reconstruction efficiency may have a dependence on decay distance, and thus proper time. Second, resolution effects will move events from their true lifetime bins into adjacent bins.

Some examples of the effects included in the $\epsilon(t)$ function:

1. Events with very long lifetimes will verticize inside the microstrips. The daughters from this decay will be less likely to be reconstructed.
2. Daughter particles which traverse a longer distance of the target are more likely to be absorbed, lowering the efficiency for shorter-lived events.
3. The angular acceptance of the SSDs may discriminate against events which "open up" far upstream of the SSD.
4. For very short-lived events, resolution effects may cause the the measured lifetime to fluctuate negative. Since there are no "negative lifetime" events to fluctuate high and compensate, there will be a depletion of events at very short lifetimes.

The effects listed above, as well as other efficiency effects, are difficult to calculate, so we determine $\epsilon(t)$ from Monte Carlo. We measure the deviance of the measured distribution from the assumption that the reconstructed events are distributed according to an exponential. For each lifetime bin:

$$\epsilon_i = \frac{N_i^{mc}}{N_{tot}^{mc} \dfrac{e^{-t_i/\tau}}{\tau} \Delta t} \tag{6.4}$$

where N_i^{mc} is the number of Monte Carlo events reconstructed in bin i, N_{tot}^{mc} is the total number of reconstructed Monte Carlo events, τ is the Monte Carlo lifetime, and Δt is the bin width.

6.5 Additional Sources of Uncertainty

In addition to the uncertainty of the lifetime due to the fit, there are two additional sources of lifetime uncertainty: that due to fluctuations in the sidebands, and that due to fluctuations in the Monte Carlo.

The variance of the fit parameter, α, measured by maximum likelihood is given by:

$$\frac{1}{\sigma_\alpha^2} = \int dt \, \frac{(\partial F/\partial\alpha)^2}{\sigma^2(F - F_{pred})} \tag{6.5}$$

where F is the data which are being fit to, and F_{pred} is the theoretical function being fit for. In the usual case, there is no error in F_{pred}, since the fit function is known, so the total variance of $F - F_{pred}$ is just the variance of F. In our case, however, we do have an uncertainty in F_{pred}, due to statistical fluctuations in the sideband background, and due to fluctuations in the Monte Carlo, which determines ϵ.

6.5.1 *Uncertainty Contributed by Sideband Subtraction*

The sideband subtraction method assumes that the time evolution of the background under the signal peak is well-described by the sideband background. Clearly, the error on the background estimation will decrease as the sideband width is increased. However, as the sidebands grow farther from the signal region, the more unreliable their description of the lifetime distribution of the signal-region background. Some compromise between the two effects must be made.

The anticipated variance of the measured lifetime will be given by:

$$\frac{1}{\sigma_\tau^2} = \int dt \, \frac{(\partial S/\partial\tau)}{\sigma^2(N_i - N_{pred})} \tag{6.6}$$

where our fitting function is $N_i^{pred}(t) = S_i^{pred} + B_i^{pred}$, where S_i^{pred} is the predicted signal, $S_i^{pred} = \epsilon(t) S_{tot} \exp(-t/\tau)/\tau$ and B_i^{pred} is the predicted background, $B_i^{pred} = RB_i^{sb}$ where B_i^{sb} is the number of events in the sidebands and R is the ratio of the width of the signal region to the combined width of the sideband regions. The data we are fitting is given by $N_i = S_i + B_i$. In the case where N_i^{pred} is totally determined, that is, ignoring fluctuations in ϵ and B_{sb}, the denominator for equation 6.6 becomes $\sigma^2(N_i - N_i^{pred}) = \sigma^2(N_i) = N_i$. If however, we include the effects of the variance of the sideband background, the denominator in equation 6.6 becomes:

$$\begin{aligned}\sigma^2(N_i - N_i^{pred}) &= \sigma^2(N_i) + \sigma^2(N_i^{pred}) && (6.7a)\\ &= \sigma^2(N_i) + \sigma^2(S_i^{pred}) + \sigma^2(B_i^{pred}) && (6.7b)\\ &= \sigma^2(N_i) + \sigma^2(S_i^{pred}) + R^2\ \sigma^2(B_i^{sb}) && (6.7c)\\ &= \sigma^2(N_i) + R^2\ \sigma^2(B_i^{sb}) && (6.7d)\end{aligned}$$

where we have ignored uncertainty in the ϵ function in step 6.7d, so that the variance of the predicted signal is zero. The variance of a yield is, of course, just the yield itself. We then scale the errors reported by the maximum likelihood fitter by the ratio of the original anticipated error to the new (sideband-corrected) anticipated error:

$$\sigma_\tau^{new} = \sigma_\tau^{fit} \sqrt{\frac{\displaystyle\int dt \frac{(\partial S/\partial\tau)^2}{N_i}}{\displaystyle\int dt \frac{(\partial S/\partial\tau)^2}{N_i + R^2 B_i^{sb}}}} \qquad (6.8)$$

6.5.2 Uncertainty Contributed by Monte Carlo

In addition, the lifetime uncertainty will include effects due to fluctuations in the Monte Carlo lifetime distributions. These fluctuations will cause uncertainties in the $\epsilon(t)$ function, and therefore the fitting function. It is obviously better to have as much Monte Carlo as possible, and certainly the Monte Carlo sample should be much larger than the data sample.

If we work in the limit of negligible background

$$\sigma^2(N_i - N_i^{pred}) = \sigma^2(S_i - S_i^{pred}) = \sigma^2(S_i) + \sigma^2(S_i^{pred}) \qquad (6.9a)$$

The variance of (S_i^{pred}) ultimately comes from Monte Carlo counting statistics. Since $S_i^{pred} \propto \epsilon$ (equation 6.3), and $\epsilon \propto N_i^{mc}$ (equation 6.4), then $\sigma^2(S_i^{pred})/S_i^{pred} = 1/N_i^{mc}$

and

$$\sigma^2(N_i - N_i^{pred}) = S_i + \frac{(S_i^{pred})^2}{N_i^{(mc)}} \tag{6.9b}$$

Here we make some approximations to simplify the calculation of the new error. Since the χ^2 has been minimized, $S_i \approx S_i^{pred}$. Also, if the Monte Carlo lifetime is identical to the data, the measured Monte Carlo events will fall into lifetime bins in the same proportion as the data, so that $S_i/N_i^{(mc)}$ will just be $S_{tot}/N_{tot}^{(mc)}$. Thus

$$\sigma^2(S_i - S_i^{pred}) \approx S_i \left(1 + \frac{S_{tot}}{N_{tot}^{(mc)}}\right) \tag{6.9c}$$

The constant term $(1 + S_{tot}/N_{tot}^{(mc)})$ can be pulled out of the integral of equation 6.6, which means that the new error is given by:

$$\sigma_\tau^{new} = \sigma_\tau^{old}\sqrt{1 + \frac{N_{tot}}{N_{tot}^{(mc)}}} \tag{6.10}$$

6.6 Lifetime Results

The $D^\pm$ sample selected for the lifetime analysis includes all of the analysis requirements previously explained, as well as a cut which removes events with either primary or secondary vertexes in the TR1 trigger counter. This cut removes background with secondary interactions, which may distort the lifetime measurement. Only events with lifetimes less than $6\tau_{D^\pm}$ are used. The sample includes about 2600 $D^\pm$'s and is shown in Figure 6.2.

The requirements of the skim and the analysis are relatively bias-free, except for the significance-of-detachment cut of $L/\sigma_L > 3$. Since a significance of detachment cut is implicit in our lifetime method (in fact it is just A), the skim requirement merely forces a lower bound on our choice of A.

The signal region is chosen to be ±25 MeV of the accepted value of the $D^{\pm}$ mass, and the sideband background regions are chosen to be 50 MeV wide and separated from the signal region by 40 MeV. The R factor, therefore, is 1/2. Typical scale factors due to sideband fluctuations are about 1.04 to 1.06. The signal and sideband regions are illustrated in Figure 6.2. The number of t bins in the binned maximum likelihood fit is chosen to be 25, although the results do not change appreciably when 100 bins are used.

The Monte Carlo sample, which requires the same analysis cuts as the data, consists of about 23,000 events, about 9 times larger than the data sample. The generated $\tau_{D^{\pm}}$ of the Monte Carlo events is 1.067 ps. Figure 6.3 shows $\epsilon(t)$ functions for $A = 3$ and $A = 5$. This function deviates significantly from 1 at large lifetimes because of the inefficiency of reconstruction for events which decay inside the microstrips. However, the $\epsilon(t)$ function shows very small corrections at short lifetimes. The σ_{τ} scale factor due to Monte Carlo fluctuations (equation 6.10) is about 1.05.

Figure 6.4 shows sample lifetime fits for $A = 3$ and $A = 5$. The points plotted are the background-subtracted number of events in the bin divided by the $\epsilon(t)$ function; the error bars are simply the square root of that number. The line shows the result of the fit. Figure 6.5 shows the measured lifetime using different values of A.

To quote a lifetime, we want to use an A region where the signal-to-background is relatively good. At A values greater than about 7.5, the signal-to-background is greater than 3 to 1. We also want to minimize our dependance on the modulator function, ϵ, measured from the Monte Carlo. At an A cut of about 14, 10% of the data will come from lifetime regions which are appreciably influenced by ϵ. Thus, we average the lifetime values at $A = 8$ to $A = 14$. Systematic error is estimated to be 0.020 ps by looking at the magnitude of Monte Carlo corrections and the fluctuations of the measured lifetime for different values of A. Thus, the $D^{\pm}$ lifetime measured in this analysis is:

$$\tau_{D^{\pm}} = 1.061 \pm 0.039 \pm 0.020 \text{ ps}$$

Figure 6.6 shows this result in comparison with other recent lifetime measurements. A remarkably consistent picture emerges.

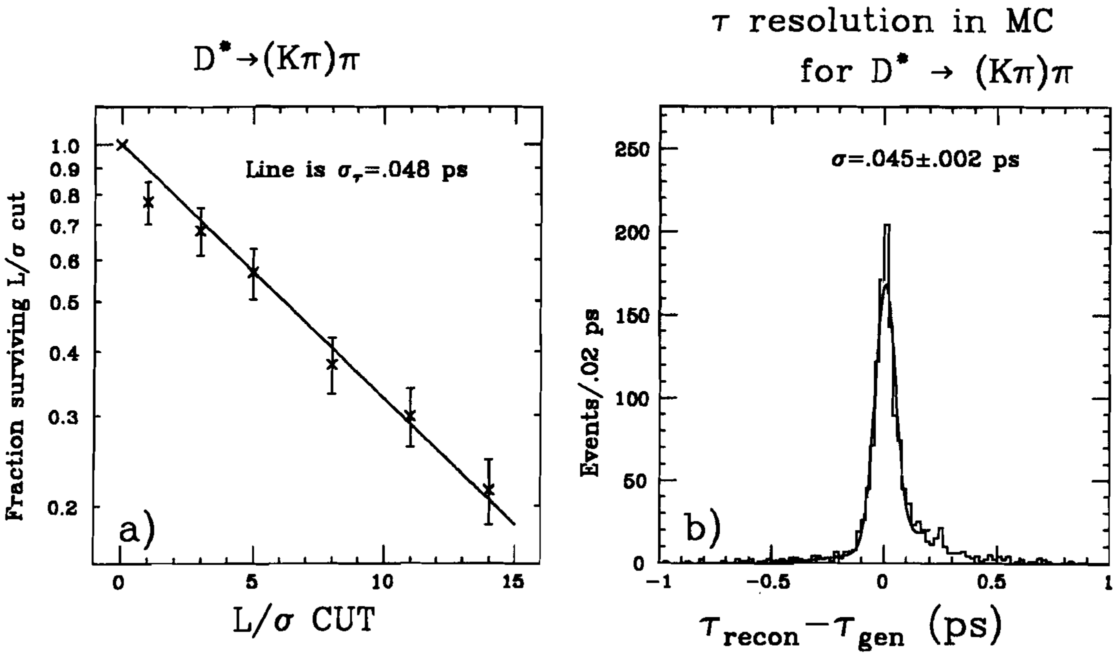

Figure 6.1: a) The fraction of D^o's passing a certain L/σ_Lcut. By using the lifetime of the D^o and a resolution of $\sigma_\tau = 0.048$ ps, one gets the plotted line. The line matches the data very well. b) Distribution of differences between the reconstructed and generated lifetime of Monte Carlo events. The width of this distribution is 0.045 ps.

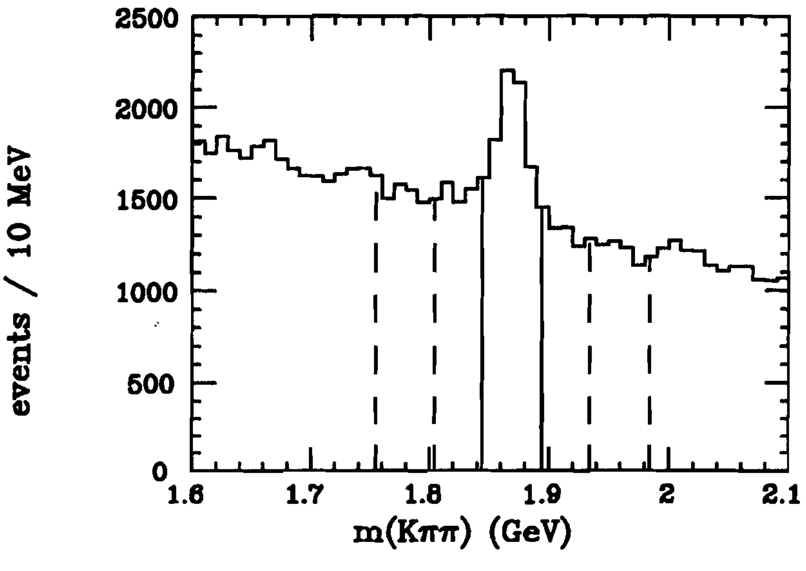

Figure 6.2: $D^{\pm}$ signal used for lifetime fits. The signal and background regions are indicated.

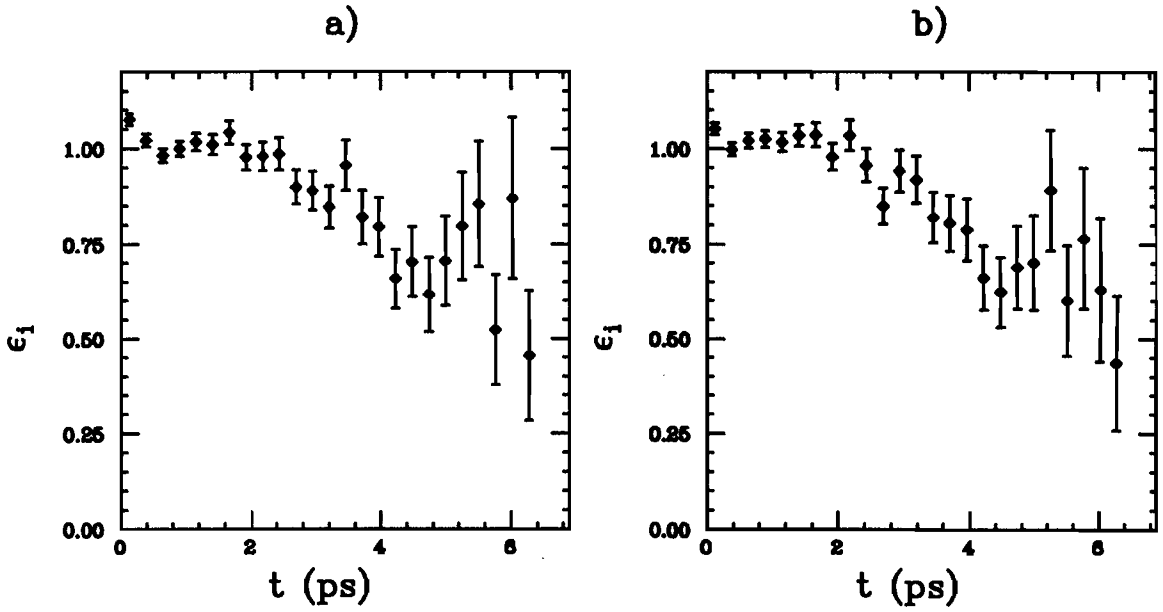

Figure 6.3: Modulator functions $\epsilon(t)$ for a) $A = 3$ and b) $A = 5$, computed from Monte Carlo.

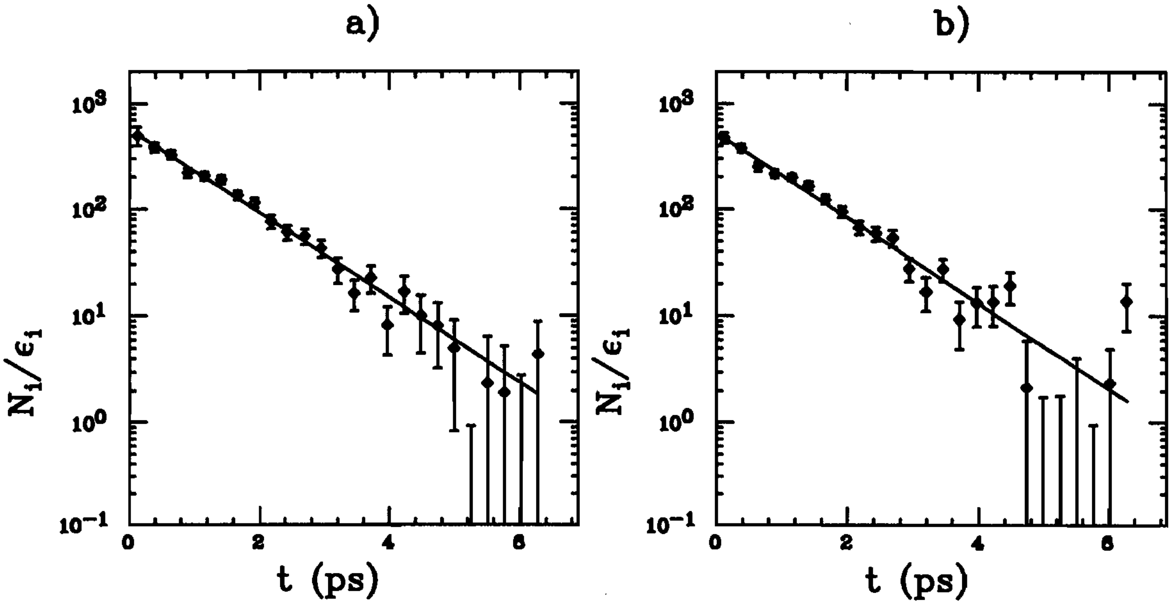

Figure 6.4: Lifetime fits for a) $A = 3$ and b) $A = 5$. The points are the efficiency-corrected, background-subtracted number of events in the lifetime bin, and the line is the fit to an exponential.

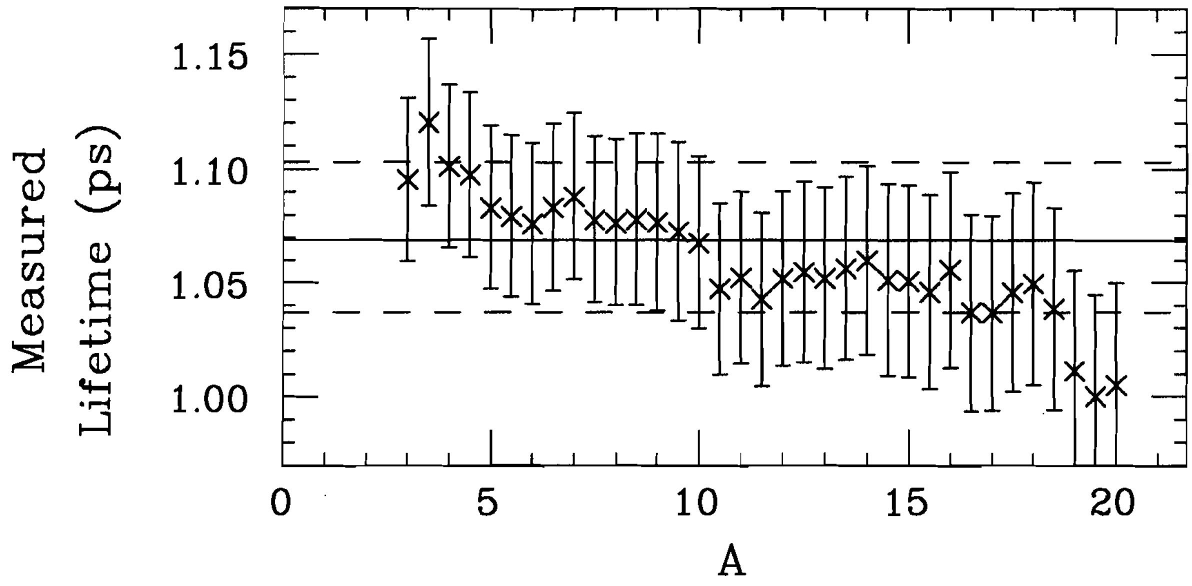

Figure 6.5: Lifetime measurements for various values of A. The solid line indicates the world average value, and the dashed lines indicate the uncertainty of the world average.

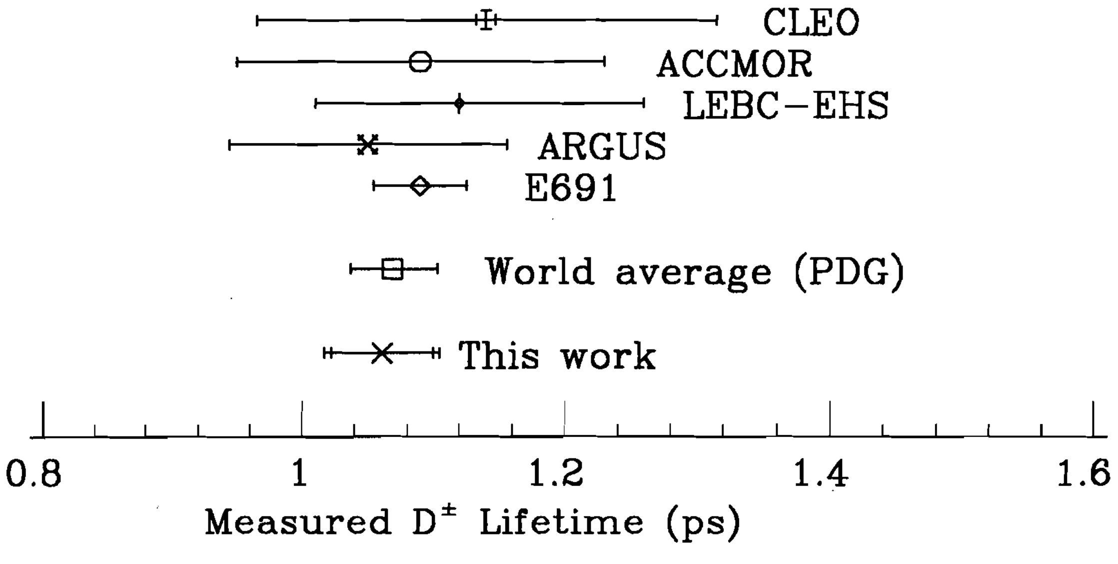

Figure 6.6: Recent lifetime measurements by various groups. [25,26,27,28,29,30]

CHAPTER 7
Additional $D^{\pm}$ Studies

7.1 Charge Asymmetry

Associated production models will predict an excess of D^- (anti-charm) mesons. Studies were done to find the ratio of D^+ to D^-. For several values of L/σ_L, the signal was split into positive and negative histograms. These signals were fit to a gaussian with a fixed width equal to the width of the fit to the total signal. The signals and fits are shown in Figure 7.1. In each case there appears to be a slight excess of D^+ mesons, although the yields of the positive and negative D's are consistent within errors. The Monte Carlo exhibits no charge asymmetry. The charge ratio for data and Monte Carlo is summarized in Table 7.1.

Table 7.1: Charge Asymmetry for data and Monte Carlo

$L/\sigma_L >$	D^+/D^- (data)	D^+/D^- (MC)
5	1.042 ± 0.062	1.001 ± 0.014
8	1.073 ± 0.062	0.998 ± 0.015
11	1.057 ± 0.062	1.006 ± 0.016
15	1.066 ± 0.068	1.019 ± 0.018

The D^+/D^- ratio result is obtained by averaging the values for the different L/σ_L cuts and using a typical error bar. The result is:

$$\frac{\text{number of } D^+}{\text{number of } D^-} = 1.060 \pm 0.063$$

The anti-charm excess predicted by associated production models will be particularly noticeable near threshold. Thus, we look at the charge asymmetry for different momentum ranges. Here, we use the *normalized mass difference*, $(m_D - m_{meas})/\sigma_m$, since the width of the signal may be a function of momentum. If we use the normalized mass difference, we can constrain the fit to be of width = 1. The results are found in Figure 7.2. Again, although there may be a slight excess of D^+ mesons, the excess is not statistically significant. There is no noticeable dependance on the momentum. We see no evidence of an excess of D^- which is predicted by associated production models.

7.2 Transverse Momentum Distribution

We have also studied the $D^\pm$ distribution as a function of transverse momentum squared, $P_\perp^2$. From Monte Carlo we determine that the acceptance is flat in $P_\perp^2$ out to about 8 or 10 GeV^2, where we run out of statistics. (See Figure 7.3.) To plot the $P_\perp^2$ distribution, we make sideband-subtracted weighted histograms. Two mass sidebands, from 1.74 to 1.78 GeV and 1.96 to 2.00 GeV are chosen. Each sideband is the same width as the signal region which extends from 1.85 to 1.89 GeV. Therefore, events whose mass falls in the sideband region are added to the histogram with a weight of -0.5. Events in the signal region are incremented with a weight of 1.0. Histograms are made for various significance of detachment requirements. The harder the cut on the significance of detachment, the less the background, and the less we rely on the validity of the sideband subtraction. Of course, there will be fewer events as we cut harder. The $P_\perp$ distributions are shown in Figure 7.4. The distributions are fit to exponentials of polynomials in $P_\perp^2$:

$$dN/d(P_\perp^2) = A\exp(a_1 P_\perp^2 + a_2 P_\perp^4)$$

The fits for the various L/σ cuts are very consistent. Taking the average of the a_1 and a_2 values for the different L/σ_L cuts gives:

$$a_1 = -0.925 \pm 0.050/ \text{ GeV}^2$$

$$a_2 = 0.0368 \pm 0.0071/ \text{ GeV}^4$$

7.3 Dynamic Substructure in the $D^{\pm} \rightarrow K^{\mp}\pi^{\pm}\pi^{\pm}$ decay

The $D^{\pm}$ sample for the purpose of making Dalitz plots must be fairly clean. The sample used is the usual sample with a harder significance of detachment cut: $L/\sigma_L > 15$. We then use only events in in the $D^{\pm}$ mass region: 1.83 GeV $< m_D <$ 1.90 GeV. Since there are two identical pions in the final state, it is appropriate to select a specific one of the $K^{\mp}\pi^{\pm}$ masses to plot against the mass of the $\pi^{\pm}\pi^{\pm}$. (Technically known as "folding" the Dalitz plot.) Conventionally, one selects the lower of the two $K^{\mp}\pi^{\pm}$ masses. In the absence of interesting effects, we expect the events to spread uniformly throughout the allowed region of the Dalitz plot. Figure 7.5a shows the Dalitz plot for Monte Carlo events, where the $D^{\pm} \rightarrow K^{\mp}\pi^{\pm}\pi^{\pm}$ decay is governed solely by three-body phase-space.

It has been claimed [13,25] that about 20% of the $D^{\pm} \rightarrow K^{\mp}\pi^{\pm}\pi^{\pm}$ proceed via $D^{\pm} \rightarrow K^*(892)\pi^{\pm}$. The Dalitz plot for a Monte Carlo with this fraction of K^* events is shown in Figure 7.5b. A clear, narrow K^* band can be seen in this Monte Carlo Dalitz plot.

The Dalitz plot for the data sample is shown in Figure 7.6. Clearly the distribution of events in the Dalitz plot is not uniform, although no clear resonance bands can be seen. The data resemble neither of the Monte Carlo Dalitz plots. The Dalitz plot and its projections are shown in Figure 7.7, along with MarkIII data [13,31]. The distributions are very similar.

Figure 7.8 shows the $(K^{\mp}\pi^{\pm})_{low}$ mass for the $D^{\pm}$ sample described above, and for the K^*-added Monte Carlo. The Monte Carlo K^* signal is evident, but no corresponding signal can be seen in the data. We then try to enhance the possible K^* signal by taking into account conservation of angular momentum. Since the $D^{\pm}$ is a pseudo-scalar, which decays into a vector (K^*) and a pseudo-scalar ($\pi^{\pm}$), we expect the angle between the the two pions, as viewed in the K^* center of mass, to be distributed according to $\cos^2\theta$. Cutting on $|\cos^2\theta|$ we get the $K^{\mp}\pi^{\pm}$ mass plots shown in Figure 7.9.

Diakonou and Diakonos [14] have postulated that most of the $D^{\pm} \rightarrow K^{\mp}\pi^{\pm}\pi^{\pm}$ signal is due to $D^{\pm} \rightarrow K^*(892)\pi^{\pm}$ and $D^{\pm} \rightarrow K_o^*(1430)\pi^{\pm}$, which interfere so significantly, that the relative amounts of $K^*(892)$ and $K_o^*(1430)$ must be derived from complicated Monte Carlos which take into account the effects of interference.

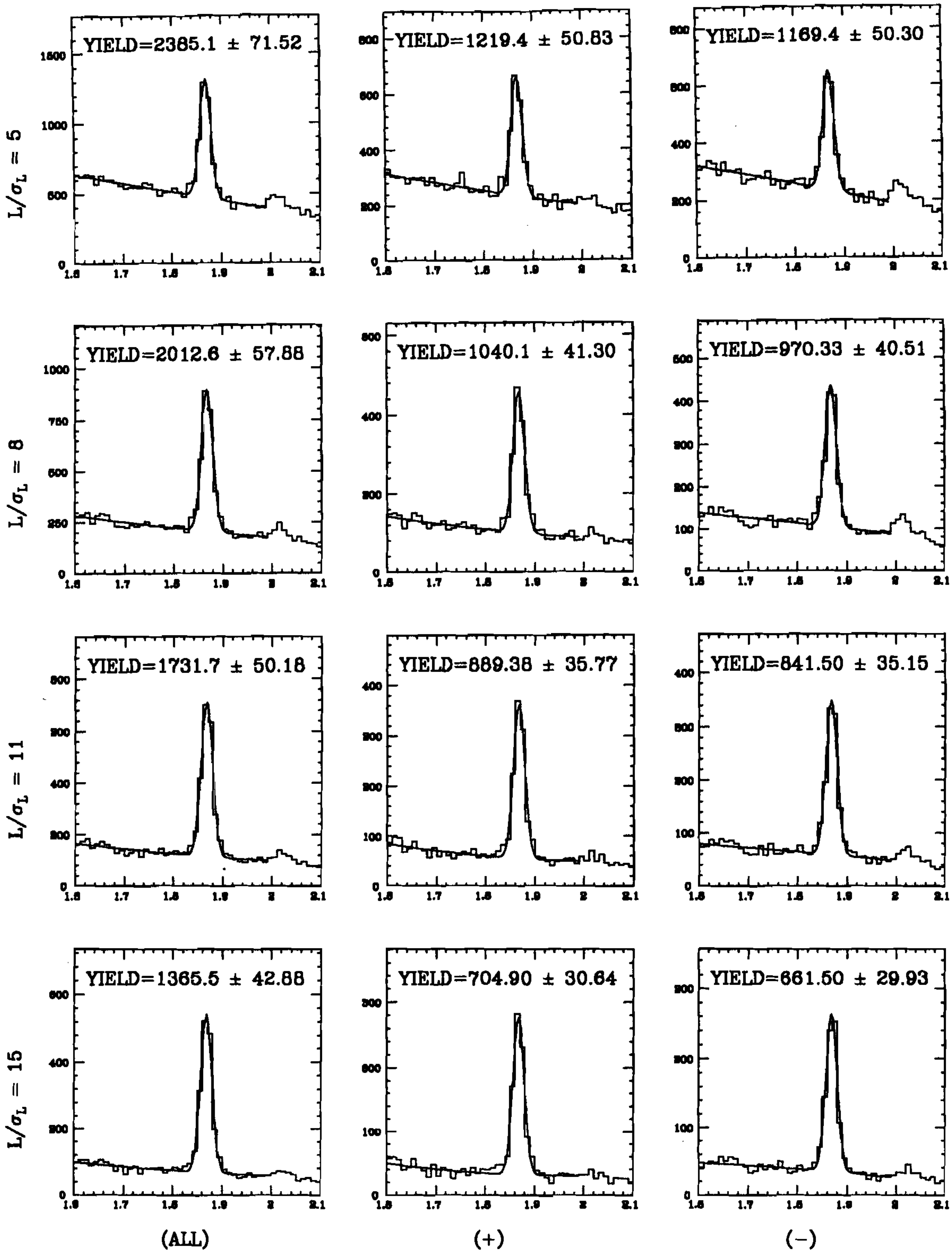

Figure 7.1: The $D^{\pm}$ signal, and charge separated signals for various values of L/σ_L.

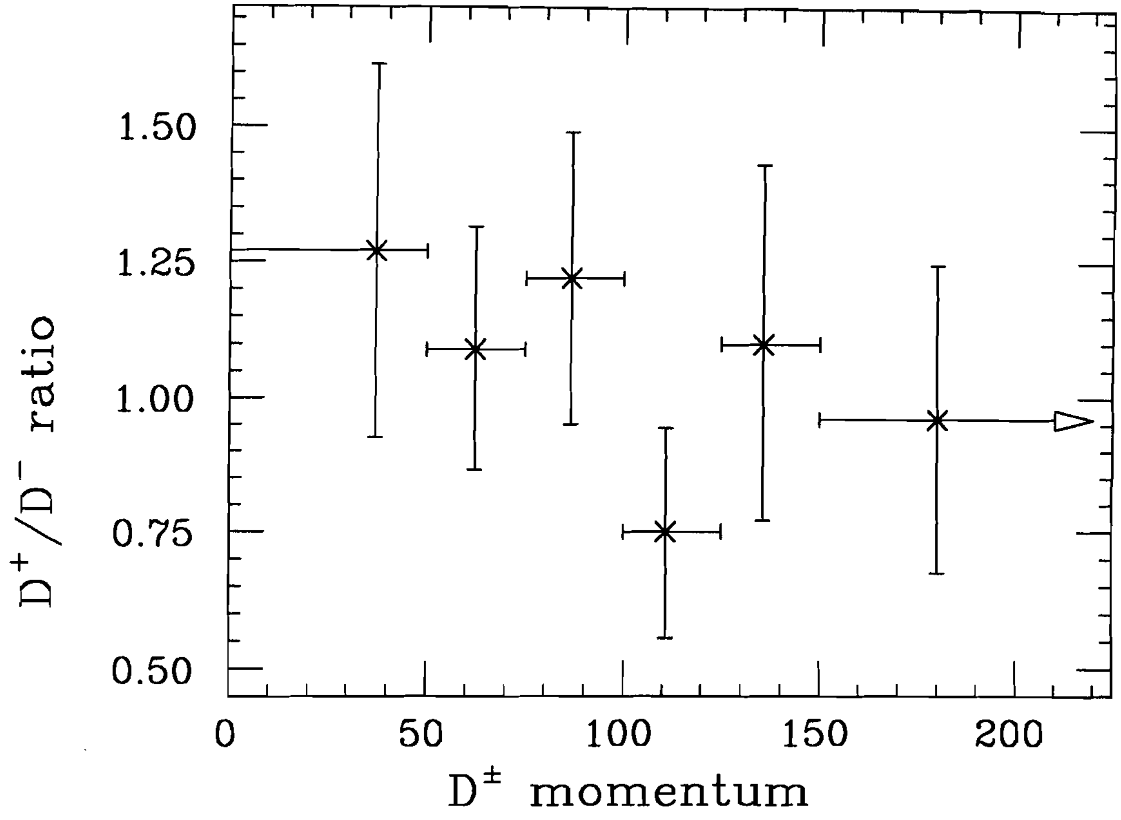

Figure 7.2: The ratio of D^+ to D^- for different momentum ranges.

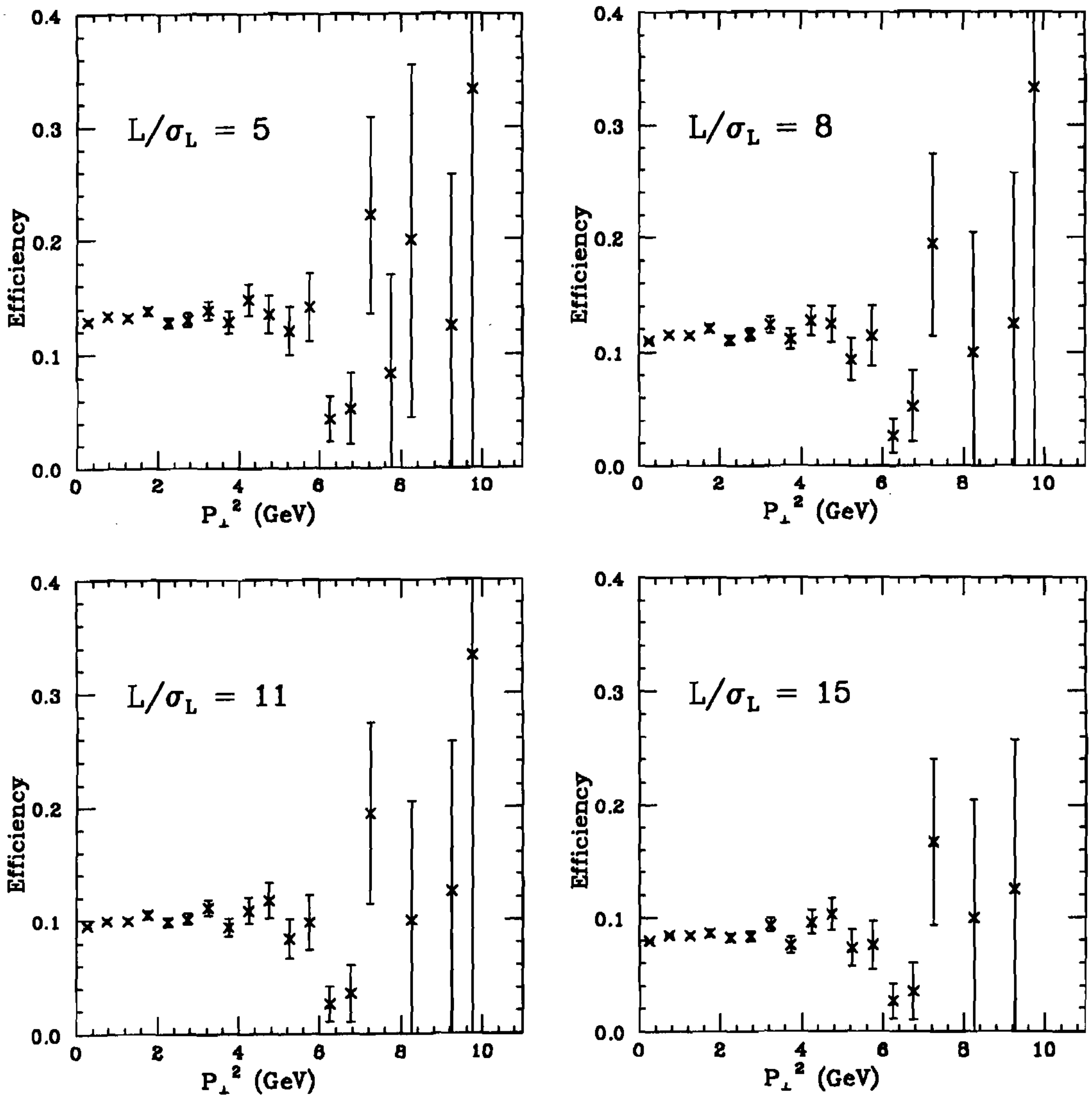

Figure 7.3: Monte Carlo $D^{\pm}$ acceptance efficiency as a function of $P_{\perp}^{2}$ for various significance of detachment (L/σ_L) cuts.

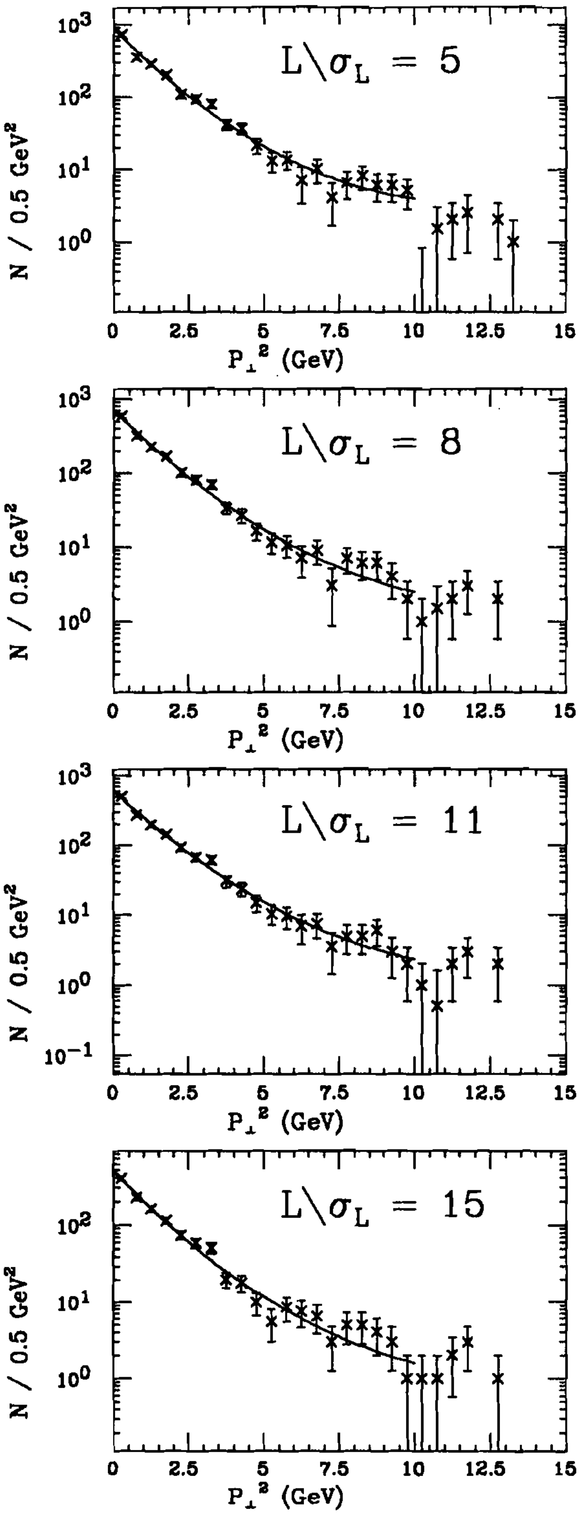

$\text{fit} = A * \exp(a_1 p_\perp^2 + a_2 p_\perp^4)$
$A = 856.6 \pm 53.6$
$a_1 = -0.953 \pm 0.0483$
$a_2 = 0.0414 \pm 0.00639$

$\text{fit} = A * \exp(a_1 p_\perp^2 + a_2 p_\perp^4)$
$A = 696.9 \pm 41.2$
$a_1 = -0.921 \pm 0.0491$
$a_2 = 0.0357 \pm 0.00693$

$\text{fit} = A * \exp(a_1 p_\perp^2 + a_2 p_\perp^4)$
$A = 600.6 \pm 34.7$
$a_1 = -0.912 \pm 0.0493$
$a_2 = 0.0359 \pm 0.00696$

$\text{fit} = A * \exp(a_1 p_\perp^2 + a_2 p_\perp^4)$
$A = 481.8 \pm 29.4$
$a_1 = -0.914 \pm 0.0538$
$a_2 = 0.0342 \pm 0.00808$

Figure 7.4: $P_\perp$ distributions for various significance of detachment (L/σ_L) cuts.

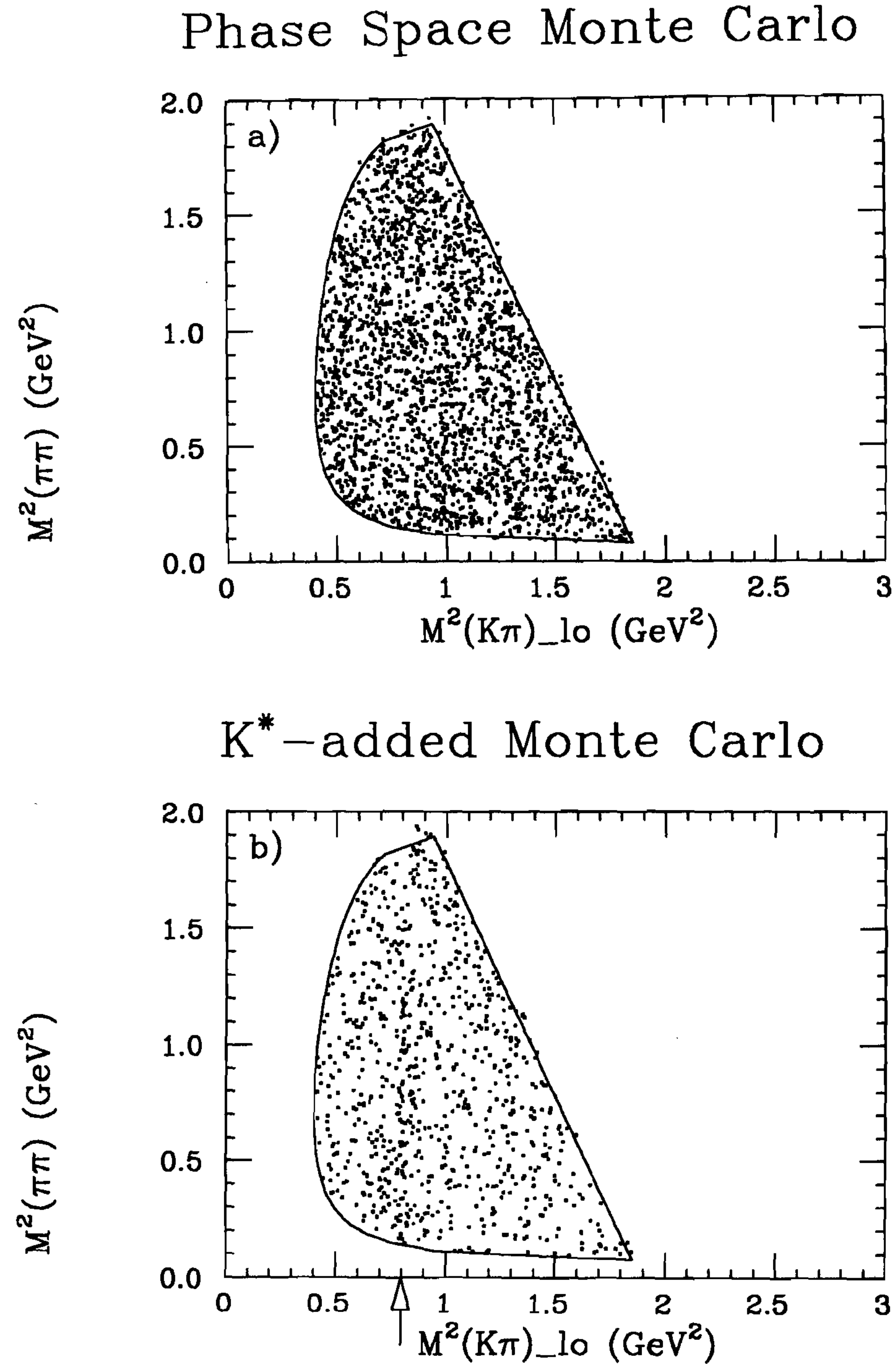

Figure 7.5: Dalitz plots for $D^{\pm} \rightarrow K^{\mp}\pi^{\pm}\pi^{\pm}$ for a) Phase-space Monte Carlo and b) Monte Carlo with 20% of the $D^{\pm} \rightarrow K^{\mp}\pi^{\pm}\pi^{\pm}$ proceeding via $D^{\pm} \rightarrow K^{*}(892)\pi^{\pm}$. The $K^{*}(892)$ mass-squared is indicated by the arrow.

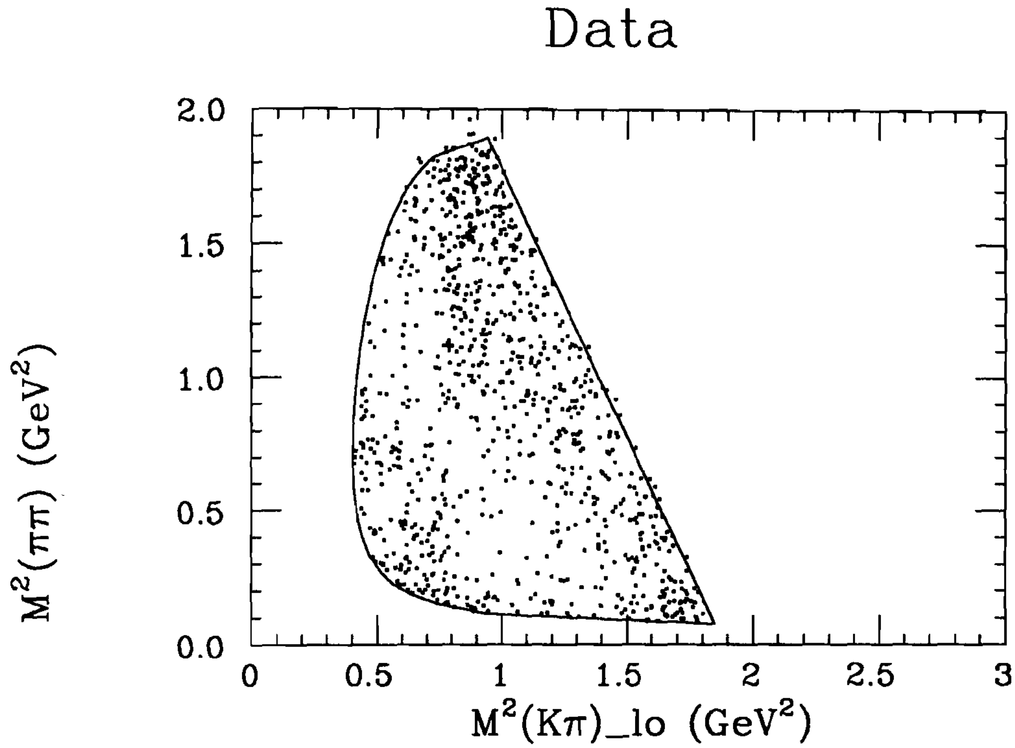

Figure 7.6: The Dalitz plot for data.

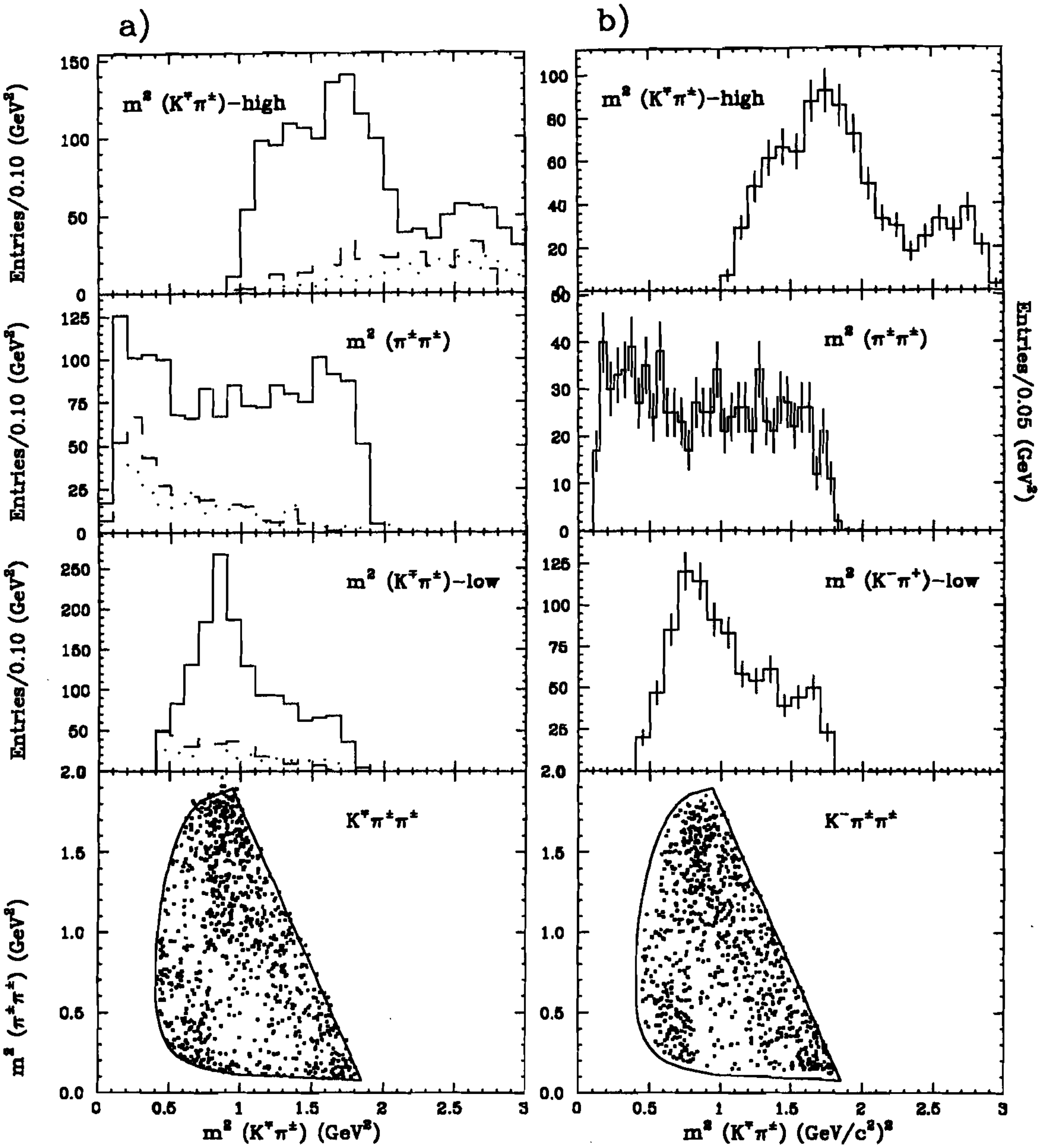

This Analysis

MARK III data

Figure 7.7: The Dalitz plot and the three projections for a) this analysis and b) MARK III data [31].

a) Data

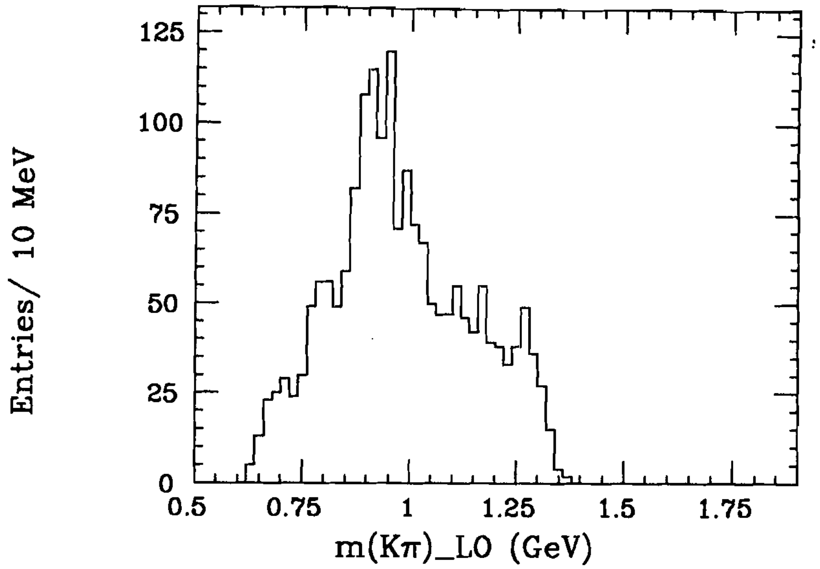

b) K* MC

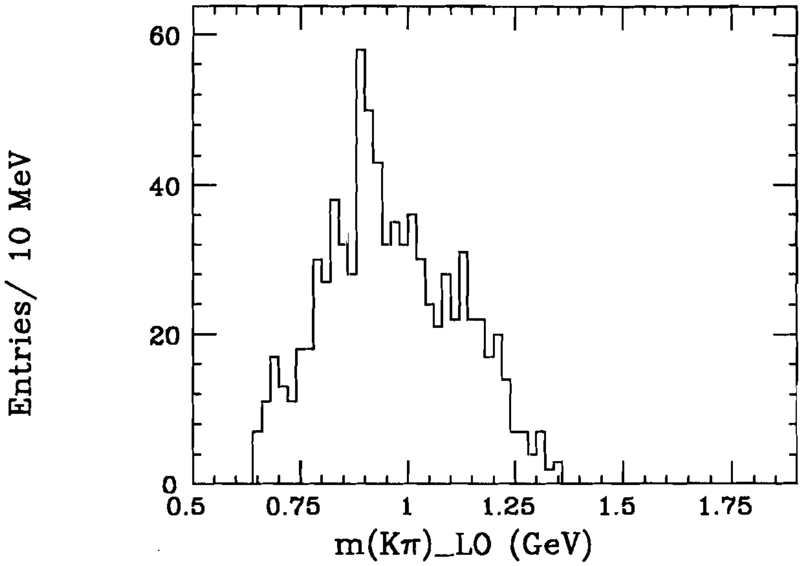

Figure 7.8: The lower $K\pi$ invariant mass for a) data and b) K^*-added Monte Carlo. The narrow K^* peak is clear in the Monte Carlo, but there is no clear evidence of a narrow resonance in the data.

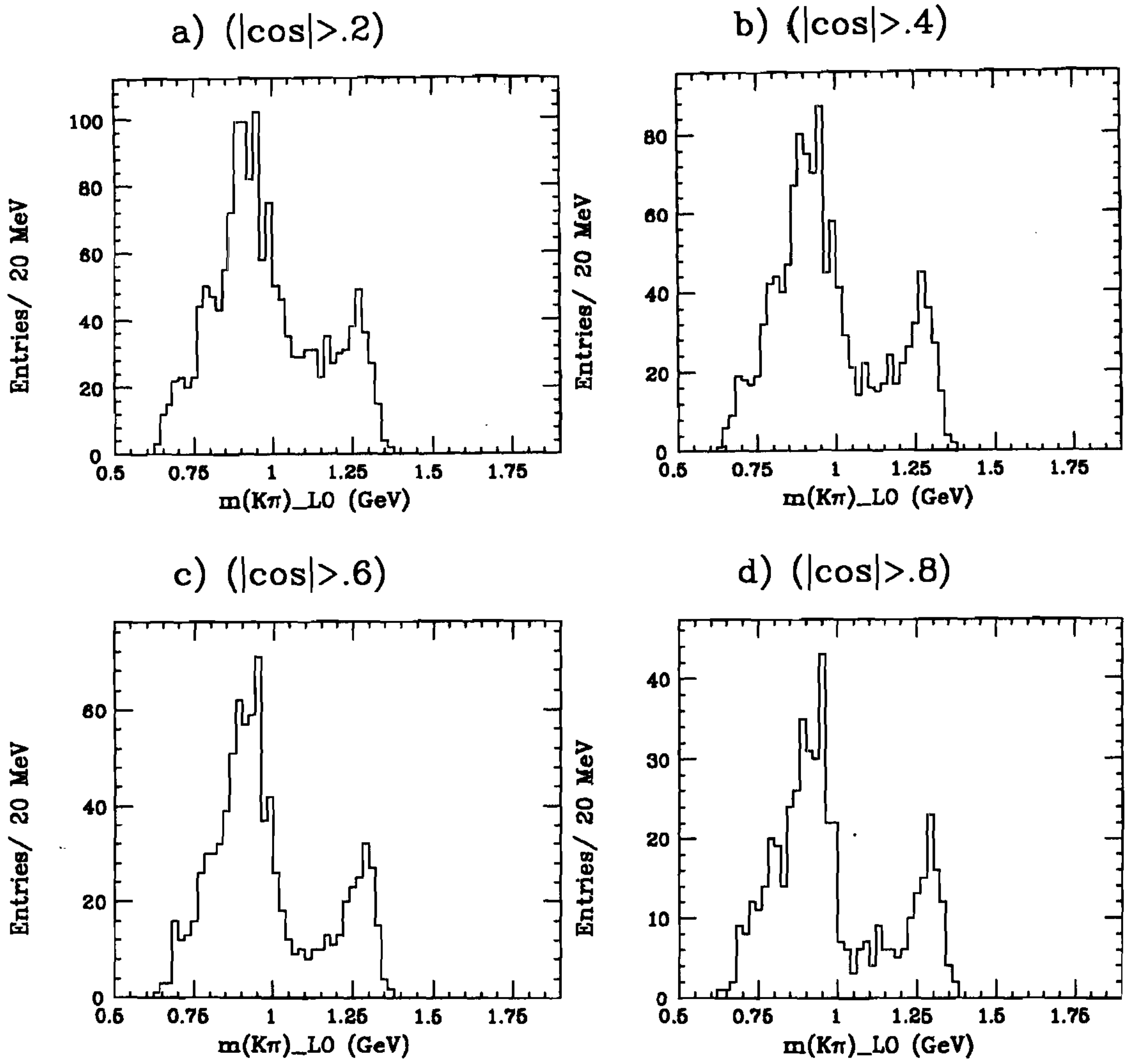

Figure 7.9: The lower $K\pi$ invariant mass for various cuts on the absolute value of the cosine of the angle between the two pions, as viewed in the K^* rest frame.

CHAPTER 8
Conclusion and Summary

Fermilab experiment E687 has seen a large sample of $D^{\pm}$ charm mesons in the decay $D^{\pm} \to K^{\mp}\pi^{\pm}\pi^{\pm}$. This sample is comparable to the world's largest sample. With this sample we have been able to study the production dynamics, the lifetime, and the dynamic substructure of the decay. This chapter will summarize the results.

We have been able to extend cross section measurements out to the world's highest photon energies. At our average photon energy of 220 GeV, the cross section times branching ratio for inclusive photoproduction of $D^{\pm}$ is:

$$\mathrm{BR} \cdot \sigma = 0.368 \pm 0.073 \ \pm 0.111 \ \mu\mathrm{b/Be\ nucleus}$$

for $x_f > 0$. Our cross section result at a photon energy of 142 GeV agrees with recent results from Fermilab experiment E691, at 145 GeV [17]. Our cross section as a function of photon energy shows a gentle rise, consistent with a compendium of cross section results. Our estimate of the total $c\bar{c}$ cross section as a function of energy appears somewhat higher than other measurements, although it is consistent with other data within errors. Our measured cross section agrees well with the photon-gluon fusion model calculated to second order in α_s, for m_c near 1.5 GeV [10]. The cross section as a function of x_f is also presented.

We are able to make very precise measurements of lifetimes with the aid of our Silicon microstrip vertex detector. The lifetime of the $D^{\pm}$ meson is calculated using a binned maximum likelihood technique with sideband background subtraction. The lifetime of the $D^{\pm}$ is measured to be:

$$\tau_{D^{\pm}} = 1.061 \ \pm \ 0.039 \ \pm \ 0.020 \ \mathrm{picoseconds}$$

The lifetime is consistent with other lifetime results and with the world average.

The ratio of D^+ to D^- has been measured and is found to be consistent with 1.

$$\frac{\text{number of } D^+}{\text{number of } D^-} = 1.060 \ \pm \ 0.063$$

The ratio is not a function of momentum. No evidence is seen for associated production.

The transverse momentum (squared) distribution for $D^\pm$ was measured. The distribution is fit to the form:

$$dN/d(P_\perp^2) \propto \exp(a_1 P_\perp^2 + a_2 P_\perp^4)$$

$$a_1 = -0.925 \ \pm \ 0.050/\ \text{GeV}^2$$

$$a_2 = 0.0368 \ \pm \ 0.0071/\ \text{GeV}^4$$

Dynamic substructure is found in the $D^\pm \rightarrow K^\mp \pi^\pm \pi^\pm$ decay, although no clear resonances are seen. The results agree with the Mark III data. The substructure is described by Diakanou and Diakanos [14], who attribute the lack of clear resonances to interference between the $K^*(892)$ and the $K_o^*(1430)$.

APPENDIX A

Calculation of the Monte Carlo Luminosity Scale Factor

A.1 Charm Particles Produced in Data:

A small target element of density ρ_A and thickness dz, irradiated by dn_γ photons will produce dn_c charm particles, assuming a cross section per nucleus of $\sigma_c^{(A)}$, which is different for different nuclei:

$$dn_c = dn_\gamma \left(\frac{\mathcal{N}_a}{A}\right) \sigma_c^{(A)} \ \rho_A \ dz \tag{A.1}$$

where $\mathcal{N}_a$ is Avagadro's number, and A is the atomic weight of the nucleus in question. We write dn_γ in terms of the photon flux,

$$dn_\gamma = \Phi(\vec{x}) \ dxdy \tag{A.2}$$

and

$$dn_c = \left(\frac{\mathcal{N}_a}{A}\right) \sigma_c^{(A)} \ \rho_A \ \Phi(\vec{x}) \ dxdydz \tag{A.3}$$

To get the total number of charm particles produced, we must add up the contributions from all these tiny target elements. Let us first determine the total number of charm particles created during a single run period, by the Si target. First, we find the total number of charm particles which are contributed by the Si sections of the target by integrating equation A.3 over the Silicon portion of the target:

$$N_c^{(Si)} = \int \left(\frac{\mathcal{N}_a}{A^{(Si)}}\right) \sigma_c^{(Si)} \ \rho_{(Si)}(\vec{x}) \ \Phi(\vec{x}) \ dxdydz \tag{A.4a}$$

Where $\rho_{(Si)}(\vec{x})$ is the spatially varying density function, which is $\rho_o^{(Si)}$ inside the Si sections of the Si target, and 0 elsewhere. The contribution from the Be sections of the

Si target to the total number of charm particles produced is:

$$N_c^{(Be)} = \int \left(\frac{\mathcal{N}_a}{A^{(Be)}}\right) \sigma_c^{(Be)} \; \rho_{(Be)}(\vec{x}) \; \Phi(\vec{x}) \; dxdydz \tag{A.4b}$$

Where $\rho_{(Be)}(\vec{x})$ is $\rho_o^{(Be)}$ inside the Be sections of the Si target, and 0 elsewhere. The total number of charmed particles during this run is then

$$N_{c(data)} = N_c^{(Si)} + N_c^{(Be)} \tag{A.5}$$

If we assume that the cross section goes as A^1 then

$$\frac{\sigma_c^{(Be)}}{A_{(Be)}} = \frac{\sigma_c^{(Si)}}{A_{(Si)}} \tag{A.6}$$

and we can write the total number of charm particles produced as:

$$N_{c(data)} = \frac{\mathcal{N}_a}{A^{(Si)}} \, \sigma_c^{(Si)} \int d^3x \; \Phi(\vec{x}) \; \rho(\vec{x}) \tag{A.7}$$

Where

$$\rho(\vec{x}) = \begin{cases} 0 & \text{if outside target;} \\ \rho_{(Si)} & \text{if inside the Si sections;} \\ \rho_{(Be)} & \text{if inside the Be sections.} \end{cases} \tag{A.8}$$

We introduce the total number of incident photons:

$$N_{\gamma(data)} = \int dxdy \;\, \Phi(x, y, z = 0) \tag{A.9}$$

and an effective target length:

$$\ell_{eff} = \frac{\int d^3x \; \Phi(\vec{x}) \; \rho(\vec{x})/\rho_{(Si)}}{\int d^2x \Phi(x, y, z = 0)} \tag{A.10}$$

then the number of charm particles produced during the the run period is given by:

$$N_{c(data)} = N_{\gamma(data)} \left(\frac{\mathcal{N}_a}{A_{(Si)}}\right) \sigma_c^{(Si)} \rho_{(Si)} \; \ell_{eff} \tag{A.11}$$

We can follow the same arguments for each of the run periods, even with different targets. We replace the $\rho(\vec{x})$ function with $\rho^i(\vec{x})$ where the index i indicates the run period. This target density function is still given by equation A.8, namely, 0 if outside the target, $\rho_{(Si)}$ if in Silicon, and $\rho_{(Be)}$ if in Beryllium. The spatially varying photon flux will also change for each run period: $\Phi \rightarrow \Phi_i$, and $N_\gamma \rightarrow N_\gamma^i$ and thus the effective lengths for the different run periods are:

$$\ell^i_{eff} = \frac{\int d^3x \; \Phi_i(\vec{x}) \; \rho^i(\vec{x})/\rho_{(Si)}}{\int d^2x \Phi_i(x, y, z = 0)} \tag{A.12}$$

If we introduce the total number of photons from the 1987-88 run, and the fractions of photons in each of the run periods (f_i) such that:

$$N^i_{\gamma(data)} = f_i N^{tot}_{\gamma(data)} \tag{A.13}$$

then we can write the combined total of charmed particles that E687 got during its 1987-88 run as:

$$N^{tot}_{c(data)} = N^{tot}_{\gamma(data)} \frac{\mathcal{N}_a \; \rho_{(Si)}}{A_{(Si)}} \; \sigma_c^{(Si)} \; \sum_i f_i \; \ell^i_{eff} \tag{A.14}$$

A.2 Charm Particles Produced in Monte Carlo

Let us look at the charm particles produced in GENERIC during one run segment. Our photon activation locations are chosen with an x, y distribution according to $\Phi(x, y)$ and the z location is chosen from the upstream face of the target to distance $\Lambda = \Lambda_o \; \sigma_o/\sigma_{mc}$, where Λ_o is the length of the longest target, the 5-Be target: $\Lambda_o = 4.06$ cm. (We define a Λ_o in this way so that it can be factored out when we sum over run periods.) The activation locations are then distributed according to:

$$\left(\frac{\Phi(x, y) \; dxdy}{\int d^2x \; \Phi(x, y)}\right) \left(\frac{\sigma_{mc} \; dz}{\sigma_o \Lambda_o}\right) \tag{A.15}$$

Once we have chosen the possible activation location, we activate the photon into a charm particle with an activation probability given by:

$$\mathcal{A} = \begin{cases} 0 & \text{if outside the target;} \\ 1 & \text{if inside Si;} \\ \rho_{(Be)}/\rho_{(Si)} & \text{if inside Be.} \end{cases} \tag{A.16}$$

Comparing equation A.16 with equation A.8, we see that the probability of activation is just $\rho(\vec{x})/\rho_{(Si)}$.

Thus, the probability that any given photon turns into a charm particle is given by the integration of the activation locations (equation A.15) times the probability of activation (equation A.16):

$$\mathcal{P} = \left(\frac{\sigma_{mc}}{\sigma_o \Lambda_o}\right) \left(\frac{\int d^3x \ \Phi(x,y) \ \rho(\vec{x})/\rho_{(Si)}}{\int d^2x \Phi(x,y)}\right) = \frac{\sigma_{mc} \ \ell_{eff}}{\sigma_o \Lambda_o} \tag{A.17}$$

where we have again introduced the concept of the effective target length as given in equation A.10.

If $N_{\gamma(mc)}$ photons are generated, then the number of charm particles created will be:

$$N_{c(mc)} = \frac{N_{\gamma(mc)} \ \sigma_{mc} \ \ell_{eff}}{\sigma_o \Lambda_o} \quad . \tag{A.18}$$

Again, we sum over the run periods: $N_{\gamma(mc)} \to N^i_{\gamma(mc)}$, $\ell_{eff} \to \ell^i_{eff}$ and the total number of charmed particles produced in a MC run is:

$$N^{tot}_{c(mc)} = N^{tot}_{\gamma(mc)} \ \frac{\sigma_{mc}}{\sigma_o \Lambda_o} \ \sum_i f_i \ \ell^i_{eff} \tag{A.19}$$

where we have used the photon fraction for each run period, and the total number of photons for all run periods.

A.3 Comparing Data to MC

Since we have arranged the Monte Carlo so that the f_i are the same as for data, and the photon fluxes are the same as for data, the ℓ^i_{eff} are the same for data and Monte Carlo. Further, if the cross sections are the same for Monte Carlo and data, we can use equations A.14 and A.19 to predict the number of charm particles in the data:

$$N^{tot}_{c(data)} = N^{tot}_{c(mc)} \left(\frac{N^{tot}_{\gamma(data)}}{N^{tot}_{\gamma(mc)}}\right) \left(\frac{\mathcal{N}_a \ \rho_{(Si)} \ \Lambda_o \sigma_o}{A_{(Si)}}\right) \tag{A.20}$$

That is, since the charm-particle-to-photon ratio is artificially boosted in the Monte Carlo, we must multiply the counted Monte Carlo luminosity by a scale factor, the last term in parentheses. The effective Monte Carlo luminosity is given by:

$$\mathcal{L}_{eff} = \mathcal{L}_{mc} \left(\frac{\mathcal{N}_a \ \rho_{(Si)} \ \Lambda_o \sigma_o}{A_{(Si)}} \right) \tag{A.21}$$

APPENDIX B

Cross Section Errors Caused by Monte Carlo Statistics

In general, the anticipated errors for the cross section fits are:

$$< \delta C_\alpha \; \delta C_\beta >= \sum_i \rho_{\alpha i} \, n_i \, \rho_{\beta i} \tag{B.1}$$

and the error on C_α is:

$$\sigma(C_\alpha) = \sqrt{\sum_i n_i \rho_{\alpha i}^2} \tag{B.2}$$

If errors on the $\rho_{\alpha i}$ matrix are considered (due to finite Monte Carlo statistics, then

$$\delta C_\alpha = \rho_{\alpha i} \, \delta n_i + (\delta \rho_{\alpha j}) n_j \tag{B.3}$$

where we are using the repeated index summation convention (except for α, which is never to be summed over). Autocorrelating and throwing out cross terms (which vanish if estimates are unbiased) we get:

$$\begin{aligned} < \delta C_\alpha \; \delta C_\alpha > &= \rho_{\alpha i} \, \rho_{\alpha i} \, n_i + < \delta \rho_{\alpha j} \; \delta \rho_{\alpha k} > n_j n_k \\ &= \rho_{\alpha i} \, \rho_{\alpha i} \, n_i + \sigma_{mc}^2 \end{aligned} \tag{B.4}$$

The familiar first term is the just error due to fluctuations in the number of charm events found in the data (equation B.1). The second term is the additional error arising from the uncertainty of the $\rho_{\alpha i}$ matrix elements. If the cross section measurement is correct then:

$$n_i = R_{i\beta} C_\beta \quad \text{and} \quad n_j = R_{j\gamma} C_\gamma$$

$$\sigma_{mc}^2 =< R_{i\beta} \; \delta \rho_{\alpha i} \; R_{j\gamma} \; \delta \rho_{\alpha j} > C_\beta C_\gamma \tag{B.5}$$

We consider the case of the just-constrained limit, where $\rho = R^{-1}$. The inverse relation between these two correlates their errors:

$$(\rho_{\alpha i} + \delta\rho_{\alpha i})(R_{i\beta} + \delta R_{i\beta}) = 1 \quad \text{or} \quad \delta\rho_{\alpha i} R_{i\beta} = -\rho_{\alpha i}\delta R_{i\beta} \tag{B.6}$$

Using equation B.6 we can reduce equation B.5 to:

$$\sigma_{mc}^2 = \rho_{\alpha i} < \delta R_{i\beta}\ \delta R_{j\gamma} > \rho_{\alpha j}\ C_\beta C_\gamma \tag{B.7}$$

Now, the $R_{i\alpha}$ matrix is measured from Monte Carlo by equation 5.9: $R_{i\alpha} = g\, G_{i\alpha}/C_\alpha^{(mc)}$, where we have used g to replace the ratio of the luminosities. The bracketed term in equation B.7 can be written as:

$$\begin{aligned} < \delta R_{i\beta}\ \delta R_{j\gamma} > &= \frac{g^2}{C_\beta^{(mc)}\ C_\gamma^{(m)c}} < \delta G_{i\beta}\ \delta G_{j\gamma} > \\ &= \frac{g^2}{C_\beta^{(mc)}\ C_\gamma^{(mc)}}\ G_{i\beta}\ \delta_{ij}\ \delta_{\beta\gamma} \end{aligned} \tag{B.8}$$

Substituting into equation B.7, we get:

$$\sigma^2{}_{mc} = g^2\ \rho_{\alpha i} \left(\sum_\beta m_{i\beta} \right) \rho_{\alpha i}$$

as long as $C^{(mc)} = C^{(data)}$. If we let $m_i = \sum_\beta\ G_{i\beta}$ we get:

$$\sigma^2{}_{mc} = g^2\ \rho_{\alpha i}\ m_i\ \rho_{\alpha i} \tag{B.10}$$

an expression which is analogous to the first term of equation B.4. Since we are assuming $C_\alpha^{(mc)} = C_\alpha^{(data)}$, then

$$m_i = \frac{1}{g} R_{i\alpha}\ C_\alpha^{(mc)} = \frac{1}{g}\ n_i \tag{B.11}$$

Thus:

$$\sigma^2{}_{mc} = g\ \rho_{\alpha i}\ n_i\ \rho_{\alpha i}$$

$$< \delta C_\alpha\ \delta C_\alpha >= \rho_{\alpha i}\ \rho_{\alpha i}\ n_i\ \ (1+g) \tag{B.12}$$

Since we have assumed the cross sections for Monte Carlo and data are identical, and since the Monte Carlo simulation is identical to data, then the ratio of the luminosities of the Monte Carlo and data will be the same as the ratio of the charm events found in Monte Carlo and data: $g = N_{data}/N_{mc}$. Thus, to include the effects of Monte Carlo statistics, the errors of the cross sections given by equation B.2 should be modified:

$$\sigma(C_\alpha) = \sqrt{\sum_i n_i \rho^2_{\alpha i}}\ \sqrt{1 + N_{data}/N_{mc}} \tag{B.13}$$

REFERENCES

[1] B. J. Bjorken and S. L. Glashow, Phys. Lett. 11:255 (1984).

[2] S.L. Glashow, J. Iliopoulos, and L. Maiani, Phys. Rev. D2:1285 (1970).

[3] J. E. Augustin et al., Phys. Rev. Lett. 33:1406 (1974).

[4] J. J. Aubert et al., Phys. Rev. Lett. 33:1404 (1974).

[5] G. S. Abrams et al., phys. Rev. Lett. 33:1453 (1974).

[6] G. Goldhaber et al., Phys. Rev. Lett. 37:255 (1976).

[7] I. Peruzzi et al., Phys. Rev. Lett. 37:569 (1976).

[8] L.M. Jones and H. W. Wyld, Phys. Rev. D17:759 (1978).

[9] F. Bergsma et al., Phys. Lett. B123:269 (1983).

[10] R. K. Ellis and P. Nason, Nucl. Phys. B312:551 (1989).

[11] D. Aston et al., Phys. Lett. 94B:113 (1980).

[12] R. J. Morrison and M. S. Witherall, Ann. Rev. Nucl. and Part. Sci., Vol 39.

[13] J. Adler et al., Phys. Lett. B196:107 (1987).

[14] M. Diakonou and F. Diakonos, Phys. Lett. B216:436 (1989).

[15] U.S. Department of Energy, Investigation Report of the Fire in the Wide Band Laboratory at Fermi National Accelerator Laboratory, Batavia, Illinois, October 3, 1987. Chicago: DOE Chicago Operations Office (1987).

[16] G. Jaross, SKIMADEE, E687 Internal Memo.

[17] J. C. Anjos et al., Phys. Rev. Lett. 62:513 (1989).

[18] R. D. Field and R. P. Feynman, Nucl. Phys. B136:1 (1978).

[19] M. Giammarchi et al., Nucl. Instr. and Meth., A251:40 (1986).

[20] S. Park, Ph.D. Thesis, Northwestern University, unpublished.

[21] J. Wiss et al., Unfolding the Differential Cross Section, E687 Internal Memo.

J. Wiss, Binning Considerations for Cross Section Method, E687 Internal Memo.

[22] G. Jaross, Ph.D. Thesis, University of Illinois, unpublished.

[23] J. C. Anjos et al., Phys. Rev. Lett., 58:311 (1987)

[24] J. Wiss and R. Culbertson, DVERT, E687 Internal memo

[25] Particle Data Group, Review of Particle Properties, Phys. Lett. B204 (1988).

[26] J. R. Raab et al., Phys. Rev. D37:2391 (1988).

[27] H. Albrecht et at., Phys Lett. B210:267 (1988).

[28] M. Aguilar-Benitez et al., Phys. Lett. B193:140 (1988).

[29] H. Palka et al., Z. Phys. C35:151 (1987).

[30] S. E. Csorna et al., Phys. Lett. B191:318 (1987).

[31] Alan J. Weinstein kindly provided the Mark III plots electronically.

VITA

Karen Lingel was born in Dayton, Ohio on 17 June 1961, and raised in Billings, Montana. She took two years of honors high school Physics taught by Mr. John Linn at Billings West High School. In 1979, she began her college career at the University of California, Berkeley, majoring in Physics. In the summer of 1982, she was accepted to the summer student program at Lawrence Berkeley Laboratory, working in the Victor Perez-Mendez group for Terry Mulera. She continued this work for the remainder of her time at Berkeley. This work was published in 1984. (K. Lingel, T. Mulera, V. Perez-Mendez, A. Del Guerra, *Investigation of Dead Times and Dead Zones in Wire Chambers Operated in the Self-quenching Streamer Mode*, IEEE Trans. Nucl. Sci., NS-31,(1984).) Karen graduated from Cal with distinction in June 1983. She began graduate work in physics the following September at the University of Illinois, at Urbana-Champaign. She held teaching assistantships in 1983 and 1984. In the summer of 1984, she began working for Jim Wiss on Fermilab Experiment E687. She received the Master of Science degree in August 1984. She enjoys travel, art, music, and aerobics.